Fast and Robust Methods for Diffusion-Weighted Magnet Resonance Imaging of the Human Spinal Cord.

Schnelle und robuste Verfahren für die diffusionsgewichtete Magnet-Resonanz-Tomographie des menschlichen Rückenmarks

by

Caspar Florin

born

06. march 1991

Dissertation to obtain a doctoral degree
at the Faculty of Mathematics, Computer Science and Natural Sciences, Department of Physics
at the University of Hamburg

Gutachter/innen der Dissertation:	Prof. Dr. Florian Grüner Dr. Jürgen Finsterbusch
Zusammensetzung der Prüfungskommission:	Prof. Dr. Florian Grüner Dr. Jürgen Finsterbusch Prof. Dr. Martin Koch Dr. Thomas Lindner Prof. Dr. Hagner
Vorsitzende/r der Prüfungskommission:	Prof. Dr. Hagner
Datum der Disputation:	21.12.2021
Vorsitzender Fach-Promotionsausschusses PHYSIK:	Prof. Dr. Wolfgang Hansen
Leiterdes Fachbereichs PHYSIK:	Prof. Dr. Günter, H. W. Sigl
Dekan der Fakultät MIN:	Prof. Dr. Heinrich Graener

Abstract

Magnet resonance imaging is an important tool in the clinical diagnostics and biomedical research, as with it in vivo non-invasive cross sections can be acquired. For the central neural system diffusion weighted imaging (DWI) is thereby of high interest, as with it the structure of tissues can be reflected. In the brain DWI is widely used with echo-planar imaging (EPI), due to its short acquisition times and reasonable image quality. In the spinal cord acquisitions are rather difficult, as the magnetic inhomogeinities are stronger, a high spatial resolution is needed and measurement times are longer.
To ameliorate these problems, in this work EPI is combined with different inner field-of-view (FOV) techniques, based on 2DRF excitations or cross sectional excitations (ZOOM), as they reduce spatial distortions. To accelerate the acquisition time we combined the inner FOV EPI with simultaneous multi slice (SMS) imaging. In this work we show at phantoms and in vivo that the combination of SMS and inner FOV increases the SNR efficiency. Tilted 2DRF excitations and ZOOM 180° combined with SMS show the best results as they are not as sensitive as collinear 2DRF excitations or ZOOM 90°.
Near metallic implants EPI suffers strongly, due to its sensitivity to magnetic inhomogeinities. Thus, the performance of STEAM and FSE is investigated in this work, as they are more robust, due to RF pulse refocusing. We combine them with inner FOV techniques, to reduce the measurement time and increase the performance. To correct in-plane and slice direction displacements they are combined with view-angle tilt and multi-acquisition variable-resonance image combination (MAVRIC). Further to suppress folding artifacts due to MAVRIC, saturation pulses are utilized. Near metallic implants at phantoms and in vivo STEAM and FSE combined with these techniques show promising results. STEAM acquisitions have a rather low SNR but short acquisition times. FSE acquisitions have a good image quality with reasonable SNR but long measurement times.
In this work EPI is combined with SMS and inner FOV which improves the performance of spinal cord DWI and can facilitate clinical applications. Further, near metallic implants great progress is made with FSE and STEAM combined with different techniques, even though there is still room for improvement in hindsight of SNR and acquisition time.

Zusammenfassung

Die Magnetresonanztomographie ist ein wichtiges Werkzeug für die klinische Diagnostik und die biomedizinische Forschung, da in vivo nicht-invasive Querschnitte aufgenommen werden können. Für das Nervensystem ist dabei die diffusionsgewichtete Bildgebung (DWI) von großem Interesse, um die Struktur von Geweben abzubilden. Im Gehirn wird DWI meist mit Echo planarer Bildgebung (EPI) durchgeführt, aufgrund kurzer Aufnahmezeiten und guter Bildqualität. Im Rückenmark ist dies jedoch schwierig, da eine hohe räumliche Auflösung, sowie lange Messzeiten und eine gewisse Robustheit benötigt werden.

Um die Probleme zu reduzieren, kombinieren wir EPI mit verschiedenen inneren Messfeld (FOV) Techniken, die auf 2DRF- oder Querschnitts Anregungen (ZOOM) basieren, um räumliche Verzerrungen zu reduzieren. Um die Aufnahmezeit zu reduzieren, wird innerem FOV EPI mit simultaner multi-Schicht (SMS) Bildgebung kombiniert. Es wird an Phantomen und in vivo gezeigt, dass SMS und innerem FOV kombiniert die SNR-Effizienz erhöht. Tilted 2DRF und ZOOM 180° kombiniert mit SMS zeigen die besten Ergebnisse, da sie nicht so empfindlich sind wie collinear 2DRF oder ZOOM 90°.

Aufgrund der Empfindlichkeit gegenüber magnetischen Inhomogenitäten leidet EPI in der Nähe metallischer Implantate. Daher untersuchen wir die Leistung von STEAM und FSE, da sie durch RF-Puls Refokussierung robuster sind. Wir kombinieren sie mit inneren FOV-Techniken, um die Messzeit zu verkürzen und die Leistung zu steigern. View-angle tilt und multi-acquisition variable-resonance image combination (MAVRIC) werden zur Korrektur von Verschiebungen in der Ebene und in Schichtrichtung genutzt und um Faltungsartefakte durch MAVRIC zu unterdrücken, werden Sättigungspulse verwendet. Metallnahe STEAM und FSE Aufnahmen an Phantomen und in vivo zeigen vielversprechende Ergebnisse. STEAM Messungen haben ein eher niedriges SNR, aber kurze Messzeiten. FSE Aufnahmen haben eine gute Bildqualität mit vernünftigem SNR, aber langen Messzeiten.

In dieser Arbeit wird EPI mit SMS und inner FOV kombiniert, was die Leistung von Rückenmark DWI verbessert und klinische Anwendungen erleichtert. Mit FSE und STEAM in Kombination mit diversen Techniken werden nahe metallischer Implantate große Fortschritte erzielt, hinsichtlich SNR und Messzeit ist aber noch Raum für Verbesserungen.

Contents

Chapter 1

Introduction

In 1936, Isidor Rabi discovered and described nuclear magnetic resonance in molecular beams by extending the Stern-Gerlach experiment [69]. In 1945/46 Felix Bloch and Edward M. Purcel expanded this technique and described the magnetic resonance in solids and fluids [6, 67].This laid the foundation for the development of magnetic resonance spectroscopy. Based on this discovery Paul C. Lauterbur invented magnetic resonance imaging in 1971 and published its theory in 1973 [49]. His theory is characterized by two main proposals. To enable imaging of the nuclear magnetic resonance he first introduced magnetic gradient fields to allocate the detected signal spatially, the so called spatial encoding. Secondly, he proposed to rotate the magnetic field gradients for successive measurements to obtain varying space encodings for the object. Filtered back projection then allows to obtain an image from the object. Following, in 1974 Peter Mansfield developed mathematical methods to convert the signal into image information. Further he developed techniques that allow to excite only a precise layer in an object – so called, slice selective excitation –. In 1977, he introduced a procedure with extreme fast switching of the gradients, the so called Echo Planar Imaging, resulting in image acquisitions of less than a second [63]. The theoretical foundation of the MRI as well as the principle functionality of magnetic gradient fields will be described in Section 2.1.
In 1985, magnet resonance imaging (MRI) was made viable for clinical diagnostics due to the invention of the Fast-Low-Angle-Shot (FLASH) technique, by Axel Haase, Jens Frahm and Dieter Matthaei [30]. The FLASH technique combines low flip angle radio-frequency (RF) excitations with gradient echoes which allows rapid continuous and sequential measurements. Around this time, Jürgen Henning developed a spin echo variation which is sensitive to pathological tissue structures [36], which today is known as fast spin echo (FSE), turbo spin echo (TSE) or rapid acquisition with relaxation enhancement (RARE). The functionality and the usage of sequences – FLASH, FSE, echo planar imaging, and

stimulated echo acquisition mode – will be explained in detail in the second section of Chapter 2.
Up to today the MRI has proven to be a valuable noninvasive method in clinics for examinations of soft tissues in the whole body, e.g. torn ligament, brain lesion, tendon injury. But also in neuroscience, where with techniques like functional MRI [38, 48] or diffusion weighted imaging (DWI) [58, 80] the neural network and its activities can be comprehended. FMRI uses the blood-oxygen-level dependent (BOLD) contrast which is based on difference in magnetic susceptibilities of oxygenated and deoxygenated blood [4]. This leads to differences of the which can be detected using an MRI scanner. Repetitive measurements thus enable the possibility to map the neural activity with FMRI. DWI allows to map the diffusion process of molecules – mainly water – in biological tissues and nerve fibers. The proton precession can be manipulated by applying gradients and by reapplying gradients in opposite direction with equal magnitude. As this refocusing process is not perfect for moving protons the signal measured by the MRI is reduced. As a result repetitive measurements with varying gradients can track the motion of molecules. As molecular diffusion is not free in tissues, but can reflect interactions with obstacles, measured diffusion patterns can be used for tissue structure mapping or nerve tract visualization. The principle of DWI will be discussed in detail in Section 2.3.
As most of the neural activities can be observed in the brain most FMRI and DWI studies were concentrated on it. However, in recent years the interest for the spinal cord increased, as it is assumed that the nerve activities of brain and spine are closely related.
Generally performing diffusion weighted imaging in the spinal cord is not as simple as in the brain. One reason is that typically measurement times are often more than 10 minutes long even for small regions of interest. As a consequence any motion of a patient can lead to incoherent data due to displacement. Another reason is that the generally used echo planar imaging is rather prone to magnetic inhomogeneities. These, however, are much more pronounced in the spinal cord than in the brain due to susceptibility variations of different tissues and bones. The variations can influence the magnetic flux densities and as result they can lead to signal displacement.
This work addresses these obstacles to enable obtaining undisturbed information on the spinal cord, e.g. tissue micro structure, the integrity of axons and white matter fibers in the central nervous system. More precisely, diffusion-weighted magnetic resonance imaging which is used for the acquisition of these informations.
As a first step inner field-of-view techniques, like 2D-selective RF excitations [7, 33] or cross sectional excitations [16, 86], were used in combination with echo planar imaging.

The reduced field-of-view enables a high resolution for small regions of interest, like the spinal cord, and prevents aliasing effects. The theoretical background is given in the fourth Section of Chapter 2. In the next step the image acquisition was accelerated with simultaneous multi-slice acquisitions [2, 43] to decrease the motion artifacts, during echo planar imaging. The general idea behind simultaneous multi-slice acquisitions is to excite multiple slices with phase modulated RF waveforms. This will be explained in detail in Section 2.5. As final step we combined the simultaneous multi-slice technique and the inner-field-of-view techniques, to decrease the acquisition time by a factor of about 2-3 and to decrease the influence of neighboring tissues. The combined techniques were investigated in the absence of metallic implants at phantoms and in vivo at the spinal cord. The results are compared to acquisitions without inner field-of-view techniques and or simultaneous multi-slice acquisition. This work is presented and discussed in Chapter 4. For the second part of the thesis image acquisition near metallic implants was improved, to enable the monitoring of spinal cord injuries during rehabilitation or injury treatment. The improvement was carried out in multiple steps. First, instead of gradient refocused sequences – e.g. echo planar imaging – we used fast-spin-echo imaging and turbo stimulated echo acquisition mode [23] which are RF refocused sequences. Inherently, these sequences have a significantly longer acquisition time compared to echo planar imaging. As a result they are less efficient when they are applied at spinal cords without metallic implant. However, as they are more robust and much less sensitive to artifacts they should have a better performance in the vicinity of metallic implants. To reduce the effect of magnetic inhomogeinities even further and to accelerate the acquisitions, the sequences were combined – like echo planar imaging– with inner field-of-view techniques and simultaneous multi-slice acceleration. The performance was investigated at phantoms and in vivo at volunteers with metallic implants and is presented in the first part of Chapter 5. To reduce distortions even further we combined the sequences with view angle tilt imaging [13] and multi-acquisition variable-resonance image combination [45]. View angle tilt imaging is used to reduce in-plane distortions by adding additional gradients during image read out while multi-acquisition variable-resonance image combination corrects distortions in slice direction by using spectral RF excitations. The principle of both techniques are described in Section 2.6. The individual and combined performance of the techniques in combination with the different sequences is presented in the second half of Chapter 5. The investigations are performed at phantoms and in vivo at volunteers with and without metallic implants. Further they are compared to echo planar imaging.

Chapter 2

Theoretical Background

For an overall understanding of the concept of magnet resonance imaging the fundamentals – the basic effects and how an in vivo image is obtained from the signal – are described in this chapter.
Following the basic sequences used for the data acquisition, fast-spin echo, stimulated echo acquisition and echo planar imaging are described. The specifics to be considered for each sequence as well as the difference in between them will be outlined.
Thereafter, the principle of diffusion-weighted imaging and the resulting possibilities to measure e.g. tissue micro structure, the integrity of axons and white matter fibers will be explained, as well as the difficulties which can occur during the measurements.
Methods to accelerate the image acquisition, as well as inner field-of-view techniques are described next. The influence of magnetic inhomogeinities and the resulting artifacts are explained in the following section. At last, the two methods used in this work to compensate for effects arising due to inhomogeinities, view-angle-tilt and multi-acquisition variable-resonance image combination, and how they influence the image acquisition, are explained.

2.1 Magnet Resonance Imaging

The description of the nuclear magnetic resonance (NMR) of atomic nuclei by Bloch and Purcell [24] is the fundamental principle behind magnetic resonance imaging (MRI). Nuclei of hydrogen (protons) have a spin, so called spin-1/2 nuclei, with two spin states and hence a magnetic dipole moment $\vec{m}$. When they are placed in a strong external magnetic field they precess around an axis along the direction of the field. The protons align in two energy eigenstates (Zeeman effect): one low and one high energy, which are separated by a small splitting energy:

$$\Delta E = \hbar \cdot \omega \tag{2.1}$$

with $\hbar$ the Plank constant and the excitation frequency ω. An ensemble of protons in the presence of a magnetic field, B_0 will appear to precess with the Larmour frequency

$$\omega_{Lar} = g_j \, \frac{q}{2\, m} \cdot |\vec{B}_0| \qquad . \tag{2.2}$$

It is depending on g_j the Landé-factor, the charge q, the mass m as well as the strength of the magnetic flux density [52]. In case of a magnetic flux density of of one Tesla ω_{Lar} is 42.58 MHz. Due to a tiny excess of protons in the lower energy state the summation results in an external detectable longitudinal magnetization $\vec{M}_L$ along $\vec{B}_0$ [32] parallel to the external magnetic flux density. By applying an RF pulse in resonance with ω_{Lar} this magnetization can be tipped sideways, with i.e. a so-called 90° pulse, or even reversed with a 180° pulse. The protons will come into phase with the RF pulse and therefore each other.
If the RF pulse is turned off, the transversal vector component creates an oscillating magnetic field which induces a small current in the receiver coils. This signal is called free induction decay (FID). Its amplitude holds information on the strength of the transversal magnetization, which depends on the type of nucleus, the location and the excitation pulses. By Fourier transformation it is possible to disentangle the signal of different nuclei and discriminate them.
While the RF pulse is applied, the longitudinal magnetization $\vec{M}_L$ is 0 and the spins perform a precession motion in the xy-plane. After the pulse is turned off, the transversal magnetization decays and the equilibrium state with only longitudinal magnetization $\vec{M}_L$ is restored. The change of magnetization in z – longitudinal direction – happens with [52]:

$$M_z(t) = M_0 \cdot \left(1 - \frac{M_z(0)}{M_0} \cdot \mathrm{e}^{-\frac{t}{T_1}}\right) \qquad . \tag{2.3}$$

Thereby M_0 describes the strength of magnetization in direction of $\vec{B}_0$ in the equilibrium state, $\frac{M_z(0)}{M_0}$ describes in which state the system is at the beginning of the relaxation process ($\frac{M_z(0)}{M_0} = 1$: saturation, $M_z(0) = -M_0$: inversion). T_1 is the so-called spin-lattice-relaxation time and describes the time until the z-component of the magnetization reaches $1 - \frac{1}{e}$ after being flipped into the transverse plane by a 90° radio frequency pulse. Typical T_1 are e.g. in water a few seconds, in oil even shorter, but in ordered solids they can take up to a few hours [72].

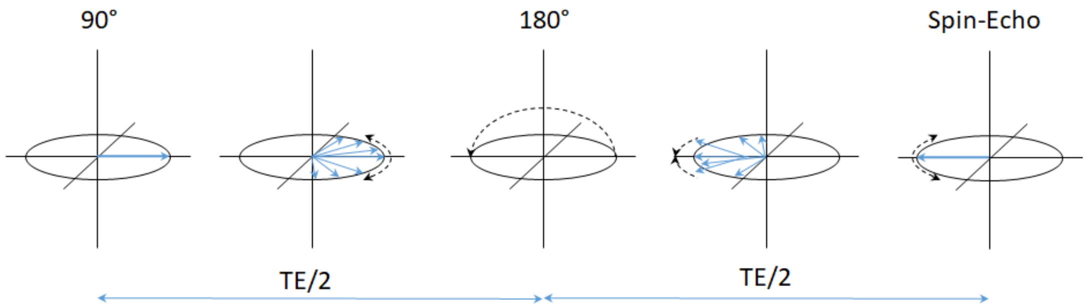

Figure 2.1: Illustration of the creation of a spin-echo. The spins are first oriented in one direction by a 90 degree pulse, after a time TE/2, in which the spins dephase, a 180 degree pulse is applied and another TE/2 later the spins rephase and produce a spin echo. Thereby, the signal strength relies on T_2 relaxation time, as it depends on non-reversible effects [52].

The transverse magnetization decays similar to the increase of $\vec{M}_z$, due to the interaction between neighboring nuclei. The reason in this case is the spin-spin-relaxation which leads to a dephasing of the spins which results in a decrease of the magnetization. This decay can be described by:

$$\vec{M}_T(t) = M_T(0) \cdot \mathrm{e}^{-\frac{t}{T_2}} \tag{2.4}$$

T_2 is the so-called spin-spin relaxation time and describes the time until $1 - \frac{1}{e}$ of the transversal magnetization is decayed. The T_2 duration depends on the chemical surrounding of the hydrogen nuclei like T_1. It varies between all tissues, e.g. tumor tissue has a longer T_2 than muscle tissue [70].

In an idealized nuclear magnetic resonance experiment, the FID decays approximately exponentially with a time constant T2. However, in practical MRI there are small differences in the static magnetic field at different spatial locations ("inhomogeneities") that cause the Larmor frequency to vary across the body. This creates destructive interference, which shortens the FID. However, as this is not random, but dependent on the location of the nuclei in the magnetic field, the dephased signal can be recovered for non moving nuclei using refocusing gradients (to create a so-called "gradient echo"), or RF pulses (to create a so called "spin-echo"). A spin-echo experiment is illustrated in figure 2.1. The corresponding transverse relaxation time constant is T_2^* which is usually much smaller than T_2.

In a spin-echo experiment, the spins are first oriented in one direction by a 90 degree pulse, after a time TE/2, in which the spins dephase, a 180 degree pulse is applied and another TE/2 later the spins rephase and produce a spin echo. Thereby, the signal strength relies on the T_2 relaxation time, as it depends on non-reversible effects [52]. If more than three RF pulses are used even so called stimulated echoes can occur due to successive stimulation of the magnetization which can be utilized with so called stimulated echo acquisition mode (STEAM) sequences.

2.1.1 Spatial Encoding

The fact that the excitation frequency is directly proportional to the applied magnetic flux density can be used to selectively excite a region in a system. A magnetic gradient field oriented in z direction G_z causes the magnetic flux density $\vec{B}$ to linearly change in z. The specific excitation of a slice can be conducted with a shaped RF-pulse and a slice encoding gradient G_z. The thickness of the excited slice thereby depends on the bandwidth of the RF excitation pulse. A slice selective excitation leads to a location dependency of the frequency [52]:

$$\omega(z) = \omega_{Lar} + \gamma G_z \cdot z \tag{2.5}$$

It is now possible to calculate the location specific excitation energy or rather the frequency. As a result the dimensional problem is reduced by one, due to the slice selective excitation. To further encode the signal an additional gradient is applied perpendicular to the slice encoding direction while the signal is measured, the so called read-out or frequency encoding gradient G_{RO}. The magnetic field gets linearly varied in read out direction and as result the frequency gets modulated linearly along this direction and thus, depending on the location the precession of the magnetization differs. This difference can be analyzed and by Fourier transforming the signal can be assigned to its specific spatial location.

An additional method to encode the signal spatially is to apply a gradient in-between the RF-excitation and the data acquisition which is usually perpendicular to the slice selective and the read-out gradients. This leads to a modulation of the spin phase in a controlled manner and thus the gradient is called phase-encoding gradient G_{PE}. The gradient changes the signal depending on location and gradient strength. A single gradient thereby does not enable a definitive mapping of the signal. Thus, the gradient and the signal read-out is repeated several times, during which the phase encoding gradient is applied with changing amplitudes, e.g. in an incremental manner. In this way different data sets can be measured in the k-space [52] which is explained in detail in the next section.

2.1.2 The k-space

The k-space is the Fourier transform of the spatial frequencies in the MR image and helps to understand the spatial encoding, the comparison of MRI-sequences and their properties [83]. Each k-space point contains spatial frequencies and phase information about every pixel of the measured region. Conversely, each pixel in the image maps to every point in k-space. It can describe the signal in all three dimensions:

$$S(\vec{k}) = \int \rho(\vec{r})\ \mathrm{e}^{i2\pi\vec{k}\vec{r}} \mathrm{d}^3 r \tag{2.6}$$

with the spin density $\rho(\vec{r})$ and

$$\vec{k}(t) = \frac{\gamma}{2\pi} \int_0^t \vec{G}(t')\mathrm{d}t' \in \Re \qquad . \tag{2.7}$$

By inverse Fourier-transformation the signal which corresponds to the spatial frequencies, the spin density in a specific slice can be determined. As the k-space is infinite and the signal of each point in k-space needs to be know, it is impossible to solve the equation exactly. As result only a reduced number of points N on a trajectory with a distance Δk compound by k_{PE} and k_{RO} can be measured and converted with a discrete Fourier-transformation. This affects the local resolution, as it depends on the distance of the first two zeros of the maximum of the point-spread function (PSF), which describes the response of an imaging system to a point source or point object and is depending on the sampled area [78]. The local resolution can be described with

$$\Delta x = \frac{1}{N\Delta k} \qquad . \tag{2.8}$$

At large objects, however, scanning only a small part of the k-space can lead to a convolution of the PSF in the spatial domain, which can result in so called Gibbs-Ringing [12]. The mapping of the frequencies is limited to a so-called field-of-view (FOV). Thus, it is necessary to ensure that during the discrete scanning of the k-space the size of the object is smaller than the FOV else signal outside the FOV could fold into it.

The trajectory, with which the k-space is measured, can be manipulated by varying the phase and or frequency encoding gradients. This enables the possibility to scan the k-space in different manners. Two possible methods are shown in figure 2.2. **(a)** shows a radial trajectory, where the center of the k-space is measured N times, as each k-space line

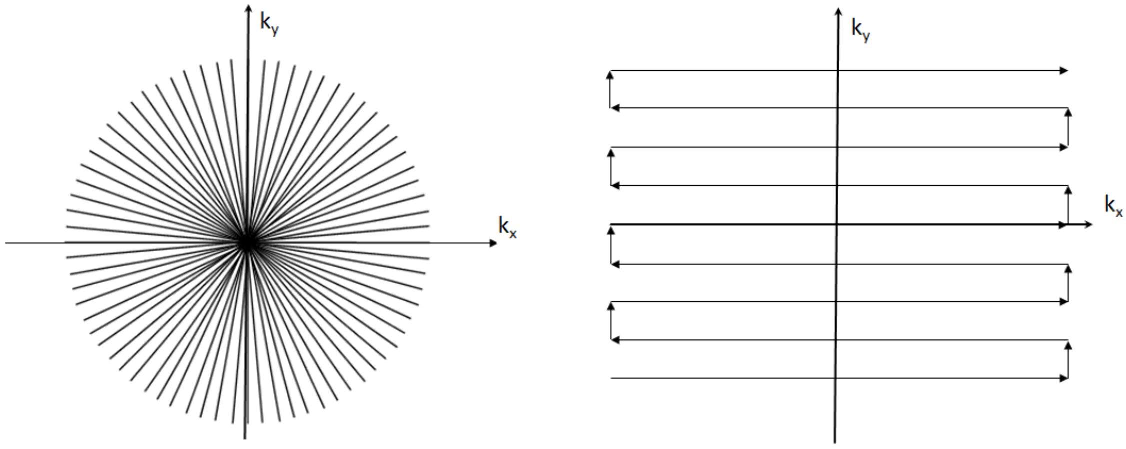

(a) **(b)**

Figure 2.2: **(a)** sketch of radial trajectory to measure the k-space. **(b)** sketch of a blipped planar parallel procedure to measure the k-space.

crosses the center. In **(b)** a blipped planar trajectory is shown, where in read out direction parallel lines are measured at which ends small phase encoding gradients (blips) are applied to scan the k-space perpendicular to the read out lines.

2.2 Image Acquisition Sequences

After Paul C. Lauterbur laid the foundation of the MRI in 1971, as described in the introduction, sequences were developed or adapted to enable in vivo measurements. Three nowadays used techniques are: Echo-planar imaging (EPI) by Peter Mansfield [63], fast-spin echo (FSE) by Jürgen Henning [36] and stimulated echo acquisition mode (STEAM) by Jens Frahm [23] of which the latter is not as commonly used like the two prior named sequences. We use these three in this work, as they all vary in their basics concerning the image acquisition and all have their unique advantages and disadvantages in hindsight of e.g. acquisition velocity, robustness, energy deposition or image quality. Their functionality and behavior during measurements will be described in the next sections. To illustrate the process and the mechanism of sequences, the principles are explained with a fast-low angle-shot (FLASH) sequence first which is displayed in figure 2.3. The gradients and pulses are arranged in a chronological order. First a slice selective gradient is started up, as soon as the gradient reaches the destined amplitude the RF pulse is turned on, to only excite the spins in a certain slice. After the duration of the RF pulse the slice selection gradient is turned off. There after a re-phasing gradient is applied to counter the slice selection

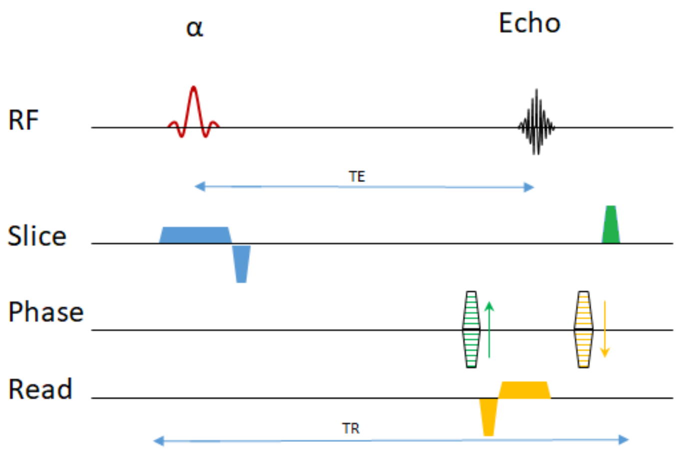

Figure 2.3: Pulse scheme of a fast-low angle-shot (FLASH) sequence. First a fast low angle shot pulse followed by a slice encoding gradient and a rephasing gradient are turned on. Thereafter a phase encoding gradient is applied in phase direction. In read-out direction a dephasing gradient shortly before the echo and a read out-gradient during the echo are played out. Thereafter in phase direction, a phase encoding rephaser and in slice direction a spoiling gradient to dephase the signal, so it does not contribute to following measurements, are applied.
As a result a single line in the k-space is measured. To acquire a full slice the measurement is repeated n-times.

gradient. It is followed by a phase encoding gradient, to encode the measured k-space trajectory, and in read out direction by a dephasing gradient to counteract dephasing effects due to the read-out gradient. If needed, to e.g. save time, it is possible to apply all three gradients at the same time. The read out gradient is applied after these three gradients to measure the spin echo occurring after an echo time TE after the excitation of the magnetization. After the read out, a gradient is applied in phase direction to turn back the phase to its initial state. At last a so-called spoiling gradient is applied in slice direction to dephase remaining signal. This method is replied n times and the phase encoding gradient is adapted each time to measure the k-space similar to the sketched examples in figure 2.2.

2.2.1 Echo-Planar Imaging

Echo-planar imaging (EPI) is a gradient echo sequence which is often used for diffusion weighted imaging (DWI) or blood oxygenation level dependent (BOLD) imaging. The sequence principle is shown in figure 2.4. A RF pulse and a slice selection gradient flip the magnetization out of its initial state. Resulting thereafter the signal decreases until it is

zero. However, if a gradient is applied, the transverse precession direction will be flipped and a new echo created. By repeating this process with switching gradients an echo train with multiple succeeding echoes can be formed. Using gradient blips in-between echoes and read-out gradients changes the phase accordingly and allows to measure the k-space as e.g. sketched in figure 2.2**(b)**. The phase encoding blips are not re-phased after each echo, like during e.g. FLASH acquisitions with the stepped phase encoding gradients.
The echo-train length during EPI depends on the signal decrease with T_2^* and the gradient switching velocity of the MRI. If the echo-train is long enough a whole slice can be measured with just one RF-excitation. Thus, this method is a rapid acquisition method, which is very useful for time sensitive measurements were motion of any kind can influence the data.
It is possible to accelerate EPI even further with methods which reduce the number of k-space lines. For example parallel acquisition method (PAT) [8, 28], partial Fourier-acquisition (PF) [56] or inner volume techniques [54, 86], of which the latter will be described in section 2.4. However, EPI is also very sensitive to magnetic flux density inhomogeneities as the phase encoding gradients used for the scanning of the k-space can be affected by small differences in the magnetic flux density, as will be shown later in this work.

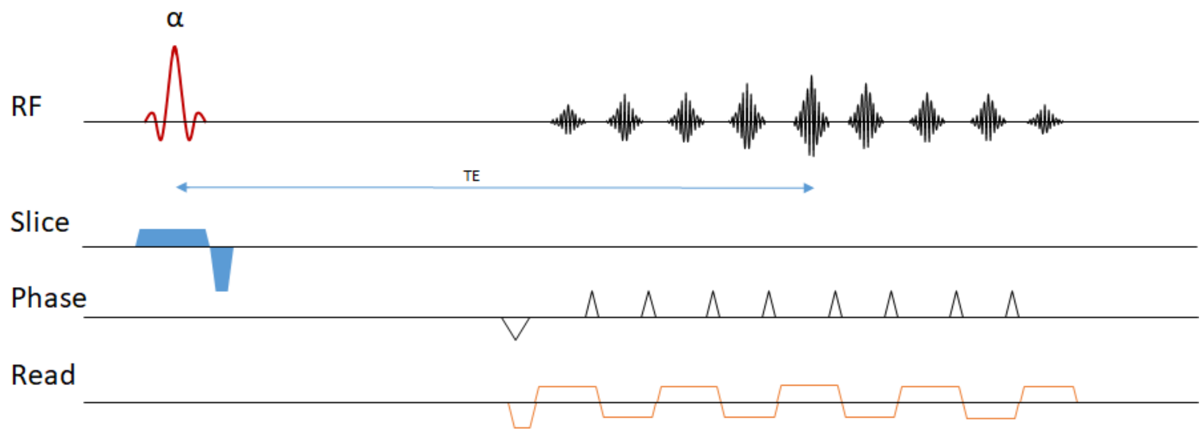

Figure 2.4: Schematic of an EPI sequence. A RF pulse and a slice encoding gradient and its rephasing gradient are turned on at the beginning. Thereafter an echo is measured to determine one k-space line. To measure a whole slice multiple echoes are measured in a row with several read out gradients, in between which gradient blips are applied to phase encode the signal.

2.2.2 Fast-Spin Echo Imaging

The fast-spin echo sequence (FSE) is based on a spin-echo sequence, where a 90 degree and a 180 degree pulse are used to excite and refocus the magnetization to create a spin echo signal by exciting and refocusing, as described in 2.1. In contrast to the spin-echo sequence during the FSE the 180 degree pulse is repeated several times. By applying 180 degree pulses after TE/2 the dephasing direction of the spins is reverted so they can overlap again after TE/2 and create an additional spin echo. This can be repeated n times and by phase encoding each of the n created echoes, different k-space lines can be measured. Resulting this can accelerate the acquisition speed by n compared to the spin echo sequence. By using PAT, PF or inner FOV techniques, the acquisition can be accelerated even further, similar to the EPI acquisitions.

Each 180 degree also refocuses the prior spin echoes and thus it is possible that several echoes occur at the same time. The signal of the echoes can overlap constructive or deconstructive, depending on the modulation of the precession motion. Additionally cumulative phase errors from repetitive 180 degree pulses and inhomogeinity effects can

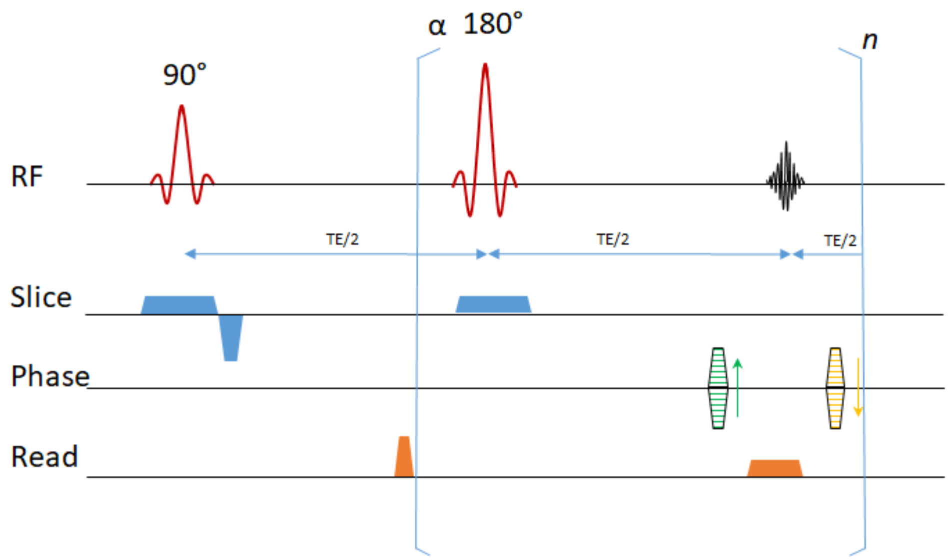

Figure 2.5: shows a fast-spin echo sequence. A 90 degree pulse and a slice selection gradient excite spatially selective the magnetization. Thereafter a gradient to rephase the slice gradient is applied. After a time TE/2 a alpha pulse of 180 degree is applied with a slice selective gradient to flip the magnetization and thus create a spin echo after another TE/2 during which a read out gradient is applied. After TE/2 an additional 180 degree pulse is applied. This is repeated n times until n k-space lines are measured. The spin-echo is additionally surrounded by phase-encoding and rephasing gradients which are varying depending on the k-space line measured.

lead to a shift in time of the echoes.
To ensure that the echoes do not interact destructively phase modulation is key. Meilboom-Gill first proposed to modulate the phase in a perpendicular manner. The pulse-related errors could be reduced if the 180° pulses are phase shifted by 90° with respect to the initial 90° and the prior 180° pulse [57]. However, in case the so called Carr-Purcell-Meiboom-Gill (CPMG) conditions [11] are violated, e.g. using DWI (see 2.3), signal loss can still occur. A possible solution is to dephase the echo after the echo read out with a strong gradient so it can not contribute to next echos. This is the so-called displaced approach [61]. However, because the previous refocused echoes are suppressed the signal intensity is greatly reduced. Another solution is the quadratic phase modulation, thereby the phase is modulated in quadratic manner so that the echoes always interact coherently [50].
As during a FSE the echos are refocused by 180 degree pulses it is a rather robust sequence and is not affected as strongly as other sequences, e.g. EPI, by magnetic inhomogeinities. The repetitive usage of 180 degree pulses can, however, lead to a high energy deposition. Thus, the specific absorption rate (SAR) might be increased and heating effects can occur. To counteract this, either the flip angle of the refocusing pulses have to be decreased or the repetition time in between the slice measurements has to be increased and thus the measurement duration is extended even though mechanically higher velocities would be possible.

2.2.3 Stimulated Echo Acquisition Mode

The stimulated echo acquisition mode (STEAM) is a measurement method which creates stimulated echoes with a chain of flip angle pulses, the general setup is shown in figure 2.6. A 90 degree pulse excites the spins due to which the magnetization starts to precess in the xy plane and the phase information changes. After TE/2 another 90 degree pulse is applied. This pulse transforms the magnetization into longitudinal magnetization [23]. This longitudinal magnetization relaxes rather slowly with the spin-lattices relaxation T_1. After a time T_M an additional alpha pulse is applied, resulting in a stimulated echo after TE/2 which can be measured. The magnetization after the second 90 degree pulse relaxes rather slowly and it is possible to "store" the magnetization. By using alpha pulses smaller than 90 degree only a part of the stored magnetization can be exited. Thus, it is possible by selecting the right flip angle pulse size, repetitive application of the pulse plus phase and frequency encoding, to measure a whole slice in a single shot. Thereby the alpha pulse depends on the desired pixel resolution, the full width at half-maximum ($\mathrm{FWHM}_{\mathrm{PE}}$) of

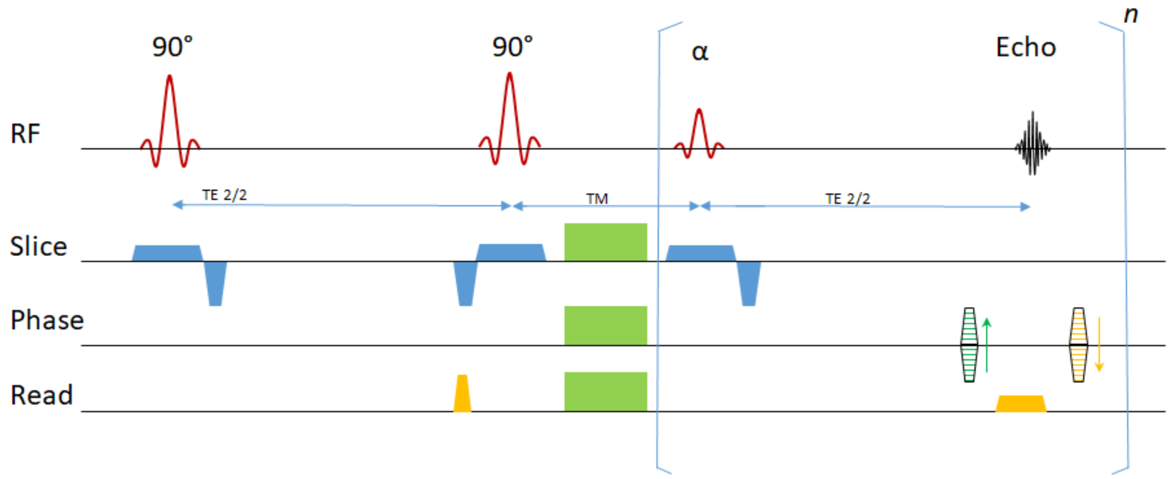

Figure 2.6: shows a stimulated echo acquisition mode sequence. A 90 degree pulse excites a slice spatially, after TE/2 another 90 degree pulse is applied, which flips the magnetization and leads to a conservation of the magnetization, as it only relaxes with T_1. After a time T_M an alpha pulse smaller than 90 degree is applied and after another TE/2 the signal is measured with a read out gradient surrounded by phase encoding gradients. Depending on the alpha pulse flip angle this can be repeated n-times to measure a whole slice.

the PSF in phase encoding direction, which is in relation with the amount of k-space lines and the distance in between them, or rather the field-of-view in phase encoding direction (FOV_{pe}). In case of full Fourier sampling it can be described by [21]:

$$\text{FWHM}_{\text{PE}} = \frac{2}{\pi} \cdot \text{FOV}_{\text{pe}} \cdot (\text{TR}/T_1 - \ln \cos \alpha) \tag{2.9}$$

It depends further on the repetition time TR, the spin-lattice relaxation T_1 and the order in which the k-space lines are measured. For example in case of a centric reordered (CRO) approach, where the first measured line is the center k-space line the flip angle is given by:

$$\alpha_{\text{cro}} = \arccos\left(\ln\left(\text{TR}/T_1 - \frac{\pi}{2}\frac{\text{FWHM}_{\text{pe}}}{\text{FOV}_{\text{pe}}}\right)\right) \tag{2.10}$$

and in case of a Half-Fourier (HF) approach the alpha pulse is given by:

$$\alpha_{\text{HF}} = \arccos\left(\ln\left(\text{TR}/T_1 - \pi\frac{\text{FWHM}_{\text{pe}}}{\text{FOV}_{\text{pe}}}\right)\right) \quad . \tag{2.11}$$

In case of the HF approach the amount of k-space lines is nearly halved, only a few phase correction center lines are measured. This reduces the acquisition time in comparison to the CRO full Fourier acquisition. However, it generally also reduces the signal to noise ratio (SNR) as less k-space lines are measured. Further during HF the k-space lines are measured in an ascending manner due to which the neighbouring k-space lines are measured successively, as a result the $\mathrm{FWHM}_{\mathrm{pe}}$ of the PSF is reduced by a factor of 2 compared to the CRO approach where between the successive lines an additional line is measured. Thus, larger flip angles can be used which results in a SNR gain in comparison to the CRO full Fourier approach [21].

2.3 Diffusion-Weighted Imaging

First discussions regarding the molecular motion in liquid or gases were carried out in the mid 19th century by Thomas Graham [25, 26, 27]. In 1855 Adolf Fick postulated that the particle current flow $\vec{J}$ is proportional to the concentration gradient ∇c opposite to the diffusion coefficient D [17],

$$\vec{J} = -D\nabla c \qquad . \tag{2.12}$$

This was later know as Fick's 1st law. The 2nd law describes the connection of local and temporal concentration differences and enables the description of non stationary diffusion. In the beginning of the 20th century Albert Einstein was able to derive Ficks law's from the thermodynamic laws and in the course of this he derived the Stokes-Einstein-relation to calculate the diffusion coefficient.

First attempts of combining diffusion measurements and spin-echo experiments in nuclear magnetic resonance (NMR) were done by Erwin Hahn in 1950. Purcell and Carr developed the possibility to measure self-diffusion in 1954 and in 1965 Stejskal and Tanner showed that pulsed gradient fields in a NMR enable the possibility to measure the diffusion motion of hydrogen nuclei [80]. Resulting one main diffusion measuring technique is named after them and a scheme of it is shown in figure 2.7. In 1985 LeBihan implemented the by Stejskal and Tanner developed method into the MRI and in 1994 he proposed together with Basser the diffusion tensor model [3]. It takes the direction dependency of the diffusion coefficient into account and enables conclusions about nerve courses in vivo.

Diffusion-weighted imaging (DWI) measures the self-diffusion of water the so called Brownian motion, which the water molecules perform due to their thermal energy. This is independent of the concentration, however, lays the foundation of Ficks laws, which

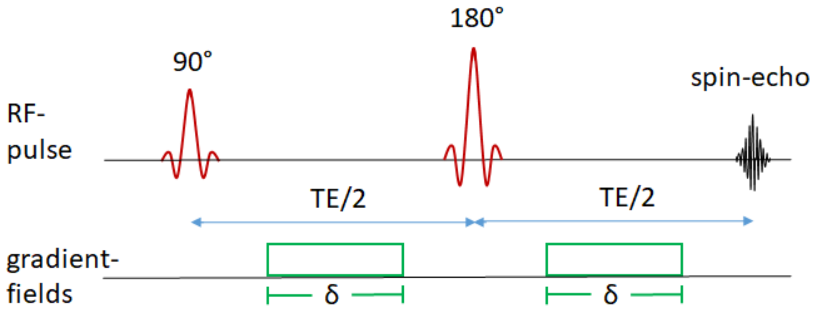

Figure 2.7: Shematic scheme of Stejskal-Tanner-sequence

describes the diffusion direction dependency.

The diffusion weighting is performed with the same physical principle as used for MRI, nuclei have a spin and align in an external magnetic flux density and with an RF excitation the state of it can be changed.

In figure 2.7 a schematic diffusion-weighted sequence is shown, more precise a Stejskal-Tanner-sequence, to describe the principle of DWI. A 90 degree pulse first flips the magnetization $\vec{M}_L$ in to the $xy-$plane applying. By applying now a gradient field δ in a given direction the external magnetic flux density $\vec{B}$ changes. As result the excited nuclei spins do not precess with the same Larmour-frequency and get dephased. A 180 degree pulse is applied to refocus the phase of the spins again. Thereafter the gradient field δ is applied again. Due to the identical frequency differences with reverse sense of rotation, the spins which did not move are again in phase and create a spin-echo, which can be measured. As the nuclei which moved along the gradient fields, are not rotated back into phase the signal strength is reduced. The signal reduction can be described by the Stejskal-Tanner-equation [80]:

$$S(\vec{g}) = S_0 \cdot \mathrm{e}^{-b\ \vec{g}^T \mathbf{D}\ \vec{g}} \tag{2.13}$$

with the signal intensity $S(\vec{g})$ under the influence of a gradient field of duration δ directed in $\vec{g}$, S_0 the signal of the non-weighted measurement, with no active gradients. b describes the strength of the diffusion weighting which is proportional to the gradients applied and the duration in between them. From the observed signal reduction a diffusion displacement can be determined. However, it is evident from the equation that to determine the diffusion motion at least one additional measurement has to be performed, typically the non-weighted measurement.

As in anisotropic media, like tissue structures, the diffusion coefficient is direction dependent

and is substituted with the diffusion-tensor **D**, a symmetric 3x3-matrix. As the matrix has 6 degrees of freedom, at least six diffusion weighted measurements with varying directions, gradients, are necessary to determine the tensor with equation 2.13, besides the non-weighted measurement. As the accuracy is restricted due to noise and artifacts, often additional directions are measured and or the measurements are repeated several times.
As the water molecules are hindered in their motion in vivo, e.g. in brain tissue by cell membrane, they can move more freely along axons than across them. Thus, the general assumption that the diffusion coefficient reflects the direction of the nerve fibers can be drawn. However, it has to be proceeded with care as the diameter of the axons is below the measurement resolution thus the measured signal only represents an average over a certain volume.
The diffusion in vivo is typically displayed with different images. One is in form of an isotropic diffusion-weighted image (DW_{iso}) which is the trace of the diffusion-tensor **D** and thus also called trace weighted image. A different one is the so called apparent diffusion coefficient (ADC) or ADC map which represents the the diffusivity in a voxel by acquiring multiple diffusion weighted images with different amounts of diffusion weighting. The change in signal is proportional to the rate of diffusion. Further a fractional anisotropy (FA) image is often used, it corresponds to the scalar measure of the degree of anisotropy in a given voxel. It is often also color-coded (Col-FA) where the colors represent the orientation of the fibers: red for left-right oriented fibers, blue for superior-inferior oriented fibers and green for anterior-posterior oriented fibers.

2.4 Inner Field-of-View Acquisition

In case small regions, like the spinal cord or the optical nerve, are of interest a high resolution is necessary. It is not sufficient to just decrease the field-of-view (FOV), the phase-encoded dimension of the MR-signal must be smaller than the imaged FOV, otherwise the signal outside the FOV can get aliased into it. This would lead to an overlap of tissue regions, as explained in section 2.1. As solution 1985 Feinberg et al. introduced inner volume MRI with cross-sectional excitation's [16] which was further developed by for example Wheeler-Kingshott or Mansfield later on [54, 86]. The principle behind this technique will be explained in the following section. Another possible solution was brought up by Bottomley and Hardy in 1987, the so called 2D-selective RF excitations which are going to be explained thereafter [7].

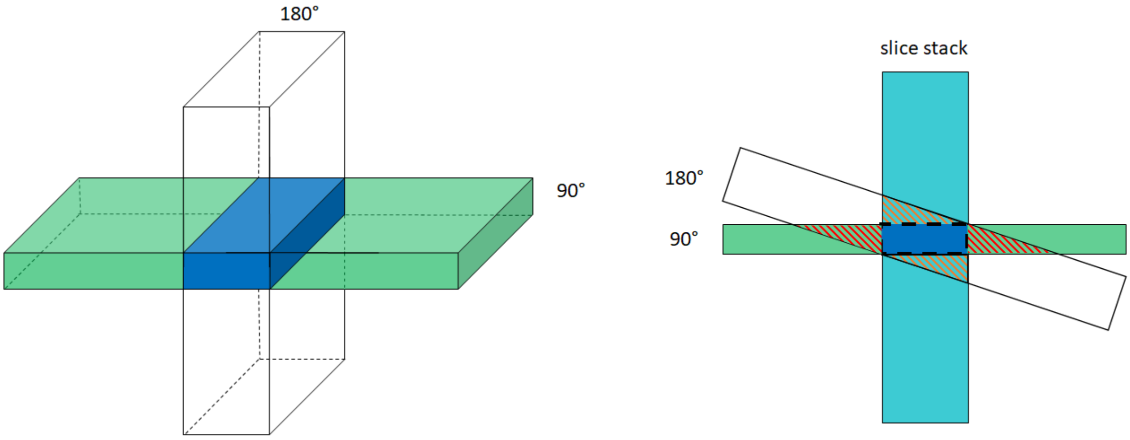

(a) (b)

Figure 2.8: (a) Sketch of cross-sectional inner volume principle [16]. The 90 degree pulse is displayed as green box and the 180 degree pulse as colorless. The blue box represents the excited and measured volume. In **(b)** the cross-sectional ZOOM inner volume is sketched [87]. In teal the stack to be measured is shown, in green the 90 degree pulse and in colorless the tilted 180 degree pulse. The blue square represents one slice to be measured. The red and orange highlighted areas are the so called transition zones. The red regions get refocused as well and the orange regions can lead to saturation effects if a slice stack is measured.

2.4.1 Cross-Sectional RF Excitations

The idea by Feinberg et al. is to excite and refocus a volume with two spatially selective RF-pulses which are orthogonal to each other to increase the spatial resolution. A 90 degree pulse excites the spins in one slab and a 180 degree pulse inverts the spins with an orthogonal excited slab in the volume of interest. Thus, a spin-echo arises only in the cross-section. The method is sketched in figure 2.8**(a)**. The blue box represents the volume in which the nuclei spins are excited and inverted by the 90 and 180 degree pulse. An advantage of this technique is that the neighboring tissue can not contribute signal, by e.g. folding artifacts. In addition the measurement time is reduced, as less k-space lines have to be measured. However, the selective excitation in an orthogonal manner has the disadvantage, that if more then one slice shall be measured, between consecutive acquisitions time has to pass. The reason is that the magnetization has to relax back into the initial state, as else multiple excitations of the same area can lead to a significant signal loss.
To address this problem Wheeler-Kingshot et al. proposed the so-called zonal oblique multi-slice (ZOOM) technique [87]. It is based on the same principle as the approach by

Feinberg et al. but instead of exciting the slice with two orthogonal selective pulses, the pulses are rotated by an angle $\phi < 90°$ to each other. Thus, only a small area of the slice stack to be measured is excited. The two pulses still excite additional areas so-called transition zones. The size of the transition zone, however, can be manipulated by varying the thickness of the pulses and the rotation angle. Using now a gap of the size of the transition zones in between consecutive measured slices and or measuring in an interleaved, in case the transition zone thickness is smaller than a slice, enables to measure a slice stack without overlapping of pre excited slices (see Fig. 2.8**(b)**). Further to prevent folding artifact due to the transition zones in phase direction phase oversampling can be used to suppress artifacts.

2.4.2 2D-Selective RF Excitation

The in 1987 by Bottomley and Hardy proposed 2D-selective RF-excitations (2DRF excitations) are created by applying temporally variable gradients while RF-pulses with specific envelopes are played out (see Figure 2.9 a) [7]. This variability enables excitations of form and region of choice, e.g. circle, rectangle and so on. As the region to be excited is usually known and thus the magnetization $M_{xy}(\vec{r})$ as well, the 2DRF excitation $B_1(t)$ needed to excite $M_{xy}(\vec{r})$ can be inversely calculated with the small angle approximation and the assumption that the system is in thermodynamic equilibrium before the excitation. The

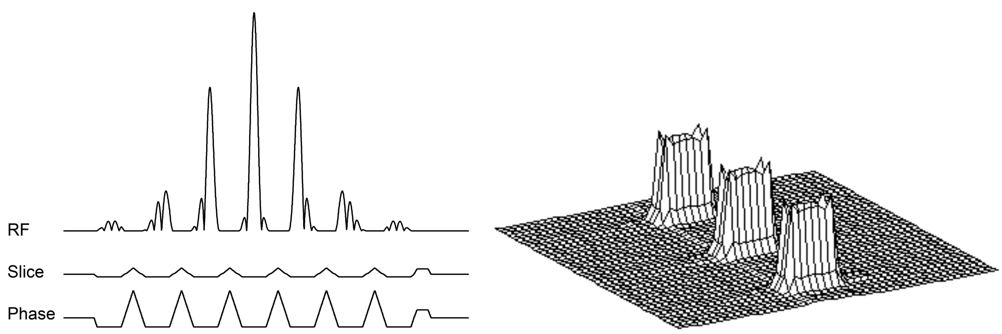

(a) **(b)**

Figure 2.9: (a) displays the temporal course of a blipped planar 2DRF excitation and the applied gradients. **(b)** shows an excitation profile of a square 2DRF pulse with side excitations which occur due to the discrete and finite sampling of the k-space.

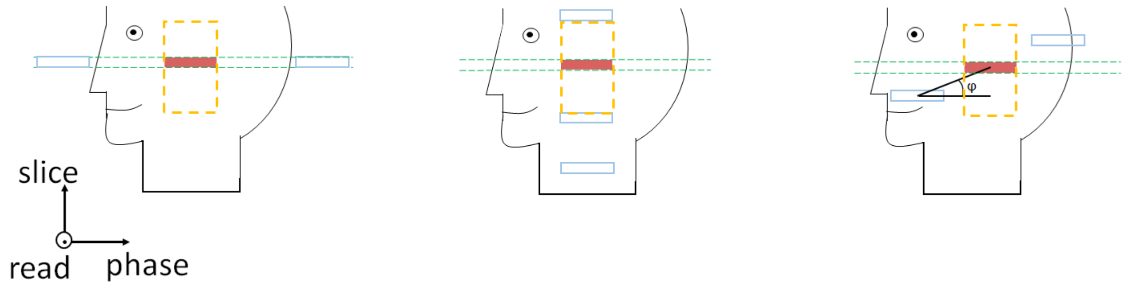

(a) **(b)** **(c)**

Figure 2.10: In the figures red squares represent the areas of interest, that are excited by a 2DRF excitation and blue squares represent the side excitations. In **(a)** the side excitations are shifted out of the subject to be examined. In **(b)** the collinear approach is shown in which the side excitations are placed in slice direction out of the stack to be measured. In **(c)** the side excitations are shifted by an angle ϕ in the dead corners were neither a slice to be excited or a possible refocussing pulse is applied, which is sketched by the green dotted lines.

excitation is given by [64]

$$B_1(t) = -i|\vec{G}(t)| \int_{\vec{r}} \frac{M_{xy}(\vec{r})}{M_0} \mathrm{e}^{i\vec{r}\ \vec{k}(t)} \mathrm{d}\vec{r} \tag{2.14}$$

where $\vec{G}(t)$ is the amplitude of the gradients and $\vec{k}(t)$ is the k-space trajectory. It is similar to 2.7 but varies in the integration limits:

$$\vec{k}(t) = \gamma \int_t^T \vec{G}(t')\mathrm{d}t' \quad . \tag{2.15}$$

By Fourier transforming the desired profile and combing it with a k-space trajectory, e.g. blipped planar (see Figure 2.2), the desired envelop $B_1(t)$ can be determined. The transformation of this envelope back into the spatial domain results in the true 2DRF excitation profile. Due to the finite and discrete scanning of the k-space the desired excitation can not be completely achieved, so-called side-excitations occur, as shown in figure 2.9**(b)**. A side-excitation excites a region of the same shape as the main excitation. Thus, the side excitations have to be considered during measurement and positioned carefully as they can lead to saturation effects and or folding artifacts. Therefor the k-space trajectory has to be adapted depending on the area to be measured and the positioning of the side excitations, which can prolong the excitation duration.

There are different possibilities to place the side excitations during the measurements. All have the similarity that the side-excitations are placed outside of the stack to be measured. One possibility is to place the side excitations perpendicular to the slice stack, thereby the side excitations at least have to be placed in regions which do not generate a signal, e.g. air, to prevent folding artifacts. (fig. 2.10**(a)**). Another way ("colliniear") is to shift the side excitations along the slice stack axis outside the slice stack to be measured (fig. 2.10**(b)**). These two methods can lead to rather long excitation durations as the number of trajectory lines increases with increasing distance of the side excitations to the main excitation. The third approach ("tilted") is a combination of the previous two and similar to the approach used in case of cross sectional excitations. By rotating the trajectory in respect to the slice- and phase-encoding direction the side excitations occur in a dead corner and are neither refocused, nor do they interfere with other slices to be measured (fig. 2.10 **(c)**) [20].

2.5 Simultaneous Multi-Slice Acceleration

Already in 1980 Maudsley proposed simultaneous multi-slice (SMS) imaging as a good tool to improve line-scan imaging [55]. In 1988 Müller even proposed to generate radio-frequency pulses needed for SMS excitation's by applying the Fourier shift theorem. However, due to the technical properties of MRI at that time the disentangling of the images was rather difficult and it did not get much attention. First with the introduction of coil sensitivity profiles, to disentangle simultaneously acquired signal in relation with parallel imaging techniques [28, 66], and the availability of receiver coils with a coil distribution in z, SMS imaging was brought fore again and became a cornerstone of MRI nowadays. The principle idea behind SMS imaging is to excite two or more slices simultaneously. This is done by summing up multiple RF waveforms with different phase modulations [2]

$$P(t) = \mathrm{e}^{i\Delta\omega t+\phi} \tag{2.16}$$

with the slice position $\Delta\omega$ and the phase ϕ. This results in a multiband (MB) pulse:

$$RF_{MB}(t) = A(t) \cdot \sum_{N} \mathrm{e}^{i\Delta\omega_n t+\phi_n} \tag{2.17}$$

where $A(t)$ corresponds to a standard complex RF waveform.
Two technical problems can occur during the design of the $RF_{MB}(t)$. First, as several slices are excited at the same time $RF_{MB}(t)$ is prone to exceed the special absorption rate (SAR) limit. Second, $RF_{MB}(t)$ is prone to exceed the peak amplitude capabilities of the

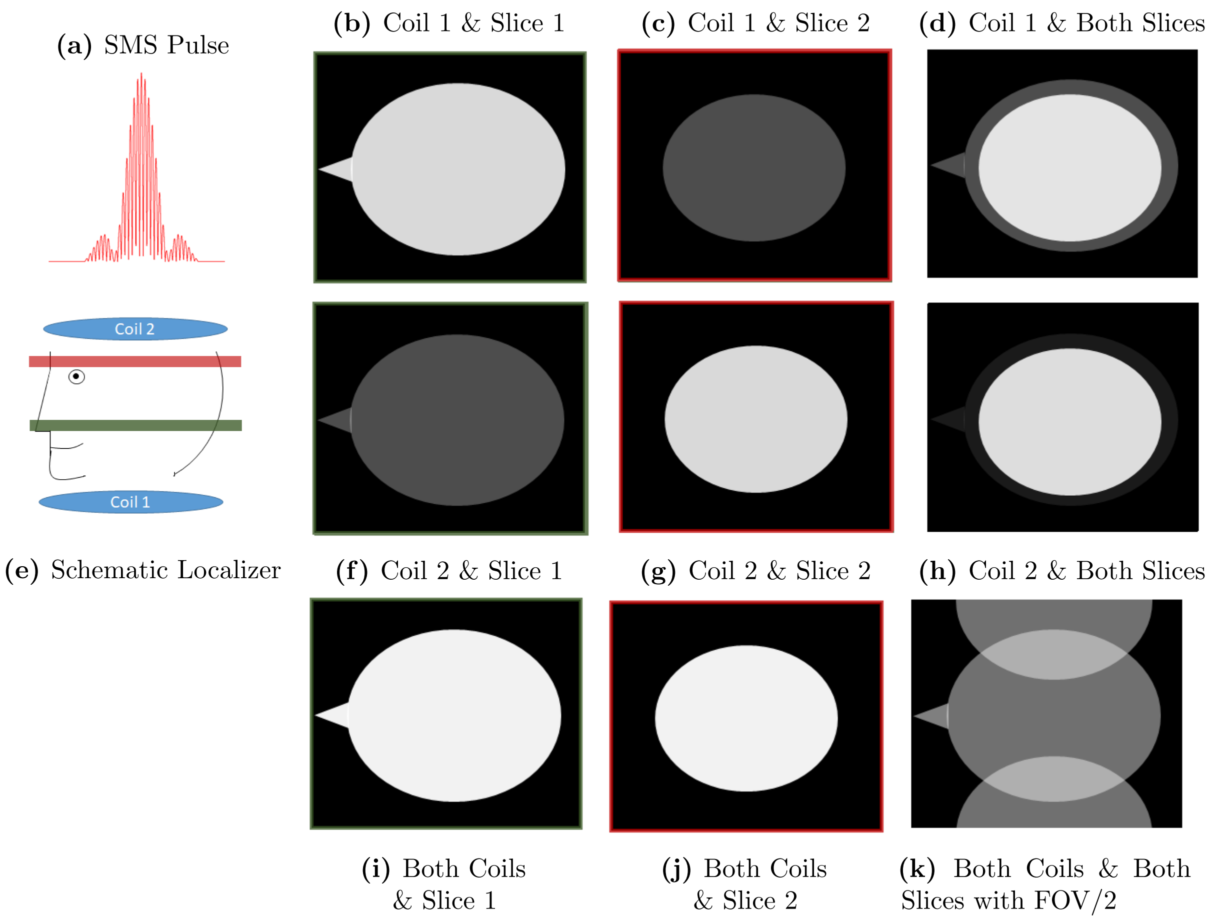

Figure 2.11: **(a)** shows the profile of a RF pulse which can excite two slices simultaneously. The RF modulation leads to the excitation of two slices which can be measured with two different coils as sketched in **(e)**. When the signal of one slice is measured depending on the respective position to the slice the intensity varies. This is sketched for coil 1 located beneath the object in **(b)** and **(c)** and for coil 2 in **(f)** and **(g)**. The lower the distance to the slice the higher is the signal measured. In case one coil measures both slices at the same time, the signal overlaps, as sketched in **(d)** and **(h)** for the respective coils. If both coils together now acquire the signal of both slices at the same time an image with both slices uniformly overlapping would be acquired. By applying a FOV/2 phase gradient modulation a shift can be exerted and thus the slices are shifted by FOV/2 to each other and thus both coils together acquire an image with overlapping signal, however, the slices are shifted, as sketched in **(e)**. With the combination of RF coil encoding the image can now be disentangled and each slice can be reconstructed so that two single images are acquired **(i,j)**. Details explained in the text.

RF amplifier.

A possible solution is to increase the duration of the RF pulse, while holding the bandwidth time product and the flip angle constant. This, however, can prolong the measurement time and off-resonance effects can have a stronger effect, due to the decreased bandwidth. One possible method to decrease the SAR is variable rate excitation (VERSE) which varies the slice selection gradients with time depending on the RF pulse to reduce its peak amplitude [14]. There are further methods to reduce the SAR, e.g. power independet of the number of slices (PINS) [47] or parallel transmission and SMS [29, 65].

The spatial encoding of SMS excitations can be performed with different approaches: Coil encoding, RF phase encoding, gradient phase encoding and combinations of them.

Coil encoding disentangles the signal intensity in one direction depending on the distance in between the multiple excited slices. Depending on the signal strength a coil measures, it can be determined from which slice the signal origins. Thus, it is possible by combining the information of several coils to create images of each slice.

RF phase encoding is realized by applying phase gradients to the RF pulse. In case of SMS this can be realized by applying individual phase cycling patterns for each frequency band. This causes an image slice to be shifted in the FOV to different locations along the phase encoding direction. To prevent folding artifacts a FOV N times larger than the FOV of a single slice is needed. Further each slice measured needs to be shifted by a unique integer multiple of the FOV.

Gradient phase encoding can be performed by phase encoding along the slice direction.

Often coil encoding and phase encoding is combined which enables the possibility to shift the simultaneous excited slices in a controlled manner. This can reduce the overlap in between aliased slices, increase the distance between overlapping voxels and causes the slice separation to partially rely on coil sensitivities along the in-plane phase-encoding direction. As a result the coil sensitivity encoding can be shared arbitrarily between the both directions (k_y, k_z) [2]. This concept is also called CAIPIRINHA [8].

In figure 2.11**(a)** a MB pulse to excite two slices, as sketched in **(e)**, is shown. The excited slices can be measured with each coil individually, as sketched **(d,h)** or they can get measured by several readout coils and shifted by FOV/2 by phase encoding gradients, as sketched in **(k)**. From this combined image the excited slices can be disentangled with the information on the signal strength from the coils, as sketched in **(i,j)**. The SNR efficiency is improved by $\sqrt{N}$ with N the number of slices acquired, as N slices can be acquired in the same time as normally one slice [2].

2.6 Metallic Artifacts in Magnet Resonance Imaging

Generally the human body consists of various tissue structures which differ in their magnetic susceptibility [34]. Most tissues are diamagnetic and thus reduce an external magnetic flux density slightly, however, paramagnetic tissues increase it and ferromagnetic materials, like iron or cobalt, amplify the magnetic flux density. Thus, if metallic implants are present in vivo an increased magnetic flux density can be observed. The metallic implants induce perturbations to the static magnetic flux density B_0 as well as to the spatial encoding used for MRI [76]. The field variations thereby depend on the size, shape, the orientation in the field, the type of metal and in particular the magnetic susceptibility χ [51]. The perturbations lead to a variation of the resonant frequencies near the object depending on the susceptibility of it and lead to artifacts. The predominant artifacts which can be observed are: Signal loss due to dephasing, saturation due to fat-suppression and displacement artifacts [34].
In the absence of relaxation or chemical shifts the spatial encoded imaging signal of a thin two-dimensional slice is given by [45]:

$$S\left(k_x, k_y\right) \propto \int_{xy} \rho(x,y) \mathrm{e}^{2\pi i\left[k_x\left(x+\frac{2\pi\Delta v_0(x,y)}{\gamma G_r}\right)+k_y y\right]}\ dx\ dy \tag{2.18}$$

where k_x and k_y are, respectively, read-out and stepped phase encoded dimensions, G_r the amplitude of the read-out gradient and $\Delta v_0(x,y)$ describes the frequency offset induced by the static field inhomogeneity with

$$\Delta v_0(x,y) = \frac{\gamma}{2\pi}\Delta B_i \tag{2.19}$$

where ΔB_i is the magnetic flux density inhomogeinity.
In equation 2.18 it can be observed that the encoding relationship k_y is not affected by the frequency offset. This means that conventional phase encoding with stepped gradients is not affected by inhomogeinities of B_i. For blipped phase encoding as used during e.g. EPI, however, this is not the case, the distortion in k_y would be needed to be considered for equation 2.18 [46].
Using the Fourier shift-theorem the read-out encoding dimension is distorted by:

$$\rho(x,y) \xrightarrow{\Delta v_0(x,y)} \rho\left(x - \frac{2\pi\Delta v_0(x,y)}{\gamma G_r}, y\right) \tag{2.20}$$

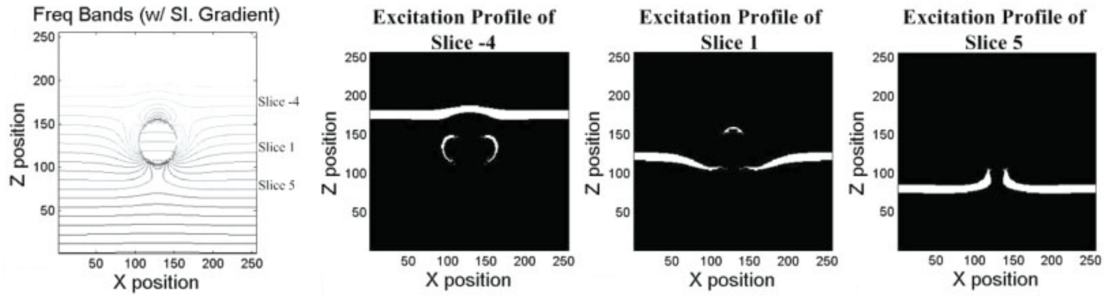

(a) **(b)** **(c)** **(d)**

Figure 2.12: It shows the influence of a metallic screw on the signal on measured slices. In **(a)** the excitation profiles corresponding to the frequency bands, which are influenced by field inhomogeneities overlapping with the frequency of the slice selective gradients, are displayed. **b-d** show distorted excitation profiles which point out that spins get excited if their precession frequency falls into the frequency band of the excited slice. This leads to through-plane distortions due to spins excited of a different slice position by the slice excitation. Illustration by Lu et al. [53].

Further B_i influences the slice selection gradients. As the selection is performed by a gradient G_z with a frequency of $v_{rf} = v_0 + \frac{\gamma}{2\pi} G_z z_0$ to excite a slice in the range of $z_0 - \delta z/2 < z < z_0 + \delta z/2$. However, due to the frequency offset Δv_0 induced by the implants, the spins are excited in a range of:

$$z_0 - \delta z/2 < z + \frac{\Delta v_0(x,y,z)}{\Delta v_{rf}} < z_0 + \delta z/2 \qquad . \tag{2.21}$$

The interactions of magnetic flux densities and implants lead to geometric distortions which result in a displaced localization of a voxel.
The distortions due to a metallic implants were illustrated by Lu et al. [53] in figure 2.12. They calculated the influence of a cylindrical metallic object on the magnetic flux densities and measured slices. Thereby it is observed that the distortion of a slice and its signal strength also vary depending on the distance to the object. In case multiple Implants, e.g. screws, are present the calculation gets complicated, as each screw influences the external magnetic flux densities and interacts with the additional implant and their distortion and thus multiple effects must be considered.

2.6.1 First Artifact Reduction Steps

The artifacts near metallic implants are severe, however, by carefully selecting the parameters and the techniques used the image quality can already be increased.

The signal loss and the resulting dark areas arise due to the rapid change of the static magnetic flux densities and the resulting signal dephasing. A possible solution to counter the dephasing is to use spin echo techniques with 180° refocusing pulses, to reverse the dephasing due to the magnetic inhomogeinities.

Problems due to chemical shifts or the frequency difference between water and fat can be addressed with spectral selective suppression [41], multiple echo separation techniques, like Dixon separation [15] or short-TI inversion recovery (STIR) [10]. These techniques help to provide decent images at certain distances from the metallic implants, however, in the close vicinity they are not sufficient and fail [46].

By using thin slices the spatial distortions can be decreased. The reason there for is that in slice direction the distortion is the ratio of slice bandwidth to frequency, multiplied by the slice width. However, this increases the measurement time, as more slices need to be measured to cover the same volume of interest and the SNR is reduced as the voxel size is reduced.

Maximizing the bandwidth during slice selection and read-out can reduce the distortion effects as well. This is because of the inverse proportionality of the spatial distortion, affecting read-out and slice selection, to the gradient strength, which scales with the bandwidth. However, increasing the bandwidth comes with the cost of reduced SNR.

2.6.2 View-Angle Tilt Imaging

The artifacts, caused by displacements, which can be observed in-plane include geometric distortions, signal loss and pile up artifacts. In case the frequency error is known the displacements due to off-resonance can be predicted. In case of smooth frequency errors the displacements can be fixed under the assumption that one frequency offset is representative for each voxel. This is done by measuring with field mapping techniques and reconstructing the image to correct the geometric distortions [34]. However, rapid spatially-varying frequency offsets which lead to pile-up and signal loss can not be resolved by field mapping. 1988 Cho et al. [13] thus introduced a powerful tool called view angle tilt (VAT), to reduce these artifacts. VAT uses the fact that both the slice and in-plane displacements due to off resonance are known and have a constant ratio. Thus, by replaying a slice selective gradient, the off-resonance is limited to the RF bandwidth [34]. The slice-selection gradient is applied while the read-out gradient is played out, as result the read-out plane is tilted

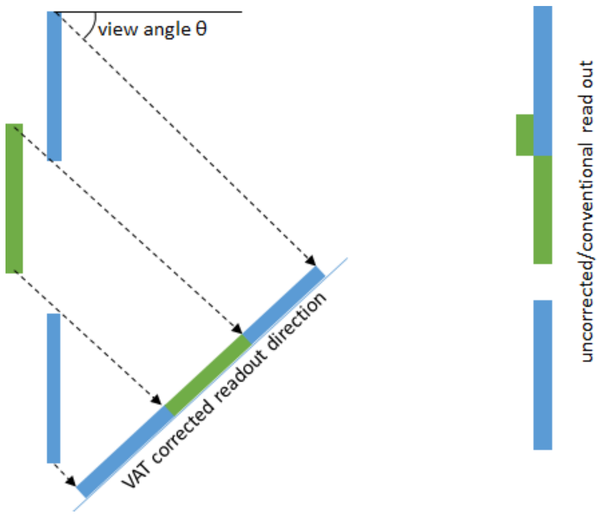

Figure 2.13: simplified VAT scheme for inhomogeneity correction method. On the left three tissues with varying overlapping frequencies are shown. This results during standard readout in signal cancellations and pile up artifacts, as sketched on the right. By applying an angle θ a tilt of the readout is achieved and a corrected image can be acquired with no overlapping signals, as sketched in the middle of the figure.

by an angle [13, 46]:

$$\theta_{Vat} = \tan^{-1} \frac{G_z}{G_x} \tag{2.22}$$

As result the slice displacements cancel out the in-plane displacements exactly, so the in-plane displacements are removed, as sketched in 2.13.
As the readout duration is limited to the duration of the RF excitation, as else blurring can occur [9], VAT is also limited. To reduce residual artifacts form the voxel tilting and blurring, a high read out bandwidth is desirable during VAT.

2.6.3 Correction of Slice Direction Distortions

Two methods to correct distortions in slice direction due to resonance frequency offsets near metallic objects are slice-encoding for metal artifact correction (SEMAC) and multi-acquisition variable-resonance image combination (MAVRIC).
SEMAC uses limited spatial bands with multiple excitations to excite the full volume of interest with a 3D spin echo acquisition to resolve distortions in slice direction. SEMAC utilizes a VAT protocol with a large read out bandwidth to reduce blurring and to minimize the temporal acquisition window, as discussed in the previous section. To compensate

slice selective distortions, additional phase-encoding gradients are added in slice direction prior to the signal read out. As result the distorted slices acquired with VAT are sub encoded with additional phase information. By registering the additional sub encoded measurements of each slice with one another and summing them up, by linear summation or sum-of-square combination, a distortion corrected image can be reconstructed [53]. The number of sub encoded measurements thereby depends on the distortions induced by metallic objects, as they need to span the expected distortions experienced in slice direction.

MAVRIC uses similar to SEMAC multiple excitations to correct through-slice displacements, however, MAVRIC does not use slice selective excitations but at least one frequency selective excitation. The RF frequency bandwidth is limited by the maximum RF amplitude and the RF power or specific absorption rate (SAR). Thus, the range of frequency offset which is acquired at one time with a frequency selective excitation and a standard imagining read out, is limited as well [45]. To acquire the full range of the frequency offset Δv_0 induced by a metallic object, the spectral distribution is separated into discrete and independent bins. The bins are measured individually with different transmission and receiver frequencies in an incremental manner to avoid saturation effects. The MAVRIC subimages (spectral bins) are combined by averaging or maximum intensity projection to an image which has minimal artifacts and includes signal from a wide range of frequency offsets near metal.

Both MAVRIC and SEMAC combined with VAT can correct both in-plane and through-slice displacements, at the cost of increased scan time. The feasibility of combinations with other techniques, e.g. fMRI or DWI, has yet to be investigated.

Chapter 3

Experimental Setup

This chapter presents the general setup of this work.
The structure and the specifications of the magnetic resonance tomograph used for the investigations in this thesis are explained, followed by the receiver coils which are used. The description of the different phantoms is given. They are used for performance and functionality test of the the sequences before they are applied in vivo. A few volunteers with and without metallic implants which were examined in the scope of the study are presented there after.
A selection of metallic implants often utilized near the spinal cord and their behavior are described. Closing, the programs used for sequence programming and data analysis are presented.

3.1 The Magnet Resonance Tomograph

The magnet resonance tomograph (MRT) used in the scope of this work is a Siemens Magnetom 3T PrismaFit [79]. It is shown in figure 3.1. In **(a)** the complete MRT setup is shown and beneath in **(b)** the core of it is shown. The MRT has a length of 198 cm with a bore size of 60 cm and a total weight of 13 tons during operation. The bore is surrounded by gradient coils which have a maximum amplitude of 80 mT/m with a slew rate of up to 200 T/m/s in all three axes. Around the gradient coils a superconducting coil is placed, which is surrounded by two cooling shields to reduce the temperature.
The MRT has 64 independent receiver channels that can be used simultaneously in a single scan. The channels can be connected with different receiver coil setups. Three setups, which were used in this work, are shown in figure 3.1 **(c)**- **(e)**.
First in **(c)** a 64-channel head neck coil is shown with which signal can be obtained in the brain and the upper region of the cervical spinal cord in the head neck area. Second in **(d)**

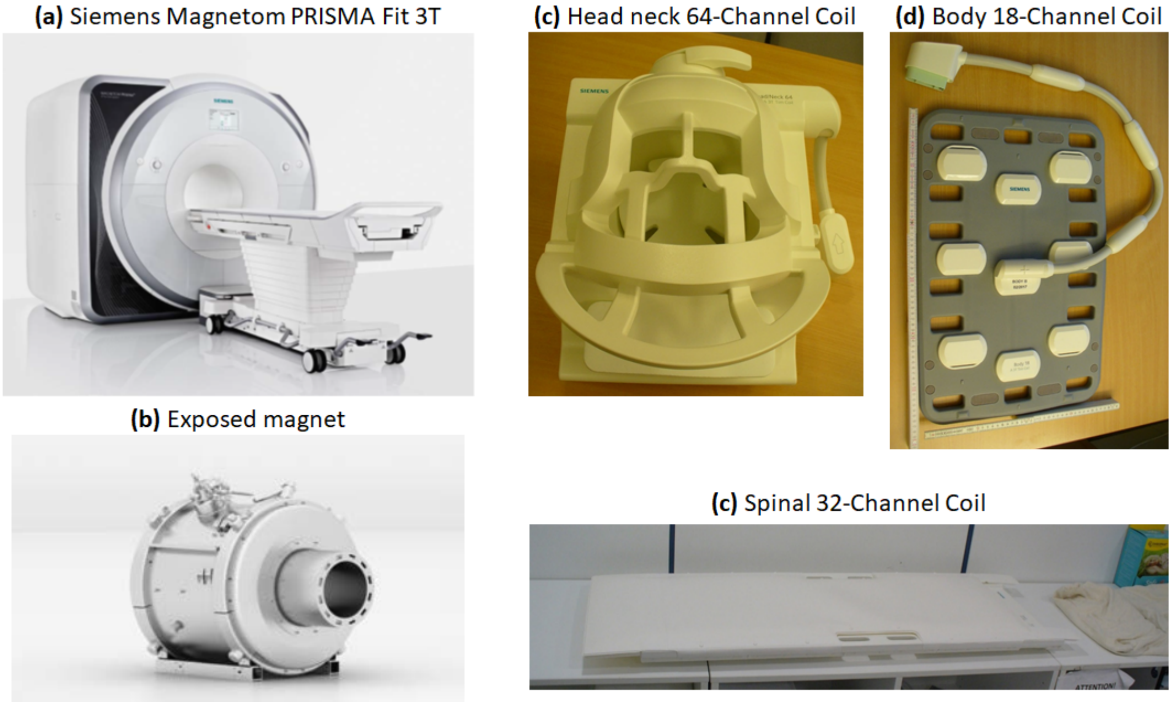

Figure 3.1: **(a)** shows a vendor image of the Siemens Magnetom PRISMA Fit 3T which is used in this work [79]. Beneath in **(b)** the inner life of it is shown which consist of a cooling system surrounding a superconducting coil and a gradient coil. Further three different receiver coils which were used in the scope of this work are shown on the right side of the figure: First a 64-channel head neck coil **(c)**, second a 18-channel body coil **(d)** and below a 32-channel spinal coil **(e)**. These three coils can be applied at the tomograph and combined depending on the region of interest investigated.

an 18-channel body coil is displayed. The position of it can be adapted above or beneath the subject in any body region, depending on the part investigated. In **(e)** a 32-channel spinal coil is presented. It can be inserted into the patient table and can be used to investigate the thoracic and lumbar spinal cord. Depending on the region of interest the coil elements with significant signal contributions were chosen for the acquisition.

3.2 Phantoms and Volunteers

The sequences and their behavior were first investigated at phantoms before they were applied in vivo. The different phantoms used are shown in figure 3.2. First we have simple cylindrical and spherical bottles filled with water or water doped with $NiSo_4$ (**a**, **b**). These phantoms were mostly used for the investigation concerning the 2DRF simultaneous

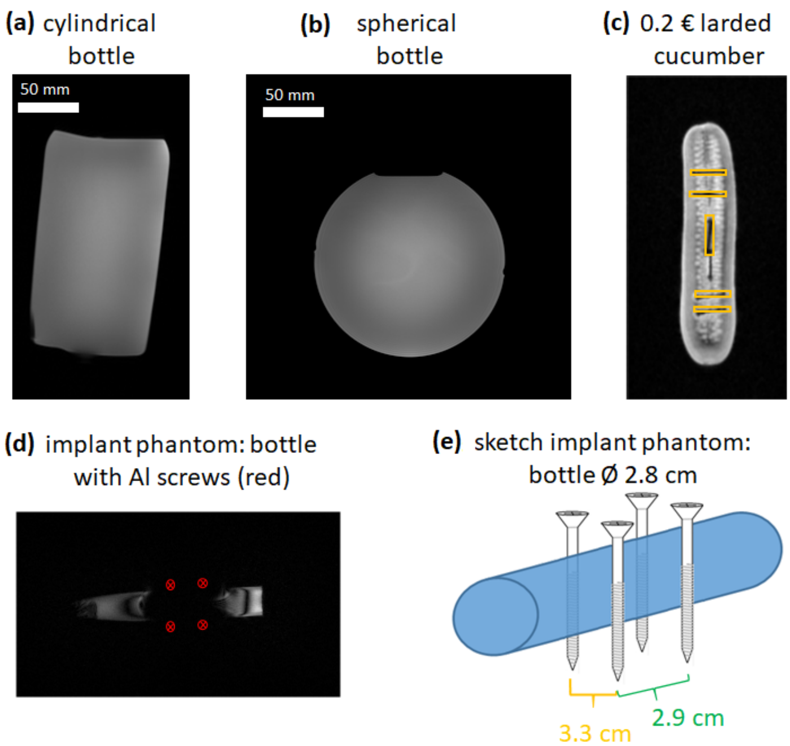

Figure 3.2: shows the phantoms used in this study. First the Fast-low-angle shot (FLASH) localizers of bottles used for standard measurements are presented, a cylindrical **(a)** and a spherical **(b)** bottle. The bottles contain water or doped water and are utilized for performance and functionality investigations.
In **(c)** a localizer of a cucumber larded with five 0.20 euro coins, highlighted by yellow rectangles, is presented. The setup was used to get first results for measurements near metallic objects. **(d)** FLASH localizer image of the phantom for detailed measurements near metallic objects, prepared with 4 screws, as pointed out by the 4 red crossed circles. In **(e)** the details of the phantom used are sketched. It consists of a water bottle with a diameter of 2.8 cm which can be surrounded by up to 4 Al screws with a distance of 2.9 and 3.3 cm.

multi-slice diffusion weighted EPI. For FSE and STEAM they were utilized for signal optimization before the sequences were applied at more complex phantoms. We larded a cucumber with five 20 euro cent coins (**c**) to test the influence of metallic artifacts on the sequences and the images obtained. Further a water bottle was prepared with the possibility to append up to four aluminum screws right next to it. The water bottle has a diameter of 2.8 cm to approximate the size of the spinal cord. This setup was chosen as many implants used near the spinal cord contain metallic screws, two possibilities are presented in figure 3.3. They are often used to either fixate or stabilize the spinal cord after an injury. They can be extended and or combined at will, to e.g. a set of 12

(a) (b) (c)

Figure 3.3: presents three different implant types of the vendor Foyomed Medical Instruments [22]. First in **(a)** a combination of six screws and 3 poles out of titanium which are connected with each other. In **(b)** 3 different titanium cages, varying in size, can be seen and in **(c)** a titanium plate with 4 screws. These implants can always be extended and combined arbitrarily, depending on the utilization in vivo.

screws connected with plates and or bars, depending on the injury of the patient. Further titanium cages are often used to stabilize the inter vertebral disk which are shown in **(b)**. Two volunteers with similar implants implanted are shown in figure 3.4. There FLASH localizers of volunteers, who were investigated in the scope of this thesis, are presented.
The first image shows a localizer of a volunteer with no implants or injuries near the spinal cord. In the scope of this work several healthy volunteers were investigated for the inner FOV simultaneous multi-slice diffusion weighted EPI study. Further FSE and STEAM were investigated to be able to compare the performance of the sequences in patients with and without implants. In image **(b)** a localizer of a volunteer possessing an implant in the larynx region near the spinal cord is shown. In this instance the patient has a cage implanted, like shown in 3.3 **(b)**. The cage stabilizes the cervical spine area and seems to only slightly influence the image quality, which will be further illuminated later in this work.
In the next localizer image **(c)** a volunteer, who has an implant containing six screws and several metallic bars connecting them, is presented. The implant is similar to the one shown previously in figure 3.3 **(a)** and stabilizes the spinal cord in the lumbar region. In the scope of this work further volunteers were investigated with similar implants, or even more complex constructions, e.g. a combination of bars, plates and screws. The reasons for the implantation thereby varies, e.g. paralysis, cancellous bone etc., as well as the region of the implant. In this work we always customized the imaging area to record an area which was corrupted by image artifacts, as well as an unaffected area in one imaging stack.
All the volunteers investigated in this study were informed of the nature of the procedure

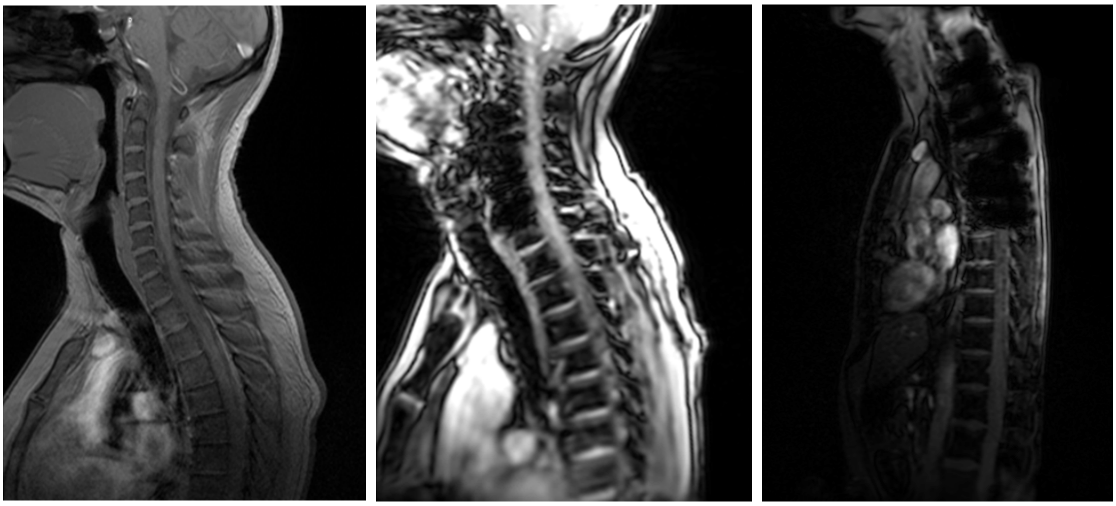

(a) **(b)** **(c)**

Figure 3.4: (a) shows an FLASH MRI image of a volunteer without metallic implants, more accurately the cervical spinal cord and parts of the cerebellum. In **(b)** a volunteer with a cylindrical metallic cage implant (see Fig. 3.3**(b)**), in the area of the larynx in front of the spinal cord is presented. In **(c)** a FLASH image is shown, of a volunteer with several titanium screws and connecting poles (see Fig. 3.3**(c)**) implanted in the lumbar region around the spinal cord.

and their written consent was obtained prior to the examination. Further the investigations of the volunteers were approved by the REB.

3.3 Pulse Sequence Programming and Data Analysis

To program the sequences MR IDEA VE11 provided by Siemens Healthineers was used. It enables the possibility to operate different RF pulses and gradients, as well as the reconstruction of data. The sequences programmed in IDEA are based on C++ code which is written in Microsoft Visual Studios 8.
The EPI sequence used in this work was already available in the work group. The STEAM and FSE sequences were programmed completely new. The sequences were grown gradually: First, the basic sequences, without any additional techniques were constructed. Second, the basic pulses were implemented and calculated, the gradients and their chronological order were defined. Third, energy calculations and safety measures were implemented. Thereafter the functionality was simulated and checked at phantoms in the MRI. After successfully probing the sequences they were combined with additional techniques which could be useful in the scope of this work, e.g. Fourier sampling, spoiling gradients. After

additional testing they were then combined with a diffusion module, which already existed in the group. It enables the use of different diffusion techniques, e.g Stejskal-Tanner or double Spin-Echo, multiple diffusion weighted directions and different gradients. Thereafter, first in vivo measurements were performed to ensure that everything is working.
The procedure of implementing a technique and proving its functionality was repeated for the simultaneous multi-slice acceleration module, consisting of RF pulse calculation and their phase modulation. Further the different modules for the inner-FOV techniques, 2DRF and ZOOM excitations which already existed in the institute, were implemented as well. Finally, the sequences were combined with MAVRIC and VAT, which were programmed from scratch.
To prevent technique combinations which are not viable together, e.g. 2DRF and ZOOM excitations, and to enable the possibility to also use each technique separately fail-proofs were implemented.
Further the image reconstruction was modified so that it is possible to calculate maximum intensity projections and or diffusion weighted images directly on the MRI. This was done to simplify the first evaluation of data which is performed at the MRI and to be able to adapt the parameters in case needed.
For a more precise data analysis we utilized Interactive Data Visualization (IDL) by Harris Geospatial to determine the SNR. In phantom experiments, the SNR was calculated as the ratio of mean and standard deviation of the pixel intensities in a homogeneous region. Measurements to estimate the SNR in vivo involved multiple acquisition of which the voxel-wise ratio of the mean value and the standard deviation was averaged over ROIs in the spinal cord to obtain the SNR values.

Chapter 4

Inner Field-of-View Diffusion-Weighted Simultaneous Multi Slice Echo-Planar Imaging

The goal of this study, presented in this chapter, was to accelerate diffusion-weighted imaging in the spinal cord. DWI is a powerful tool for clinical as well as biomedical research. It gives the possibility to detect acute stroke [59], investigate white matter integrity [3] or characterize tissue micro-structures [82]. In the human brain DWI is widely combined with EPI as it provides short acquisition times and reasonable image quality. It was even shown that EPI can be accelerated even further with parallel imaging techniques (PAT) [28, 66, 68] or, as recently shown, with SMS [8, 62, 77].
Imaging of the spinal cord in contrast to the brain bears a few complications. First, near the spinal cord the field inhomogeinities – magnetic susceptibility of tissues – varies due to the lung or bones which increases the distortions present in EPI. Second, a high spatial resolution has to be achieved, due to the small size of the spinal cord and its inner structures which lead to a decrease of the SNR. Third, large FOV's are needed in lower areas of the spine to prevent aliasing effects that increase distortions.
These problems can be approached by shortening the EPI readout echo train, with for example partial Fourier sampling [56, 81], PAT [28, 66], or inner-FOV [7, 16, 64, 87]. Partial Fourier sampling only decreases the echo time and as a result increases the SNR, while the other approaches decrease geometric distortions as well. However, the performance of PAT is often limited in the spinal cord, due to its dependency on the number of receive coil elements and their geometry in respect to the investigated region. Thus, inner-FOV imaging techniques are often used for DWI at the spinal cord.

It was shown successfully that inner-FOV techniques can increase the spatial resolution and prevent aliasing during DWI EPI [16, 18, 39, 71, 86]. To now enhance the performance of inner FOV DWI EPI even further, in this work the combination of it with SMS is going to be investigated. The combination could improve the clinical applicability of spinal cord DTI as it would provide minimal geometric distortions and short acquisition times.

First the combination of all techniques in one sequence is described. Further its performance is probed at phantoms and the conditions which have to be met, are illustrated. Following the performance of the combinations in vivo is investigated. Inner FOV 2DRF and cross-sectional excitations will be compared. Further the performances of simultaneous multi slice imaging is compared to single slice acquisitions combined with the respective inner FOV technique. The results are going to be compared and their pros and cons depending on the conditions are discussed and evaluated.

4.1 Technique Combination and Benchmark Examination

EPI DWI is combined with the following inner-FOV techniques: 2DRF collinear excitations, 2DRF tilted excitations and cross-sectional excitations. The combined sequences with single slice excitations as well as the echo read-out train are sketched in figure 4.1. The sequence is further combined with SMS by exchanging pulses exciting single slices with pulses exciting multiple slices, except for the 2DRF collinear pulses, as here the side excitations can be used. The side excitations or transition zones have to be considered as they could overlap with the additional excited slices or lead to folding artifacts.

The combined inner-FOV multi-band excitations are presented in 4.2. In **(a)** a SMS collinear 2DRF excitation with a multi-band factor of 2 and a side excitation distance of 124 mm is shown. As the distance of the side excitations to the main excitation can be reduced, by using SMS, the duration of the excitation can be decreased as well, depending on the multi-band factor. The side and main excitations can be positioned so they overlap and thus cover the other inner FOV of the SMS acquisition to reduce the side excitation distance.

In case of SMS tilted 2DRF excitations with a multi-band factor of 2, shown in 4.2 **(b)**, the duration compared to single slice 2DRF tilted excitation is increased, as additional trajectory lines have to be considered. However, compared to the collinear approach the excitation duration is shorter and it is constant, as the side excitation distance is constant.

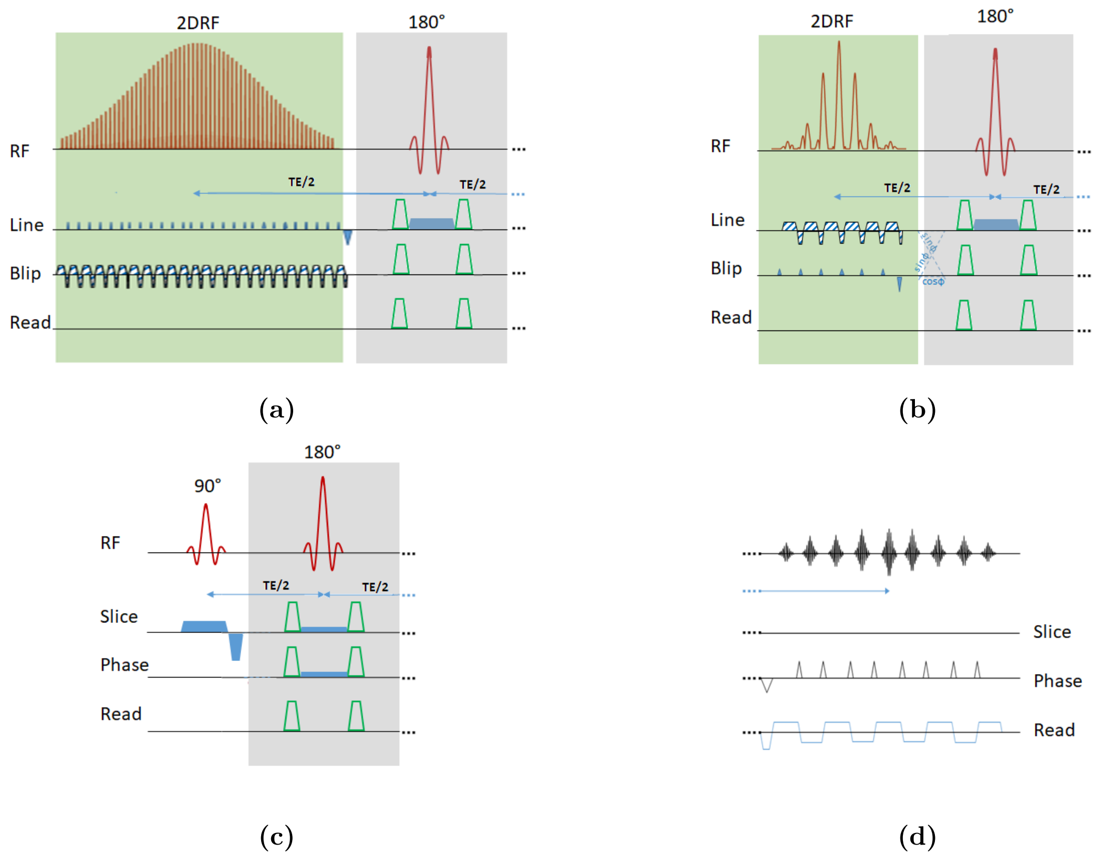

Figure 4.1: Illustrates different inner FOV techniques and an EPI echo read out train. **(a)** sequence sketch of a single slice collinear 2DRF excitation accentuated in green and a Stejskal-Tanner DWI module underlined in gray. **(b)** tilted 2DRF excitation, whith blip and line direction tilted by an angle ϕ respectively, and a DWI part. **(c)** single slice ZOOM-EPI pulse sequence with 180° pulse of DWI module rotated by ϕ to the first excitation. **(d)** shows a standard EPI readout-train with blipped gradients in phase direction. All three excitation and DWI modules were combined with the readout train in the following experiments.

A multi-band pulse with a factor of 2 used during cross sectional inner FOV excitation is shown in 4.2 **(c)**. Its duration is the shortest in comparison with the 2DRF approaches as no side excitations have to be taken into account. However, the transition zones have to be kept in mind for cross-sectional excitations with a rotation $< 90°$. The slices have to be positioned with sufficient distance, to eliminate the possibility of saturating neighboring slices. Further the extra refocused areas which can occur during simultaneous excitation, need to positioned far outside the investigated object to prevent folding artifacts.
The three excitations differ greatly in appearance. The explanation is: The collinear 2DRF multi slice excitation does not differ from a single slice excitation and does not need

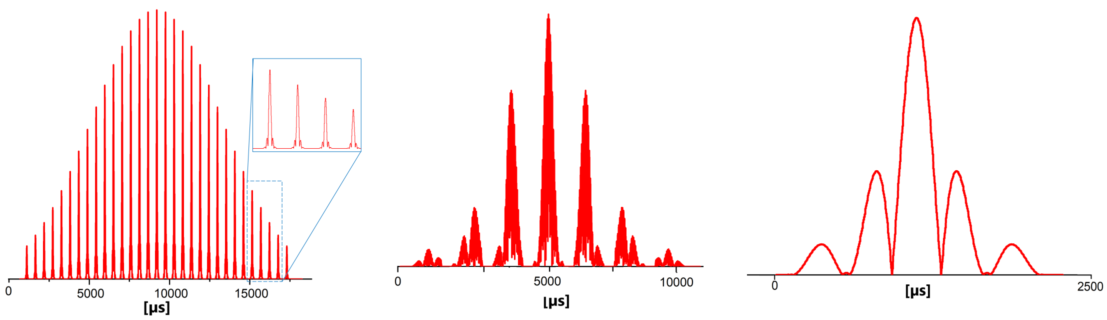

(a) (b) (c)

Figure 4.2: Simulated multi-band pulses used during this work. They were calculated with an acceleration factor of 2 and a distance of the simultaneous excited slices of 124 mm. In **(a)** a SMS 2DRF collinear pulse with a duration of 15000 μs and a small part zoomed in is illustrated. In **(b)** a 2DRF tilted multi-band pulse with a tilt angle of $\phi = 15°$ and a duration of 10500 μs. In **(c)** a cross-sectional multi-band pulse rotated by 15° in respect to the imaging plane with a duration of 2450 μs is presented.

additional phase modulation, the multi slice pulse of the cross sectional excitation is a standard RF excitation phase modulated and in case of the 2DRF tilted excitation the phase modulations of 2DRF and multi slice acceleration have to be combined.

4.1.1 Excitation Profile Investigation

Profile acquisitions of the SMS inner FOV techniques were performed using a twice-refocused spin-echo sequence (one echo per shot) with the same inner FOV and refocusing RF pulses as used in the EPI sequences. The image acquisition and the second refocusing RF pulse (slice thickness 4 mm) were conducted in the excitation plane of the 2DRF pulse, like for the inner FOV EPI acquisitions. The first refocusing RF pulse can be applied either in the 2DRF excitation plane to obtain a profile of the magnetization excited by the 2DRF pulse or in its original orientation to obtain a profile of the refocused magnetization, i.e. the magnetization contributing to the signal during the inner FOV EPI acquisitions. The results of the profile measurement are shown in figure 4.3. The acquisitions were performed with a resolution of 0.5x1.0 mm^2, an FOV of 256x224 mm^2, an acceleration factor of 2, a distance in between the simultaneous excited slices of 40 mm and a fixed echo time of 64 ms. TRs of 6.0 s were used in doped water phantoms, respectively, to avoid saturation effects yielding total acquisition times of 67.6 min per profile.
In **(b)** and **(c)** the side excitations are visible as the excitations are not refocused. For the 2DRF excitation in **(d)** and **(e)** the side excitations are suppressed by the refocusing

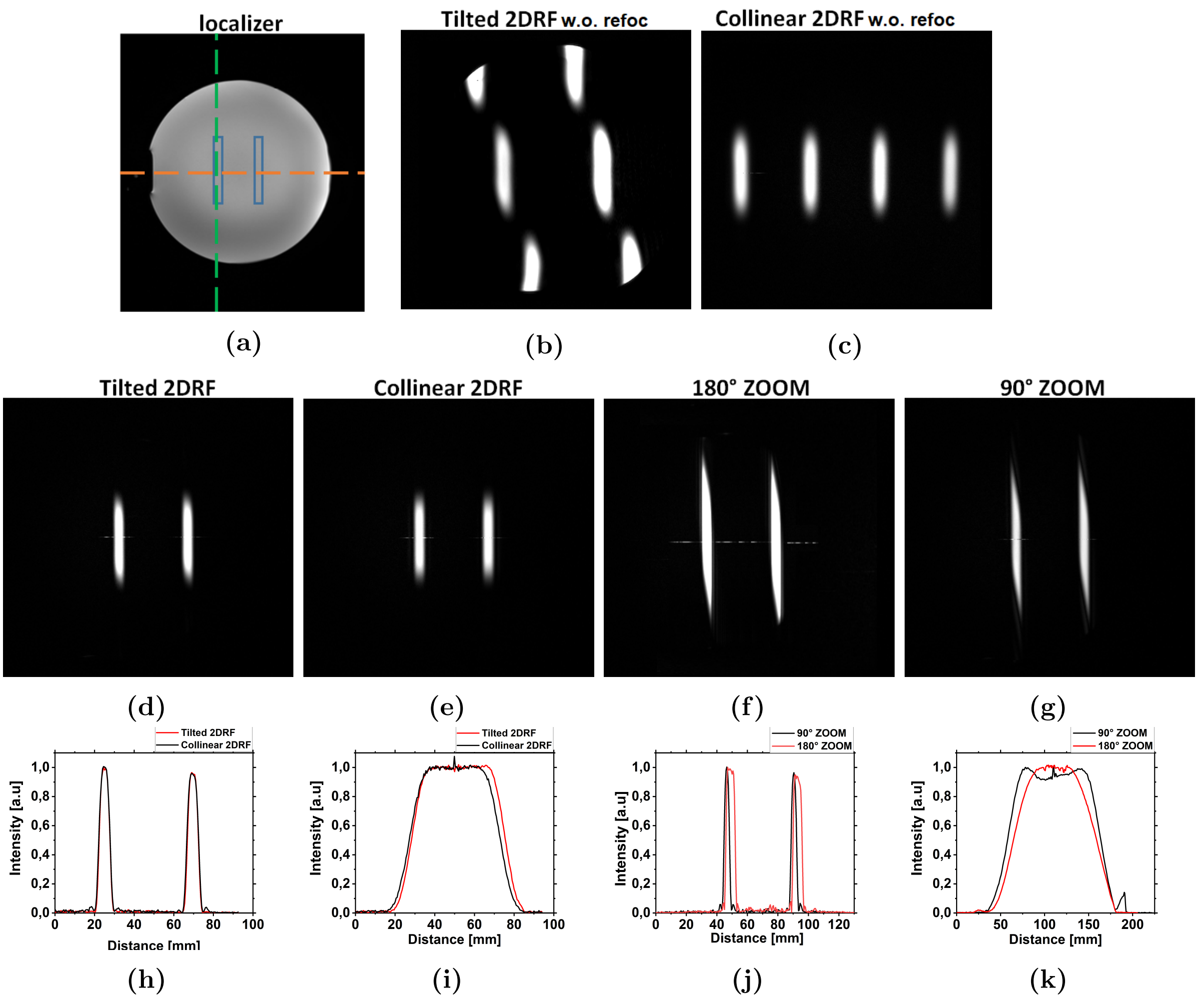

Figure 4.3: **(a)** Localizer of a doped water bottle with targeted profiles of inner FOV profiles highlighted by blue rectangles. Intensity plots of the profiles were acquired along the dashed green (phase direction) and orange (slice direction) lines. **(b)** and **(c)** show non refocused 2DRF profile measurements. **(d)**-**(g)** show profile acquisitions of the spatial magnetization distribution, excited by 2DRF tilted excitation, 2DRF collinear excitation, 180° ZOOM and 90° ZOOM, respectively. The intensity plots in slice direction are presented in **(h)** and **(j)**. Intensity plots in phase direction are shown in **(i)** and **(k)**. **(h)** and **(i)** thereby present the intensity of the 2DRF excitations normalized on the respective highest intensity. **(j)** and **(k)** present intensity plots acquired from the ZOOM acquisition, standardized on the respective maximum ZOOM intensity, respectively.

pulses as desired. Thus, only two excited slices are visible. The profile plots show that the both tilted and collinear 2DRF excitations show a reasonable realization[1] of the slice profiles with full widths at half maximum (FWHM) of about 5.5±0.3 mm in the slice

[1]The peak visible in the collinear acquisition is due to a too short break in between the consecutive performed measurements.

direction and about 60 mm in phase-encoding direction with a plateau (width at 90% of maximum) between 45 and 49 mm and transition zones (between 90% and 10% of maximum) between 20 and 17 mm yielding a usable FOV of 40 and 43 mm. In addition the distance between the simultaneous slices is about 40 mm which is in accordance to the parameters used.
During the ZOOM acquisitions the excitation used for the cross sectional excitation, was rotated by an angle of 15°. Depending on the pulse rotated, the 90° pulse (90° ZOOM) or 180° pulse (180° ZOOM), the thickness of the RF pulse was adjusted to excite the correct inner FOV. In case of 90° ZOOM a thickness scaling of 80% and in case of 180° ZOOM a thickness scaling of 60% was used, to obtain a FOV of 4x40 mm^2.
The 180° ZOOM profile has a FWHM in slice direction of 5.4±0.3 mm and in phase-encoding direction of about 65 mm, a plateau of 46 mm and a transition zone of about 22 mm. In case of 90° ZOOM we measured a FWHM in slice direction of 4.1±0.2 mm, a phase-encoding direction of 73 mm, a plateau of 49 mm and a 28 mm transition profile. This leads to usable FOV's of 43 and 45 mm respectively. The distance in between the slices is about 40 mm, in accordance with the parameters.
The different thickness scaling of the 90° and the 180° rotated RF pulses are performed to adjust the transition zones and the inner FOV as equal scaling factors would vary the width and length of the inner FOV and the transition zones even more, as will be shown in the next section at inner FOV SMS inhomogeneity sensitivity measurements.

4.1.2 Sensitivity to Field Inhomogeinities

In figure 4.4 the sensitivity to field inhomogeinities and frequency offsets of inner FOV EPI is investigated. To be able to evaluate solely the effect on the inner FOV excitations and to avoid an influence of miss adjustments on the SMS reconstruction algorithm, these acquisitions were performed with single band excitations at two slices. For the frequency and gradient offsets adjusted **(a)**, all acquisitions show a good excitation of the inner FOVs with very similar signal intensities. For a system frequency shifted by 100 Hz (Fig. 4.4 **(b)**), the acquisitions with the tilted setup are unaffected. However, for the collinear setup signal losses are observed in both slices for medium and large side excitation distances (about -25 %), while the acquisition with the small FOE appears normal (less than 5% signal loss). The signal losses are due to the low bandwidths of the 2DRF pulses in the blip direction: for a frequency offset, the excitation profile is spatially shifted in the blip direction and not fully covered by the refocusing RF pulses. The corresponding signal

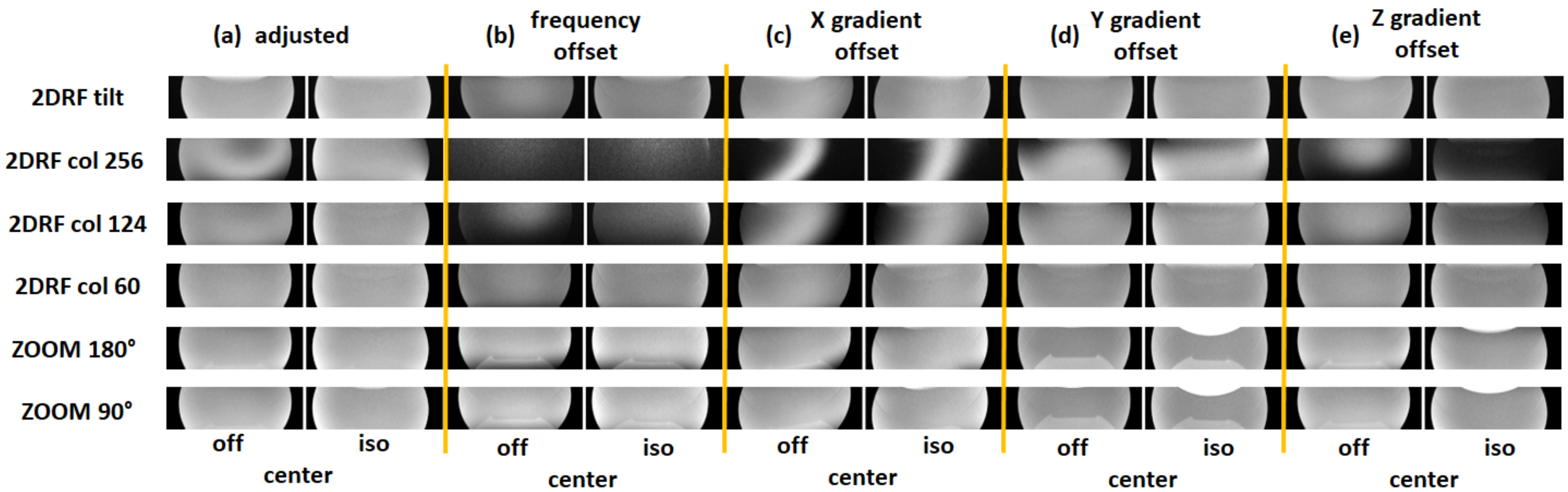

Figure 4.4: Inner field-of-view EPI images of two slices separately acquired with only one slice excited (tilted) or only one slice refocused (collinear), one at an offcenter position of 36 mm (left) , the other at the isocenter (right), obtained with inner FOV excitations using the 2DRF tilted, the 2DRF collinear setup with varying side excitation distances and cross sectional excitations, either tilting the 180 or the 90 degree excitation by 15° or 90°.
For the target protocol (62 slices with 4.0 mm thickness), the side excitation distance of 70 mm for the tilted setup (row 1) is used for acquisitions without and with simultaneous multi-slice (SMS) imaging; for the collinear setup, the side excitation distance correspond to acquisitions without SMS imaging (248 mm, row 2) and with SMS imaging for acceleration factors of 2 (124 mm, row 3) and 4 (60 mm, row 4).
For the cross sectional excitations the cross section is created by a standard 90 degree and a 180 degree pulse tilted by 15° (row 5) or a 90 degree pulse tilted by 15° (row 6) both with a thickness scaling of 70%. Acquisitions were performed with **(a)** the frequency and shim adjusted and (b-e) offsets of the **(b)** frequency (100Hz) and **(c-e)** the gradients (0.05 mT m-1) in z (slice), y (phase-encoding), and x (frequency-encoding) directions, respectively.

loss increases with the effective shift in the slice direction that depends on the relative orientation of the blip direction and the 2DRF bandwidth, i.e. the side excitation distance. For the tilted setup, the side excitation distances is rather small (70 mm) and only a fraction of sin ϕ (15°) of the shift occurs in the slice direction (cf. Fig. 4.4 **(b)**) making it rather insensitive. For the collinear setup, the full shift is in the slice direction, i.e. relevant for the signal loss, and the side excitation distance may be rather large (124 mm / 256 mm for SMS / conventional acquisitions) making it more prone to frequency offsets. This effect is also relevant for field inhomogeneities which are induced by a gradient offset in the slice direction (cf. Fig. 4.4 **(e)**). In this case, the signal loss mostly occurs in the off-center slice (left, about 30% and 15% signal loss, respectively), where the gradient offset induces a frequency offset but not in the isocenter slice (right) for which the mean frequency across the slice remains unchanged.
Also for gradient offsets in phase- and frequency-encoding directions, a significant impact is obvious for the collinear setup with medium and large FOE (Fig. 4.4 **(d,e)**). Both offsets shear the 2DRF trajectory and its excitation profile and thus move parts of it out of the refocusing plane, yielding signal reductions either in frontal or in left and right parts of the excitation profile, respectively. The effects are very similar for both slices as they affect the trajectory, independent of the specific position. Furthermore, the offsets induce typical EPI distortions in all acquisitions, e.g. a slight in-plane shearing for an offset in the frequency-encoding direction.
In the case of the ZOOM acquisitions slight folding artifacts can be observed in the bottom of the images. The frequency offset leads to a shift in slice direction of the cross section, due to the variation of width, shape, bandwidth and duration of the 180° and 90° excitations. The resulting signal loss and or folding artifacts can be observed due to a shift of the cross section. The extend to which the cross section is shifted depends on the rotation between the excitation and refocusing pulses used for the cross sectional acquisition.
In case of gradient offsets in phase and slice direction (Y,Z) folding artifacts can be observed. The Y, Z gradient offsets lead to a frequency offset during the ZOOM acquisitions as the excitation plane is tilted. Further the offsets can alter the thickness of the slices which can lead to additional artifacts.
The acquisitions show that the 2DRF excitations of the collinear setup are more prone to field inhomogeneities for the medium and large FOEs which are required for conventional acquisitions or SMS acquisitions with an acceleration factor of 2 in the current setup. Thus, the applicability to measure large slice stacks in practice could be limited. For smaller FOE, e.g. as sufficient for acquisitions with an accordingly smaller slice stack or

higher SMS acceleration factor, the sensitivity is considerably reduced and comparable to that of the tilted setup. The cross sectional tilted setups are more stable than the collinear approach for middle and large FOE and are nearly comparable to the 2DRF tilted and the 2DRF collinear approach with small FOE. The latter two, however, still show the best overall performance.
The methods combined with EPI will be compared even further in vivo in the following section and in the next chapter the techniques will be even combined with STEAM and FSE and investigated.

4.1.3 Coil Sensitivities

The SMS acquisitions are influenced by the receive coil arrangements, as explained in section 2.5. Depending on the position of the investigated measured volume, the slice stack size and the number of receive coils the SNR efficiency can vary. To investigate the different effects a cylindrical water phantom was measured with single-slice and simultaneous multi-slice EPI and for each slice 16 repetitions were performed. The measurements were performed without inner-FOV to solely evaluate the effects due to SMS. To obtain the SNR values the voxel-wise ratio of the mean value and the standard deviation was averaged over ROIs in the phantom. The SNR relation between SMS and single slice acquisition is presented in figure 4.5. In **(a)** the number of slices was varied and in **(b)** the influence of different measurement positions was investigated at the spinal cord receive coil and combinations of spinal cord receive coil and body receive coil.

The SNR measured with SMS decreases with decreasing numbers of slices measured, in comparison to single slice acquisitions. The SNR difference for 50 slices acquired is in the range of ±5 %, for 30 slices, however, the SNR of SMS is up to 40 % smaller. The reason is that it is easier to disentangle the signal received if the distance between the simultaneous slices is larger. Thus, in vivo only large slice stacks were measured to simplify the signal disentangling of the receive coils.
In **(b)** it can be further observed that the SNR is depending on the position of the measured slice. In the region where two coils overlap, e.g. at ~40 mm in **(b)**, the SNR is decreased in comparison to a slice acquired in the center (100 mm) of a coil. This observation is independent of the calibrated iso-center. The acquisitions with the iso-center adjusted in between two coil sets, shows a similar signal behavior, increased SNR in the center of a coil and decreased SNR between two sets. The explanation is that the signal intensity measured by the receive coils is dependent on the distance between measured slices and

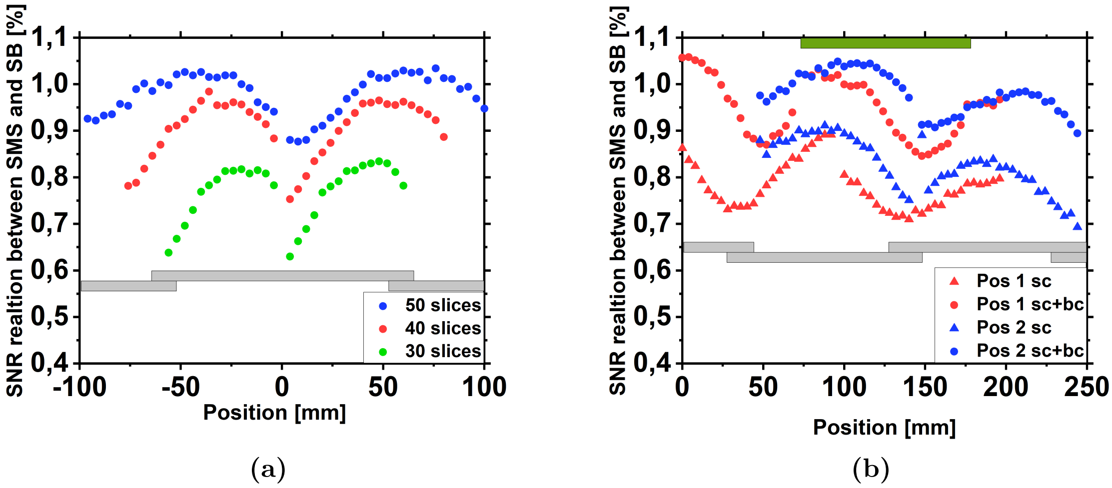

Figure 4.5: Position dependent SMS EPI SNR measurements at a cylindrical water phantom to determine the coil SMS coil efficiency. In **(a)** the performance of SMS EPI in case of varying slice stack sizes is investigated at a 32-channel spinal cord coil. The SNR relation between single slice and SMS is illustrated in blue for 50 acquired slices, in red for 40 and in green for 30. The water phantom was centered around a coil set of 4-channels of 13.5 cm width, illustrated by grey rectangle. The coil sensitivity in dependence of the position of the object during inner FOV SMS acquisitions is shown in **(b)**. The SNR relation was measured with only the spinal cord coil (sc, triangle shaped) and with a combination of spinal coil and body coil (sc+bc, circle shaped). The isocenter and the object were once centered in the middle of a 4 channel batch (red coloured) and once in between two batches (blue coloured) as sketched by the grey rectangles. The center of the body coil, sketched by the green rectangle, was placed above the object centered between the coil batches of the spinal cord.

coils. As the distance in between two sets is nearly equal the signal determined is as well and thus disentangling the signal is more complex than in the center where the distance differs.

The combination of the spinal cord coil with the body coil shows an increase in SNR of ∼10% as the addition simplifies the signal disentangling. To increase the SNR thus the spinal cord coil was either combined with the 64-head neck receive coil or the 18-channel body receive coil, depending on the region investigated, for in vivo measurements.

4.2 In Vivo Measurements

4.2.1 2DRF Inner-FOV SMS Acquisitions

In figure 4.6 non diffusion-weighted in vivo images excited with collinear and tilted 2DRF inner FOV excitations, obtained with single slice and SMS acquisitions are presented. In total 62 slices, that were averaged 16 times, were acquired in the brain stem and the spinal cord of which eight are shown here. The signal was measured with a combination of head-neck and spinal cord receive coil. The acquisitions were performed with an in-plane resolution of 1.0x1.0 mm^2 and a FOV of 40x128 mm^2 plus 16 mm phase-encoding oversampling to account for profile transition zones. An echo spacing of 0.93 ms and a partial Fourier ratio of 6/8 were used yielding a total echo train of 39 ms for all three protocols. The measurements were performed to estimate and compare the SNR in case of single slice and SMS acquisitions combined with 2DRF inner FOV excitations. Thus, the images were acquired once with a fixed TR of 8.2 s that was compatible with all protocols to compare single slice and SMS acquisition, and the shortest possible TR for each individual protocol to evaluate the gain due to an acceleration factor of 2. To obtain the SNR values the voxel-wise ratio of the mean value and the standard deviation was averaged over ROIs in

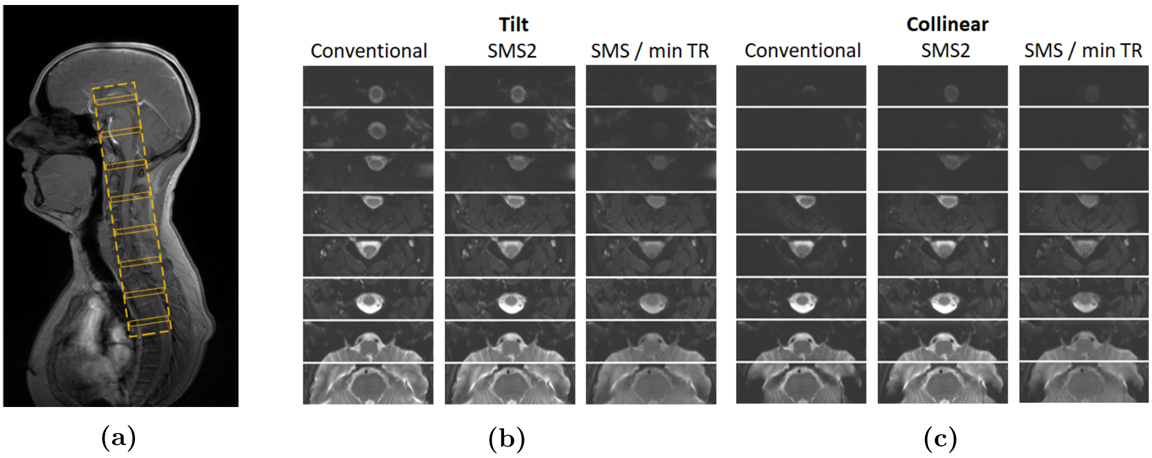

Figure 4.6: **(a)** Localizer and **(b, c)** eight out of 62 slices in the brain stem and spinal cord obtained with EPI without diffusion-weighting (16 averages) using **(b)** 2DRF tilted and **(c)** 2DRF collinear setup without (left columns) and with SMS acquisitions (acceleration factor 2; middle / right columns); SMS acquisitions were performed with the same TR as the conventional acquisitions (middle columns) and with the minimum TR achievable (right columns). All images of a row have identical gray scaling, i.e. the image intensity directly reflects the signal amplitude. The collinear setup suffers from reduced signal intensities in some of the lower slices due to field inhomogeneities.

the spinal cord.
The images acquired with the tilted setup (fig. 4.6 **(b)**) show a reasonable image quality for the whole brain stem and spinal cord covered, they are similar for both single slice and SMS acquisitions. No negative effects due to the SMS acceleration or the prolonged 2DRF excitation can be observed. For the SMS acceleration with conventional TR (8.2 s) the SNR in the spinal cord is almost identical (−0.2 %) to the single slice acquisition. For the SMS acquisition with minimum TR (3.4 s), a change in contrast and reduction of the SNR of approximately 10 % can be observed. The reason therefor is the shorter TR, however, as the acquisition time is almost halved, the SNR efficiency is considerably higher, by 23 %, in comparison.
The collinear setup 4.6 **(c)** in comparison to the tilted setup shows a SNR loss in average of −32 % in case of the single slice acquisition. This signal loss is rather pronounced (up to −75 %) in the lower spinal cord area. One reason therefore is the longer TE (+14 ms) due to the longer excitation pulse. The other reason and major one is the increased sensitivity to field inhomogeinities, as observed in the previous section and in figure 4.4. The SMS acceleration of the collinear setup by a factor of 2 reduces the TE and sensitivity which increases the SNR by approximately 40 % in comparison to single slice collinear acquisition for long and short TR. This as well, is in accordance with the phantom measurements done before, as we halve the side excitation distance. However, in comparison to the tilted setup the SNR and the SNR efficiency still suffer. In the lower cord sections the SNR is reduced by up to 60%. This means for our settings with 2DRF excitations, the tilted setup currently provides a better SNR performance.

In figure 4.7 results of a DWI measurement obtained with 2DRF inner FOV excitations and SMS acceleration for both setups are shown. In **(b)** and **(c)** sagittal reconstructions are presented: First, an isotropic diffusion-weighted image (DW_{iso}), second, an apparent diffusion coefficient (ADC) or ADC map, third, a fractional anisotropy (FA) image.
The diffusion-weighting was performed with a Stejskal-Tanner gradient pulse pair (see 2.3) with a duration δ of 9 ms and diffusion times Δ of 24 ms. The diffusion tensor image (DTI) was acquired with a b value of $625\,\mathrm{s\,mm^{-2}}$ and six non-collinear directions of the diffusion weighting and an image with no diffusion weighting. The echo times for the collinear setup were 76 ms and for the tilted 64 ms. The repetition times were 3.5 s for the collinear setup and 3.4 s for the tilted setup. This results, with two preparation scans to achieve a steady state, reference scans for SMS acquisitions, and 16 averages, in a total measurement time of 6.6 min for the tilted and 6.8 min for the collinear setup.
The images show similar results to the SNR measurements, for both setups – tilted and

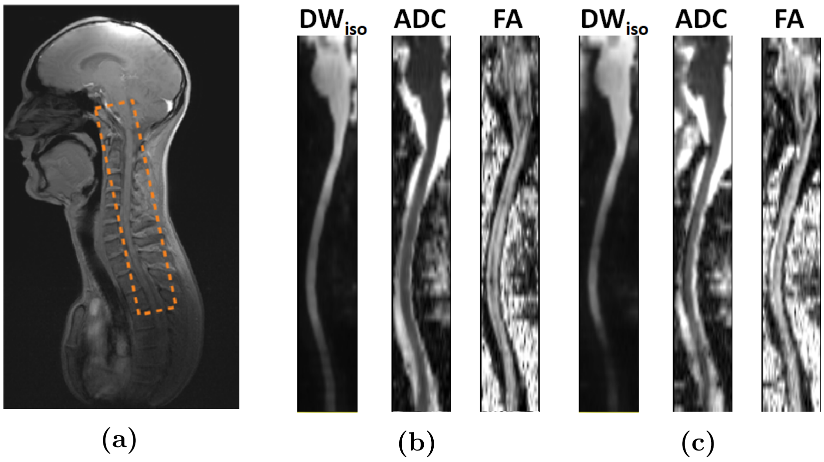

Figure 4.7: **(a)** Localizer and **(b)**,**(c)** results of 2DRF inner FOV DWI EPI acquistions with a two-fold SMS acceration using the **(b)** tilted and the **(c)** collinear setup: sagittal reconstructions of isotropic diffusion-weighted images (DW_{iso}), maps of the apparent diffusion coefficient (ADC) and the fractional anisotropy (FA) (from left to right)

collinear – very similar image quality can be obtained. In the lower cord regions both setups suffer as the read out channels found in the lower region have a worse sensitivity compared to the ones in the head-neck area and less coils are found, due to the assembly of spinal cord and head neck receive coils. Further it is a consequence from the increased sensitivity to field inhomogeinities (see Sec. 4.1.2). The signal reduction is slightly more pronounced in case of the collinear setup in comparison to the tilted setup which can be recognized in the isotropic diffusion-weighted images due to its higher sensitivity to field inhomogeneities. This is also reflected in the ADC[2] and FA[3] images and values which were obtained. Both, values and image quality are significantly reduced for the collinear setup due to noise floor effects [40].

4.2.2 ZOOM Inner-FOV SMS Acquistion

In figure 4.8 8 out of 62 diffusion-weighted images averaged 16 times and obtained with single slice and SMS acquisition are presented. However, in comparison to figure 4.6, ZOOM was used, with the 180° **(b)** and the 90° **(c)** pulses rotated by 15° and a thickness scaling of 60% and 80% respectively. The resolution, the receive coils used, as well as the echo time TE (30 ms), the repetition time TR (8.2/3.4 s) and the other parameters were

[2]ADC values: (tilt: conv. 0.99 SMS2: 0.98 / collinear: conv. 0.64 SMS2 0.78) x$10^{-3}mm^2s^{-1}$)
[3]FA values: tilt: conv. 0.59 SMS2 0.58 / collinear: conv 0.44 SMS2 0.51

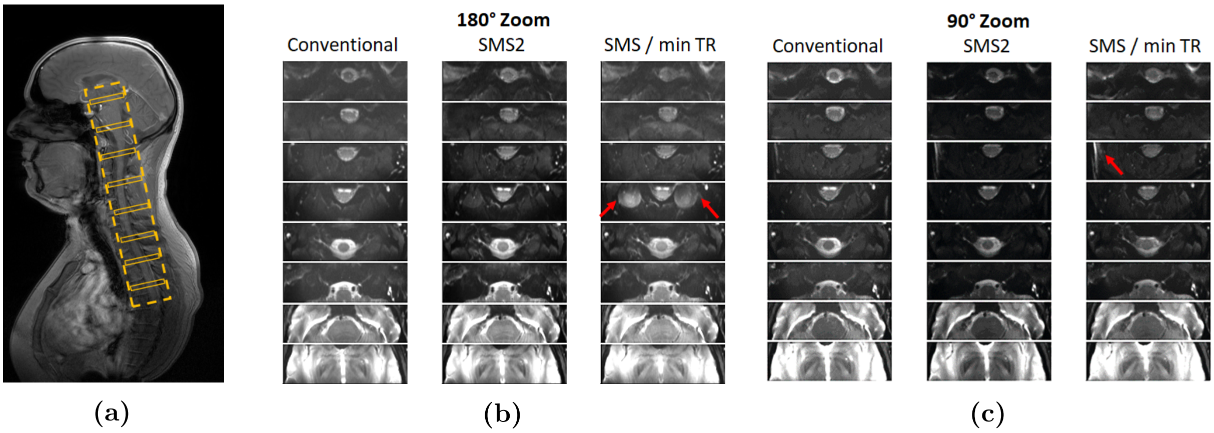

Figure 4.8: **(a)** Localizer and **(b, c)** eight of 62 slices in the brain stem and spinal cord obtained with EPI without diffusion-weighting (16 averages) using ZOOM with **(b)** 180° pulse and **(c)** 90° pulse tilted without (left columns) and with SMS acquisitions (acceleration factor 2; middle / right columns); SMS acquisitions were performed with the same TR as the conventional acquisitions (middle columns) and with the minimum TR achievable (right columns). All images of a row have identical gray scaling, i.e. the relative image intensity directly reflects the relative signal amplitude. Red arrows highlight artifacts.

equal to the 2DRF excitation acquisitions.

All six slice stacks measured have a good image quality. However, the single slice acquisitions differ slightly from the SMS acquisitions. In case of the images acquired with the 180° pulse rotated, artifacts are easily visible in case of SMS with short TR (4th slice, red arrows). For the 90° SMS acquisitions artifacts are visible as well (3rd slice, red arrows), even though they aren't as pronounced. The artifacts between the two different approaches seem to differ, however, they might have the same origin. One possible explanation that the artifacts occur, could be an overlap of the refocusing pulse of the 1st slice and the excitation pulse of the 2nd simultaneous acquired slice or vice versa which leads to an refocused imaging region in the image plane outside the measured FOV. Depending on where this additional excitation is located, within the body or outside, additional tissue could be excited and folding artifacts occur. However, as the distance between the simultaneous excited slices is rather big this is rather unlikely to happen. Another possible explanation that the artifacts occurred, could be that the transition zone is bigger than the phase oversampling and or saturate the following measured slices. The transition zone was ~14 mm wide and of ~3.3 cm high. As the phase oversampling used for the measurements was 16 mm and a gap of 4 mm was ensured between two consecutive measured slices by measuring the stack in an incremental manner, this is no possible explanation in this case.

The difference in between the observed artifacts during 90° and 180° ZOOM can probably be explained by the difference in bandwidth and pulse width of the respective rotated excitations. It leads to a variation of the cross section, the transition zone, as well as the additional excitation.
In addition to the occurring artifacts during the SMS acceleration a slight signal decrease in the lower cord areas can be observed. The reason therefor is that due to the assembly of the spinal cord and head neck receive coils less read out channels are found in the lower region, as already experienced during the measurements with 2DRF excitations. The SNR which was determined from the images, in the spinal cord confirms these observations. In case of the 180° ZOOM acquisitions the SNR decreases in between single slice and SMS acquisition which is more pronounced in the lower regions. The simple application of SMS with no acceleration of TR leads to a decrease of $\sim 5\%$ in brain stem and upper cord and $\sim 23\%$ in the lower regions, due to the increased inhomogeinity sensitivity and reduced number of receive channels. In case of SMS with acceleration of TR the SNR is $\sim 20\%$ and $\sim$ 34% less in the upper and the lower areas compared to single slice acquisitions. Still, the SNR efficiency increases due to the acquisition acceleration by approximately 24% similar to 2DRF excitations. The SNR difference of the 90° images is slightly higher compared to the 180° acquisitions. Between single slice and SMS acquisitions with long TR in the upper regions a SNR decrease of $\sim$ 10% and in the lower of $\sim$ 25% was determined and for the accelerated acquisitions a decrease of 25% and 35%, respectively. The general decrease of signal while applying SMS is caused by the increased inhomogeneity sensitivity. The acceleration of the measurements by decreasing TR leads to an additional decrease of the SNR, but again increases the efficiency of SMS ZOOM EPI by $\sim$ 24%. The difference between 180° and 90° acquisitions of $\sim 8\%$ lies probably in the slightly varying excitation profile of the cross section and the different bandwidths of the rotated excitations, as shown in the profile and sensitivity measurements.

In figure 4.9 ZOOM DTI SMS EPI measurements with 90° and 180° pulses rotated by 15° with a thickness factor of 60% and 80% respectively, of a volunteer are presented. The image acquisition was accelerated by a factor of two and the shortest possible TR (3400 ms) was used. The diffusion weighting was performed with a Stejskal-Tanner gradient pulse pair, with a duration δ of 9 ms and diffusion times Δ 24 ms. The image was acquired with a b value of $625\,\mathrm{s\,mm^{-2}}$, six non-collinear direction and a non weighted image. The echo time TE was 63 ms for both setups. The total measurement time summed up to 6.5 min, due to 16 repetitions, 2 preparation scans and SMS reference scans.
The images present similar results to the SNR measurements. The image quality of

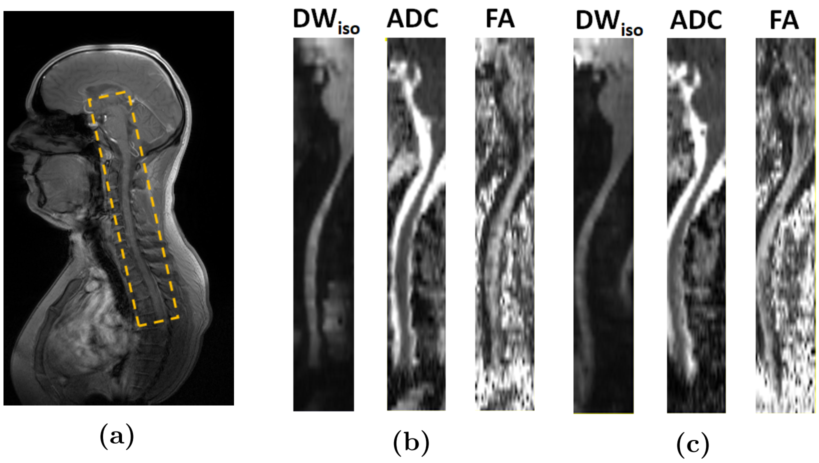

Figure 4.9: (a) Localizer of volunteer with measured slice stack highlighted in orange. **(b)** 180° ZOOM and **(b)** 90° ZOOM EPI acquisitions with (l.t.r) sagittal reconstructions of isotropic diffusion-weighted images (DW$_{\mathrm{iso}}$), maps of the apparent diffusion coefficient (ADC) and the fractional anisotropy (FA)

both setups is very similar. In the lower cord region both setups show signal drop outs due to the inhomogeinity sensitivity and the reduced number of receive channels, as mentioned before. As the tissue susceptibilities in the lower spinal cord area measured differ stronger in comparison to the neck or brain stem region. Further, in case of the ZOOM 90° slightly less signal is obtained compared to the 180° which is mostly visible in the isotropic diffusion-weighted images. The reason there for is that the bandwidth and width of the rotated excitations differ slightly and thus are affected differently by magnetic inhomogeinities. Thus, the ZOOM method with the 180° pulse rotated has a slight edge compared to the 90° rotated pulse.

4.2.3 Comparison of 2DRF tilted and ZOOM 180°

Of the inner FOV techniques which thus far have shown the best image quality in combination with SMS – 2DRF tilted and ZOOM 180° –, a comparison is shown in figure 4.10 in form of transversal color-coded FA acquisitions. The images were acquired with the same parameters as the previously acquired images. The methods show nearly no difference in performance in combination with SMS. The SNR efficiency is increased significantly compared to single slice acquisition, as shown before. However, the images acquired differ depending on the inner FOV technique. The images measured with ZOOM show a lot of noise in the lowest areas of the spinal cord and the brain stem which can not be observed in the 2DRF tilted acquisitions and due to which the anisotropic diffusion is

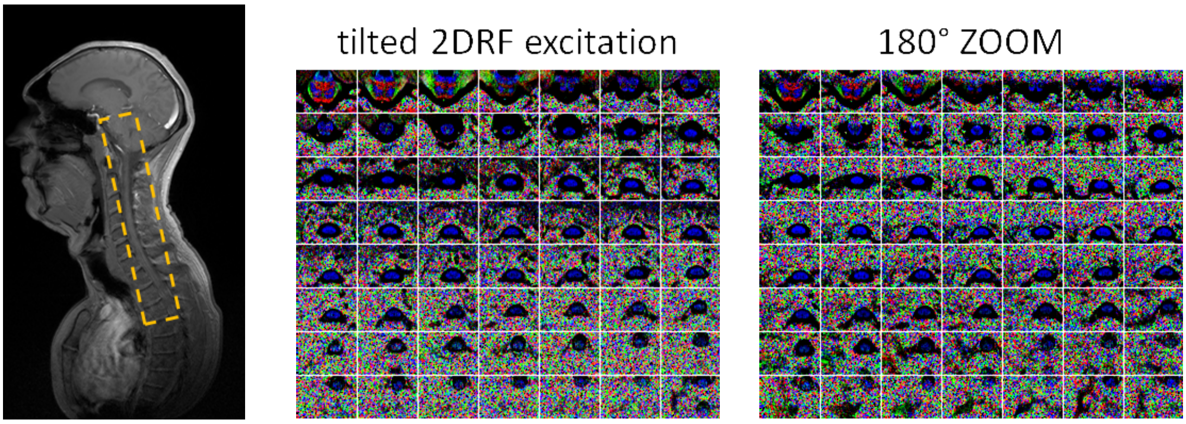

(a) (b) (c)

Figure 4.10: (a) Localizer, 56 out of 62 transversal color-coded FA results of inner FOV DWI EPI acquistions with a two-fold SMS acceleration using the **(b)** tilted 2DRF excitation and the **(c)** 180° ZOOM setup, red arrows highlight areas with noise effects

not recognizable. A reason therefor could be that the bandwidth varies slightly during ZOOM and thus the sensitivity to inhomogeinities varies as well which does not occur for the 2DRF tilted excitations.

4.3 Discussion

In this study, four basic setups for inner-FOV DWI based on 2DRF excitations [19, 75] and cross sectional excitations [87] have been combined with SMS acquisition [8, 77]. The performance has been evaluated and compared, and the feasibility to shorten acquisition times has been demonstrated in vivo at healthy volunteers.
For the settings used in this study, large slice stack with low SMS acceleration factor, the tilted setup showed the best SNR performance. The reason therefor is the low sensitivity to field inhomogeneities which is related to its short 2DRF pulse duration[4] and the orientation of the blip direction with the lowest bandwidth. Further it is not as sensitive to magnetic inhomogeinities like cross-sectional excitations.
For the tilted setup, each inner FOV of an SMS acquisition must be considered in a defined excitation profile, however, the 2DRF trajectory can be used either for single or SMS acquisitions. The fixated side excitation distance can be used, independent of the height of the slice stack to be measured or the band distance between simultaneous excited slices which makes it rather flexible. A reduced gradient amplitude nevertheless could be

[4] 9.9 ms tilted compared to 16.6 ms collinear setup

required for higher SMS acceleration factors, to avoid excessive 2DRF peak amplitudes, as each additional excited slice adds its own profile. This would prolong the 2DRF excitation and as a result the sensitivity to field inhomogeinities would increase as observed similarly at 2DRF collinear excitations.

In case of the collinear setup, the side excitations can be positioned to cover the other bands of an SMS acquisition, to reduce the side excitation distance compared to conventional acquisition with the same stack size. Thus, the collinear setup benefits from SMS imaging in terms of shorter 2DRF pulse duration. There can be a combination of parameters (measured number of slices, slice thickness, acceleration factor) where the side excitation distance of the collinear setup is smaller than the ones of the tilted setup[5] and thus the tilted setup could get outperformed. For each variation of the side excitations, multi-band factor or slice stack size, new 2DRF trajectories and envelopes have to be considered depending on the slice stack and the band distance of an SMS acquisition which complicates the collinear approach again. Further it has to be evaluated whether larger acceleration factors and the small distance between two simultaneously excited slices are feasible with the coils available. In our case in the region of the spinal cord this is not possible due to the receive coil assembly.

The collinear setup could be of advantage for improving the resolution of the 2DRF trajectory easily in line direction as it could reduce the phase-encoding sampling and thus, reduce the EPI echo train. However, for the current setup, this would require a prolongation of the 2DRF excitation which would exceed the time saved for the echo train resulting in an overall longer TE and additional the sensitivity to field inhomogeinities would also be raised.

The signal losses observed with the collinear setup are caused by displacements of main and or side excitations due to field inhomogeinities which reduce the overlap with the refocusing RF pulse. This could be avoided by adjusting the bandwidth of the refocusing excitation to the one of the 2DRF excitation in slice direction, however, this would lead to a excessively long refocusing pulse and is rather complicated. Further, additional problems which are connected to the low bandwidth are not solved, as e.g. false slice position or thickness. A better approach could be to consider the actual field distribution and adapt the profile and side excitations individually to compensate the individual displacements. This on the other hand could lead to unwanted side excitations which could be shifted into the slice stack and saturate slices. Further this approach would only be feasible for

[5] In this work this would correspond to a combination of parameters which would allow a side excitation distance smaller than 70 mm

acceleration factors of two, if the shift in between the side excitations vary, as the side excitations are needed to cover the additional inner FOV during SMS. In case of the tilted setup displacements, due to field inhomogeinities, mostly occur in the image plane and thus it is less prone to them. Additionally as each slice acquired simultaneously has its own excitation profile, the shifts could be corrected individually in contrast to the collinear approach. A strong in-plane field inhomogeneity could lead to a curvature of the slice and thus the overlap with the refocusing pulse may vary within the image. However, in case of a small inner target region like the spinal cord this should not be an issue.
For the ZOOM acquisitions the transition zones for each inner FOV have to be considered, they need a sufficient distance in between the excited bands and the transition zones should not overlap with a following excitation, to prevent saturation effects. The transition zones vary slightly in size in phase-encoding direction, depending on the rotated pulse, 90°/180°. This can lead to the need of larger oversampling to prevent folding artifacts. It can, however, be solved easily by adjusting the pulse thickness and or the rotation angle of the rotated excitation, as done in this work. Generally for ZOOM the same excitation profile can be used for single slice and SMS acquisitions, but it can be of advantage to adapt the rotation angle, the pulse thickness, and or the phase oversampling size depending on the region investigated, to reduce possible artifacts. Artifacts can occur if regions outside of the inner FOV are excited which can lead to folding artifacts. Further artifacts can occur as the pulses used to excite the inner FOV can be affected by field inhomogeinities and thus shift the excitation and refocusing pulse and as result the overlap in the images varies. Additionally the variation of the susceptibility depending on the measured region surrounding the inner FOV can affect the simultaneously applied pulses differently and thus the overlap for each simultaneous acquired inner FOV can be shifted.
One possible approach to suppress the artifacts could be to use saturation bands to pre saturate regions outside of the inner FOV. This would, however, increase the measurement time slightly. A different approach to suppress artifacts would be to change the rotation angle of the tilted excitation, e.g. from 15° as used in this work to 165°. This would rotate the additional cross section as well and thus tissue structures that could contribute signal are not excited. The side excitations, however, still occur in the image plane and signal from a different region can affect the image.
The signal losses observed in the lower regions of the spinal cord in the measurements are due to the reduced number and the increased size of the receive channels and the displacement of the cross section, because of magnetic inhomogeinities. If either of the pulses used for the inner FOV excitation are displaced, a signal loss either in slice or image

plane can occur. A possible solution could be to consider the actual field distribution and adapt the profile individually, as similarly proposed for the 2DRF excitations.
For all four inner FOV approaches it has to be evaluated to which degree higher acceleration factors are feasible for spinal cord imaging. As the coil sensitivity measurement have shown that for a multi-band factor of 2 the SNR decreases significantly below 40 measured slices compared to single slice acquisitions ($\sim 30\%$). An increased acceleration factor would decrease the SNR as the signal separation would be more complex and even though the measurement time is even shorter the SNR efficiency does not increase, it rather even decreases.
The biggest difference in performance between the two inner FOV approaches is that in case of 2DRF excitations only the region of interest has to be considered for the measurements. Inhomogeinities which are outside the region of interest seem to not influence the 2DRF excitations as strongly as the cross sectional pulses. This makes the tilted 2DRF approach slightly more robust than the 180° ZOOM setup. However, the adaptation in case of stronger magnetic inhomogeneities is simpler in case of ZOOM.

In conclusion, in this chapter, four basic setups for inner-FOV DWI have been combined with SMS acquisition and their feasibility to shorten acquisition times has been demonstrated in vivo in healthy volunteer. The evaluation and comparison show that ZOOM 180° and 2DRF tilted are the easiest to handle and show the best performance. Further in combination with SMS the acquisition times of diffusion-weighted imaging can be shortened significantly. Thus, it could help to improve the performance of spinal cord DWI and facilitate clinical applications, e.g. in spinal cord injury.
In the next chapter the performance of these methods will be investigated near strong magnetic inhomogeinities, due to e.g. metallic implants, to investigate the range in which DWI measurements with inner FOV EPI are feasible.

Chapter 5

Diffusion-Weighted RF Refocused Spinal Cord Imaging Near Metallic Objects

A large amount of people require metallic implants due to e.g. arthroplasty of knee, hip replacement, spinal fusion, etc. [85] and the number is expected to increase in the next decades [74]. MRI could pose a great tool for unwanted complications after a surgery and or to control the fiber integrity with diffusion weighted imaging after an operation. However, metallic implants render MRI nearly incapable, as the diagnostic utility is limited rather strongly. Although many metallic implants are MRI safe, they still influence the imaging process. Metals influence the surrounding static magnetic fields due to susceptibility variations in between metals and tissue structures [35]. The variations thereby depend on shape, metal, size and orientation (see 2.6). At implants near the spinal cord it is especially difficult to acquire images due to the size of the spinal cord and different tissue structures surrounding it. To improve DWI near metallic objects at the spinal cord, different methods were investigated in this chapter.

In the previous chapter the performance of DWI at the spinal cord without metallic objects was improved. However, the methods suffer greatly near metallic implants, as will be shown in the first part of this chapter. The reason therefor lies within the sequence. The echoes are read out with blipped phase encoding gradients during EPI and are not individually refocused with RF pulses after each echo time. Thus, the k-space trajectory is distorted which leads to strong distortions and or cancellations in the image (sec.: 2.6). To address the problems of reduced image quality we investigated the performance of RF refocused sequences, like STEAM or FSE, in combination with inner FOV techniques near

metallic artifacts. The first attempts, as well as their results are going to be explained and evaluated in the second section.
Following, to further improve the signal near metallic implants additional methods, e.g. MAVRIC and VAT, were applied and investigated at phantoms. As in previous studies they have shown to be of great use in the vicinity of metallic objects [9, 45]. They reduce the cancellations and distortions which can be observed in the images. After the evaluation of their effectiveness we combined all techniques and applied them in vivo. The results are presented and discussed in the third section. In the last part EPI, STEAM and FSE in combination with all methods (MAVRIC, VAT, inner FOV) are compared and discussed. Further a conclusion and an outlook are given.

5.1 Echo-Planar Imaging Near Metallic Objects

Diffusion weighted measurements at volunteers with implants were performed with tilted 2DRF inner FOV echo-planar imaging, similar to the measurements performed in the previous chapter, to demonstrate the extent of the distortions caused by metallic artifacts. Two volunteers were measured, the first is shown in figure 5.1 and the second in figure 5.2. We measured 16 slices with a resolution of 1x1x5 mm^3, averaged 16 times and used a FOV of 30x128 mm^2 with 16 mm phase oversampling. The DWI was performed with a b value of 500 $\mathrm{s\,mm}^{-2}$ and six weighted directions and one non weighted. The echo time TE was 56 ms and the repetition time TR 3000 ms. This resulted in a total measurement time of 4.32 min First a volunteer with a metallic cage implanted in the larynx area, is measured with an 2DRF inner FOV EPI (shown in Figure 5.1). In the FLASH-localizer **(a)** the spinal cord can be depicted quite well and in front of it a black area can be spotted which is highlighted by magenta dots. This area corresponds to a metallic cage which was implanted, similar to the ones shown in figure 3.3 (**b**). In the sagittal reconstruction acquired with DWI ($\mathrm{DW_{iso}}$, ADC, FA), the spinal cord can be recognized well. However, slight distortions artifacts are visible in the images. A strong curvature of the spinal cord can be observed. In the transversal color-coded FA acquisitions in several slices (e.g. 5, 8, 16) further distortions can be observed in the central region. The spinal cord in the images is rather slim and "triangle" shaped. This can origin from the surgery of the patient or field inhomogeinities influencing the imaging process. The latter seems to be more likely as the localizer shows a rather normal form, and even though we confirmed in the previous chapter the stability of 2DRF DWI EPI, a metallic implant leads to a much stronger distortion, compared to distortions present in healthy tissue structures.

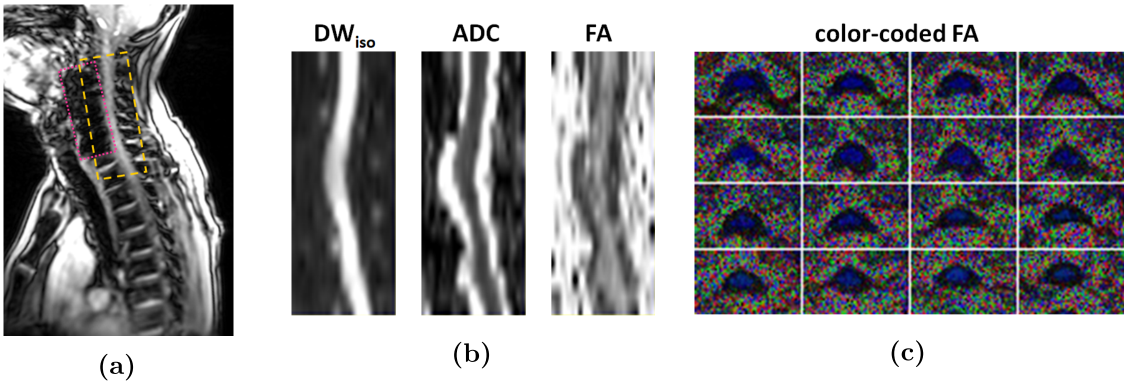

Figure 5.1: (a) Localizer of volunteer with a metallic cage highlighted in magenta and measured stack marked orange. **(b)** Sagittal reconstructions of isotropic diffusion-weighted images (DW$_{iso}$), maps of the apparent diffusion coefficient (ADC) and the fractional anisotropy (FA) and **(c)** transverse slices of color-coded FA (upper left slice corresponds to the upper measured region) acquired with 2DRF inner FOV EPI.

This is also demonstrated at an additional volunteer in figure 5.2, who has an implant, containing six metallic screws connected with 4 metallic bars, near the thoracic spinal cord.
In the FLASH acquisition 5.2 **(a)** it can be observed that the implant has a much stronger impact compared to the metallic cage. In a large area no signal is obtained. The signal is screened out by the metallic artifacts or distorted in such a manner that the signal appears in a different area.
In **(b)** the sagittal DTI EPI measurement show a similar phenomenon. Only in the lower

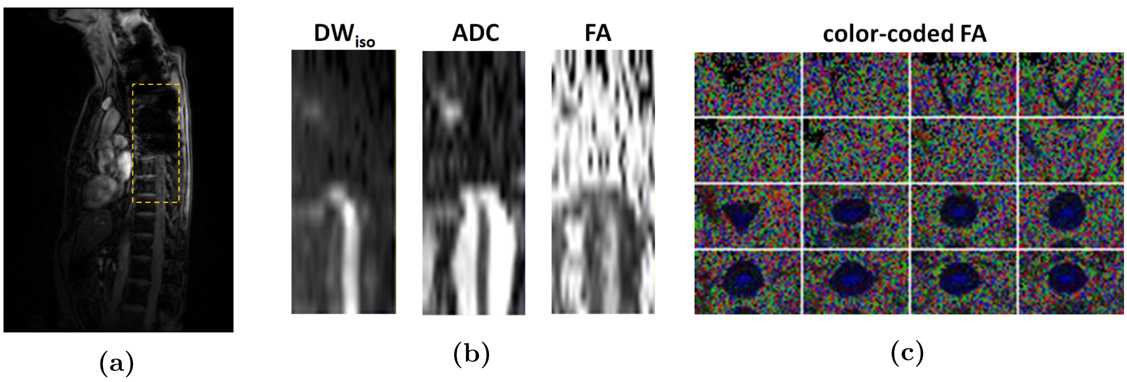

Figure 5.2: (a) Localizer of volunteer with metallic screws and bars implanted (measured stack marked orange). **(b)** Sagittal reconstructions of isotropic diffusion-weighted images (DW$_{iso}$), maps of the apparent diffusion coefficient (ADC) and the fractional anisotropy (FA) and**(c)** and transverse slices of color-coded FA acquired with 2DRF inner FOV EPI

area the spinal cord can be pictured, in the upper part the metal leads to distortions and cancellations of the signal. In the transversal color-coded FA **(c)** this observation is repeated. Further in the middle slices the spinal cord seems to be deformed into a "triangle" shape. In the upper region some areas with small signal can be observed, however, it can not be told where the signal originates from, thus it should be handled with care.
From the measurements it can be observed that performance of EPI near metallic implants depends on position, size and nature of the implant. If the distortions induced by the implant are small EPI still presents a reasonable signal. However, near strong distortions of the static magnetic fields due to metallic objects it can be observed that EPI is rendered unusable, even with inner FOV techniques.
Thus, in this work we took a new approach to acquire diffusion weighted images near metallic implants at the spinal cord and utilized RF refocused sequences, namely FSE and STEAM.

5.2 RF Refocused Sequences

To measure DWI with RF refocused sequences, we combined STEAM and FSE with a diffusion pulse module. Further, we added inner FOV techniques –2DRF excitations, cross sectional excitation–, as they have shown to be of benefit for imaging near the spinal cord.

5.2.1 Single-Shot STEAM

The complete single-shot STEAM sequence combined with DWI and inner FOV is sketched in figure 5.3. The diffusion weighted single-shot STEAM sequence excites a region of interest and stores the magnetization after the applied diffusion module and second 90° pulse, which is then measured with repeated low amplitude RF alpha pulses, as explained in 2.2.3. The first pulse is in this case a 2DRF excitation with the blip and line trajectory rotated by an angle ϕ, respectively (green shaded). In between the first and second 90 degree pulse a diffusion module is integrated (grey shaded). The sequence further grants the possibility to use cross-sectional excitations instead of 2DRF excitations. Therefor the possibility to rotate any RF pulse (1st/2nd 90°, 180°, α) by an angle ϕ is implemented, as similarly done at DWI EPI.
The sequence was first tested with standard phantoms without metallic artifacts and after they showed viable results STEAM was tested in vivo at healthy volunteers.

For the measurements half Fourier sampling was used, to enable larger alpha pulses

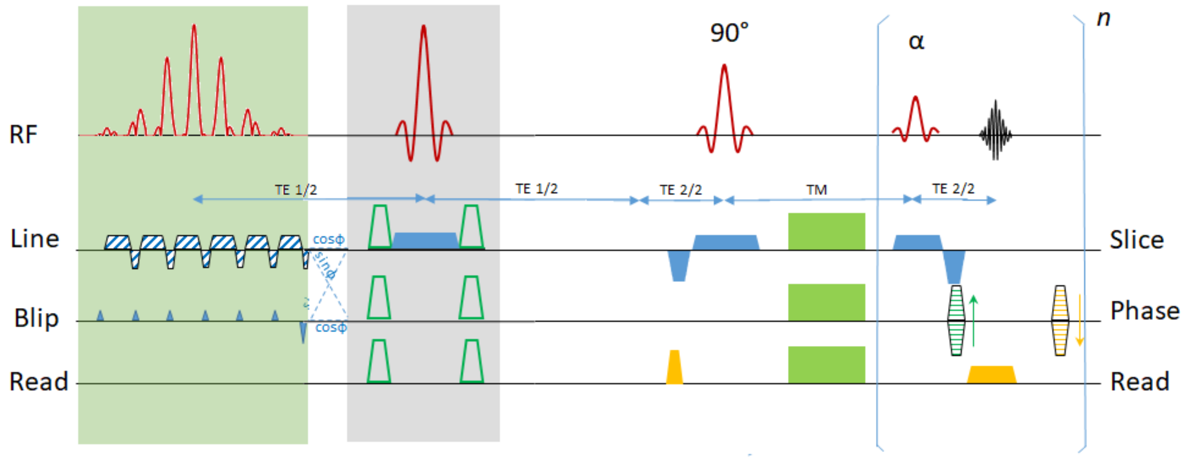

Figure 5.3: schematic sketch of a STEAM sequence combined with a tilted 2DRF excitation pulse (green shaded) and a Stejskal-Tanner diffusion module (grey shaded).

and to increase the SNR [21]. This effect is further heightened in combination with inner FOV techniques, as the number of k-space lines to be measured is reduced, as shown in figure 5.4. Besides the increased flip angle the acquisition time decreases as well. For the image acquired with Full Fourier sampling in centric reordered fashion **(a)** an acquisition time of 1183 ms and a flip angle of 12° were used. For the Half-Fourier acquistion the flip angle was increased by 6° to 18° and the measurement duration was nearly halved to 652 ms. This led to a relative SNR increase of 120% in comparison. The addition of inner FOV techniques enabled the usage of a flip angle of 22° and for a 2DRF tilted acquisition, as presented in **(c)**, the acquisition time can be reduced to 264 ms. As result the SNR is slightly reduced in comparison to the full FOV HF acquisition, however, the relative

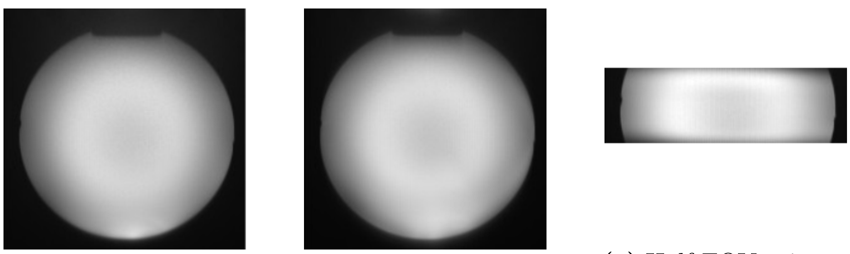

(a) Full-Fourier **(b)** Half-Fourier **(c)** Half-FOV + inner FOV

Figure 5.4: Single-shot STEAM images of a water phantom covering a full FOV with centric full- Fourier sampling **(a)**, a full FOV with half-Fourier sampling **(b)** and an inner-FOV with half-Fourier sampling **(c)**.

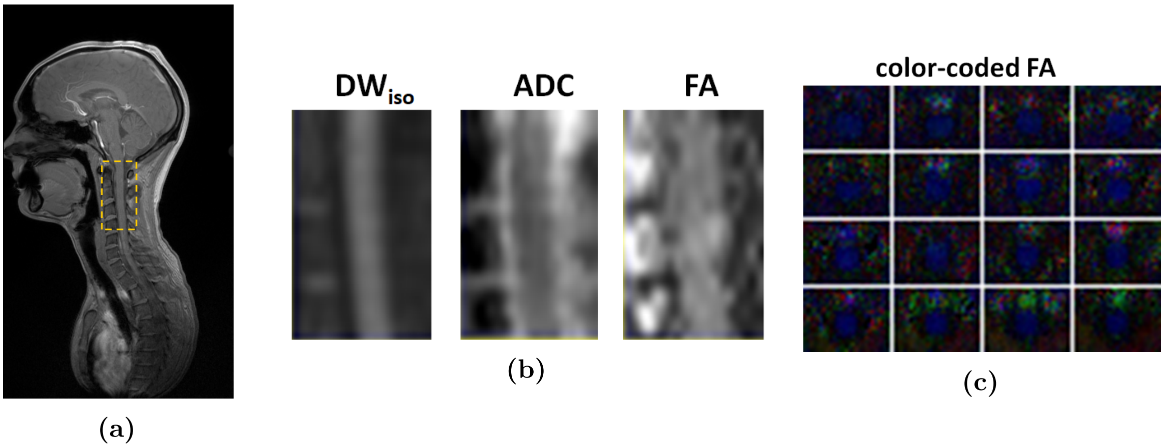

Figure 5.5: **(a)** Localizer of a volunteer with measured stack marked (orange). **(b)** Sagittal 2DRF inner-FOV STEAM reconstructions of isotropic diffusion-weighted images (DW_{iso}), maps of the apparent diffusion coefficient (ADC) and the fractional anisotropy (FA) and **(c)** transverse slices of color-coded FA with a resolution of 2x2x4 mm^3

SNR is nearly equal (99%) for full FOV centric reordered acquisition and inner-FOV HF acquisition.

The in vivo measurements were realized with an in-plane resolution of 2x2 mm^2, a FOV of 40x128 mm^2 and 16 mm phase-encoding oversampling. This resulted in a flip angle of 23°. We measured 16 slices with a thickness of 4 mm and 16 repetitions. The time to measure a single line was 6.08 ms which results in an echo spacing TE2 in between each echo of 6.90 ms. The time TE1 needed for the diffusion weighting was 37 ms. DWI is performed with a Stejskal-Tanner gradient pulse pair. Thereby the duration δ was 12 ms and the diffusion time Δ 24 ms. The DWI was performed with a b-value of 500 s mm^{-2} for six non-collinear directions. The total repetition time TR was 2800 ms, which results from the transition time T_M of 10 ms, the echo time TE 1 and the k-space measurement. The total measurement time thus amounted 5.14 min.

One single-shot DWI 2DRF STEAM in vivo measurement is shown in figure 5.5. In the images the spinal cord can be clearly depicted. However, in comparison to EPI acquisitions the SNR is smaller by ~20%. This is in accordance with SNR measurements performed in water phantoms and literature [42, 60], where EPI showed a better SNR compared to single-shot STEAM as well. As the α flip angle is decreased only a small part of the "stored" magnetization is refocused to be able to measure a full slice with the total "stored" magnetization and multiple α pulses. As result the measured signal is decreased as well. This and the longer acquisition time needed in comparison to the EPI are the reason for the lower SNR. On the other hand it is possible to utilize larger bandwidths with STEAM

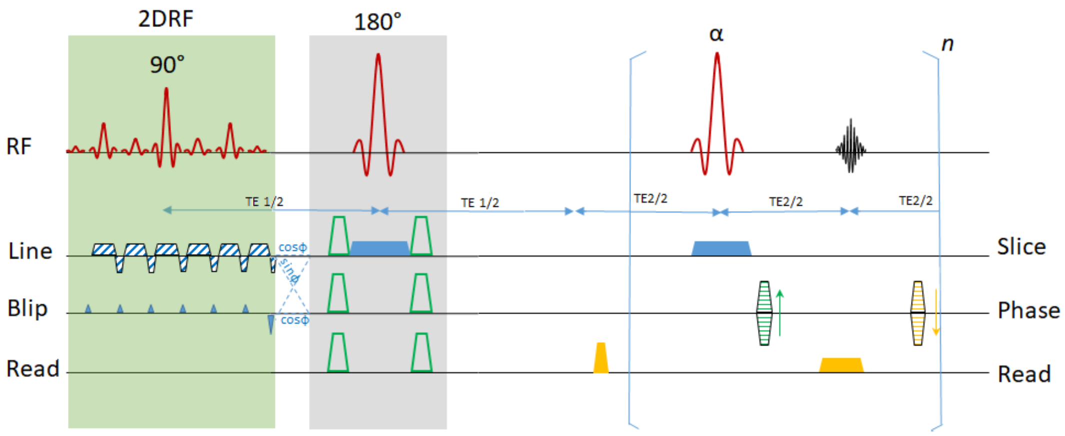

Figure 5.6: schematic sketch of a FSE sequence combined with a tilted 2DRF excitation pulse (green shaded) and a Stejskal-Tanner diffusion module (grey shaded).

and thus a larger frequency range can be covered.

5.2.2 FSE

A schematic FSE sequence combined with DWI and 2DRF inner FOV excitations is sketched in 5.6. The FSE is combined with a Stejskal-Tanner diffusion module (shaded green) and a 2DRF tilted excitation (shaded grey). Additionally, the possibility to use cross sectional excitations is given, similar to the STEAM sequence. The difference in-between FSE and STEAM is that after a single 90 degree excitation pulse each echo is refocused by an 180 degree pulse and reused. The FSE principle is explained in 2.2.2.
The sequence was probed first in phantoms and afterwards in healthy volunteers, one of these measurements is shown in 5.7. To achieve a comparability between STEAM and FSE we used an equal resolution 2x2x4 mm^3 in a FOV of 40x128 mm as well as the same amount of slices and averages. Further half Fourier sampling and tilted 2DRF excitations with an angle ϕ of 15° were used. The difference in the measurements can be found in the measurement times. The echo time used for the diffusion module TE1 was 42.5 ms and the echo spacing TE2 was 8 ms. The repetition time TR was 3200 ms as else the SAR limit would be reached. This led to a total measurement time of 5.58 min.
Timing wise it would be possible to accelerate the sequence even further, but due to the repetitive usage of 180° pulses a lot of energy is deposited in the volunteer. Thus, to reduce the deposited energy the repetition time has to be increased significantly to ensure the special absorption rate is not exceeded. Further the flip angle of 180° is reduced to 160°,

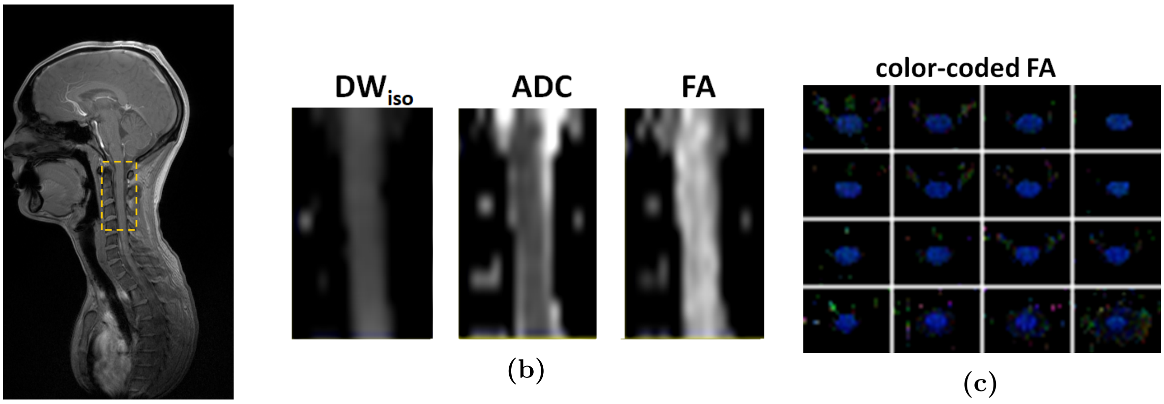

(a) (b) (c)

Figure 5.7: **(a)** Localizer of volunteer with measured stack marked (orange). **(b)** Sagittal 2DRF inner-FOV FSE reconstructions of isotropic diffusion-weighted images (DW_{iso}), maps of the apparent diffusion coefficient (ADC) and the fractional anisotropy (FA) and **(c)** transverse slices of color-coded FA with a resolution of 2x2x4 mm^3

to additionally ensure that the SAR limit is not exceeded and the repetition time is not increased unreasonably. In figure 5.7 the results of a tilted 2DRF DWI FSE measurement is shown. To obtain SNR values the mean averages and the standard deviation were obtained from the non weighted acquisitions and the voxel-wise ratio of them was determined over ROIs in the spinal cord.

In comparison to the single-shot STEAM acquisitions at the same volunteer the FSE shows a SNR gain of $\sim$32% which is in accordance with water phantom measurements which were performed. The difference comes from the individual refocusing of each echo with 180° pulses. Even in comparison to EPI acquisitions the FSE acquisitions do not lack, they have show an increase in SNR of $\sim$14%. However, the EPI acquistion time is reduced by a third in comparison and thus the SNR efficiency of EPI is still higher. This is in accordance to prior made observations at water phantoms and literature [1]. In the sagittal reconstructions both STEAM and FSE show no distortions as e.g. bending or squeezing which can occur during EPI acquisitions and seem to be rather robust.

5.2.3 Sequence Comparison in Phantoms With Metallic Objects

First measurements near metallic artifacts were carried out with a phantom consisting of a cucumber larded with 20 cent coins. Non diffusion weighted measurements performed with EPI, STEAM and FSE, are presented and compared in figure 5.8. The measurement parameters used were slightly adapted. No averaging was performed, the resolution was

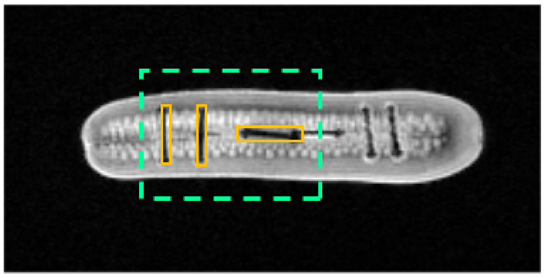

(a) **Localizer**

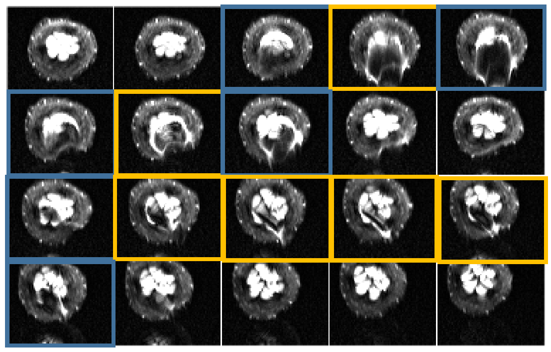

(b) **EPI**

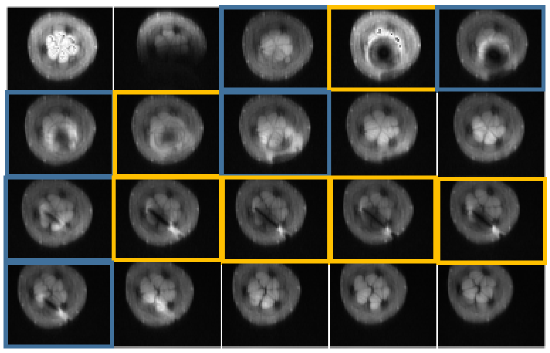

(c) **STEAM**

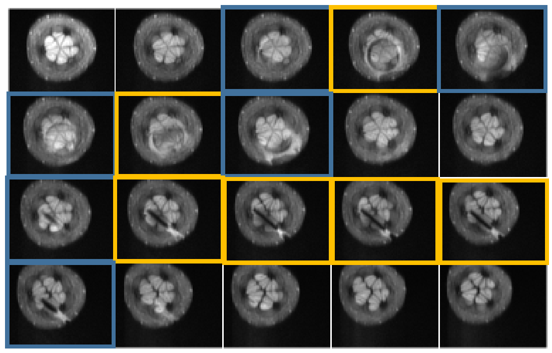

(d) **FSE**

Figure 5.8: (a) Localizer of a cucumber larded with 20 euro cent coins highlighted by yellow rectangles and the measured slice stack highlighted in turquois. **(b)** 20 transversal slices acquired with an EPI sequence, **(c)** STEAM sequence and **(d)** FSE sequence. All acquisitions were performed with 2DRF inner FOV excitations. In yellow the regions where the coins are located is highlighted. Blue marked areas show slices neighboring the coins.

1x1x4 mm^3 and the FOV was 40x128 mm^2.

The EPI acquisitions show that they suffer from pronounced geometric distortions and signal dropouts. This can not only be observed in the slices where the metallic objects are present, but as well in the slices close to them.

In case of the single-shot STEAM acquisitions the slices can be well depicted, even the geometry of the coins and the cucumber surrounding them. In the FSE images all three coins can be depicted as well and only a low amount of displacements can be observed. In comparison with EPI both single-shot STEAM and FSE show a better robustness and image quality. The slices acquired with single-shot STEAM have in comparison to the FSE a slightly reduced image quality, due to the lower SNR, still both methods seem to be applicable close to metallic implants.

Thus, first diffusion weighted measurements were performed at the same volunteers, as

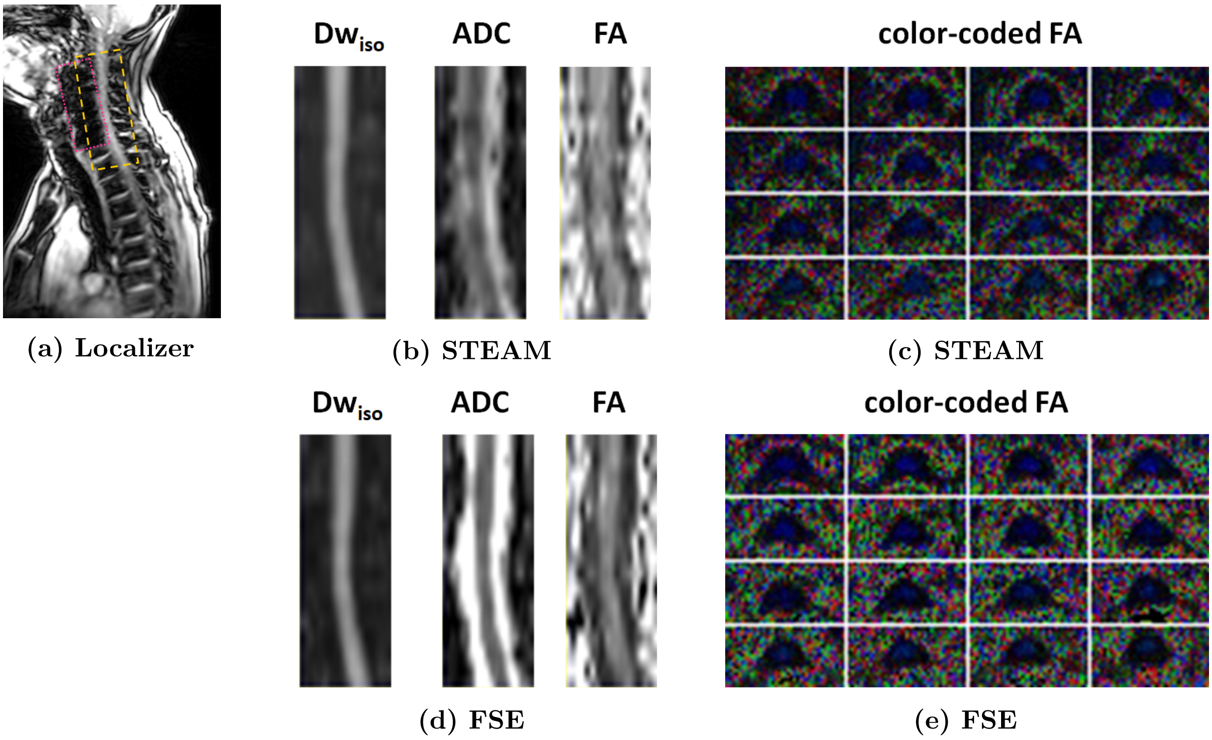

Figure 5.9: (a) Localizer of a volunteer with metallic cage (highlighted magenta) and measured stack marked (orange). Sagittal 2DRF tilted STEAM **(b)** and FSE **(d)** reconstructions of DW$_{\text{iso}}$, ADC and the fractional anisotropy. **(c)** and **(e)** show transversal color-coded FA slices of STEAM and FSE, respectively.

shown for the EPI measurements (Figure: 5.1 and 5.2), with six non-collinear directions and one without diffusion weighting, with a b value of $500\,\mathrm{s\,mm^{-2}}$, δ of 9 s and Δ of 24 ms. First, the volunteer with a metallic cage in the larynx area is presented in figure 5.9. Second, in figure 5.10 the volunteer with multiple screws and plates in the thorax area is shown. 16 slices were measured with 20 repetitions, a resolution of $1.5\text{x}1.5\text{x}5.0\,\mathrm{mm}^3$ and a FOV of $30\text{x}128\,\mathrm{mm}^2$.

In the first figure 5.9 a good image resolution of single-shot STEAM and FSE acquisitions can be observed. The SNR of the single-shot STEAM acquisition is lower by $\sim 28\%$ in comparison to the FSE acquisitions. However, both measurements show less distortions compared to the EPI acquisitions in figure 5.1. The sagittal EPI reconstructions showed a curvature with constrictions and widening. The STEAM and FSE reconstructions present a smooth and in comparison uniform curvature of the spinal cord. In case of the color-coded FA this observation is underlined, while the spinal cord looks squeezed in the EPI images, in the single-shot STEAM and FSE acquisitions the spinal cord looks fuller and not as squeezed. On the other hand the EPI acquisitions took about half the time, to

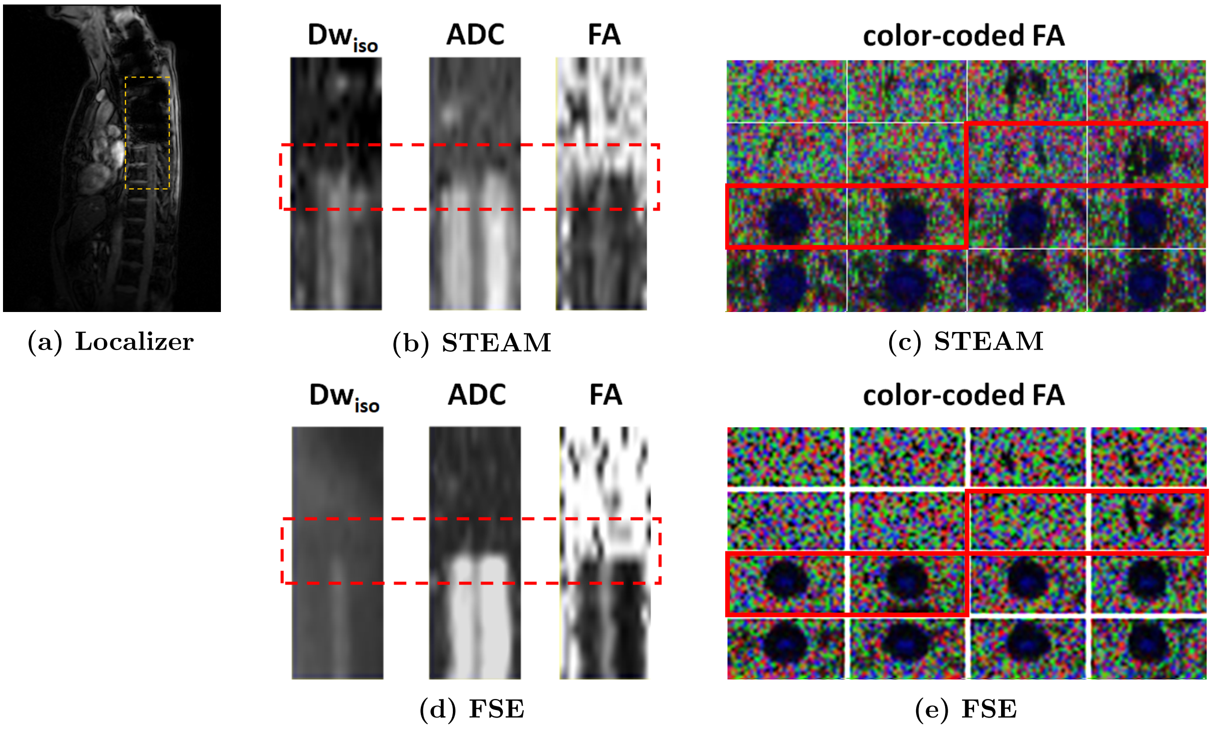

Figure 5.10: **(a)** Localizer of a volunteer with metallic screws and bars implanted with measured stack marked (orange). Sagittal 2DRF inner-FOV STEAM **(b)** and FSE **(d)** reconstructions of DW_{iso}, ADC and the fractional anisotropy. **(c)** and **(e)** show transversal color-coded FA slices of STEAM and FSE, respectively. The 7th to 10th slices are highlighted, as they show the most variations (detail see text).

achieve a reasonable image quality.
Further the question which has to be posed is, how strong the influence of the metallic cage actually is in comparison to the distortion due to varying tissue susceptibilities. In case of the healthy volunteers small distortions are visible during EPI measurements as well, which are not visible with STEAM and FSE. However, due the prolonged measurement time STEAM and FSE are not as feasible as EPI for DWI. In case of larger metallic implants it was shown, that EPI suffers of signal cancellation in figure 5.2. For the comparison in figure 5.10 single-shot STEAM and FSE measurements of the same slice stack measured in the same volunteer are presented. In the first impression no big difference is visible between FSE, STEAM and EPI acquisitions (fig.: 5.2**(b)**,**(c)**). All three techniques suffer from signal cancellations after about half of the slice stack is measured. With a more accurate observation, however, differences can be seen between the 7th and 10th slice (highlighted in red). In case of the FSE and single-shot STEAM the sagittal reconstructions show slightly more signal close to the cancellations and are less distorted. In the color-coded FA

this observation can be confirmed. The spinal cord does not appear squeezed or widened and in the 8th and 9th slice slightly more signal is visible.
The results, however, are underwhelming and do not make single-shot STEAM and FSE a reasonable alternative to EPI near metallic artifacts. Thus, we investigated how to improve the performance of the techniques further at phantoms.

5.3 Sequence Improvement

To improve the measurements near metallic implants the performance of the respective techniques and sequences – FSE and STEAM – are investigated individually and combined with new techniques.

The first improvement is to use slice selective gradients of equal strength. The reason is that the spatial displacement of the gradients is different and thus the 90° and 180° excitations do not overlap. As a result the RF pulses are squeezed, widened and or

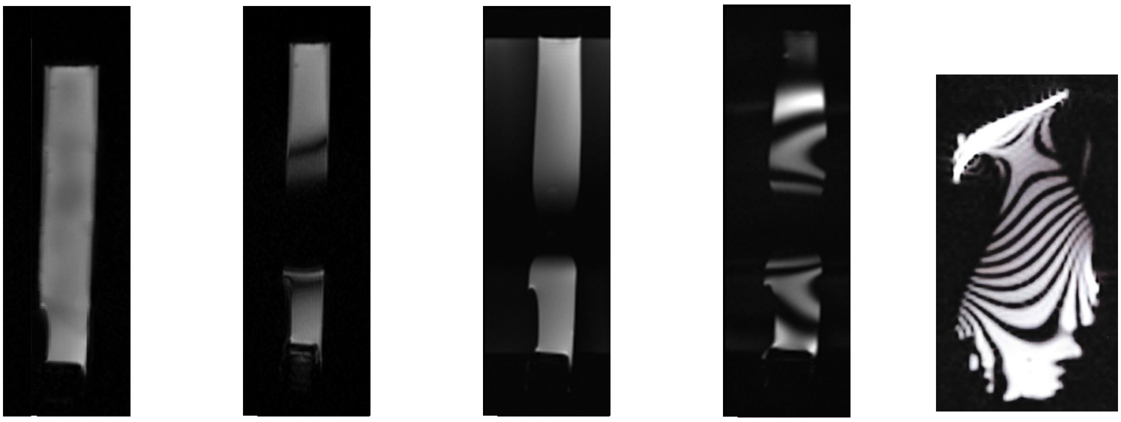

(a) Localizer bottle without screws

(b) FSE different slice selective gradients

(c) FSE equal slice selective gradients

(d) FSE 2DRF inner FOV

(e) 2DRF **SE**

Figure 5.11: (a) FLASH localizer of investigated water phantom swith no screws. **(b)** FSE acquisition of water phantom surrounded with 2 aluminum screws and varying slice selective gradient strength (90°: $9.00\,\mathrm{mT\,m^{-1}\mu s^{-1}}$, DWI: $3.00\,\mathrm{mT\,m^{-1}\mu s^{-1}}$ and alpha pulse: $6.00\,\mathrm{mT\,m^{-1}\mu s^{-1}}$) **(c)** FSE acquisition with equal slice selective gradients for all RF pulses of $6.00\,\mathrm{mT\,m^{-1}\mu s^{-1}}$. The amount of cancellations in the middle of the bottle are decreased due to the adaption of the gradients.
(d) FSE acquisition with tilted 2DRF inner FOV with adapted slice selective gradients of water phantom surrounded by 2 aluminum screws. **(e)** sagittal SE acquisition of a standard cylindrical water bottle, as presented in 3.2, surrounded by two aluminum screws. The screws are attached to the bottom of the bottle (right side).

excite a different region. In case the gradient strength is equal for all excitations they all are affected by the magnetic inhomogeinities in the same manner. This enhances the probability that the same slice is excited by the pulses. To achieve gradients of equal strength the excitation duration was adapted for FSE and single-shot STEAM, resulting in the remaining measurements the 90 degree pulses had a duration of 2560 μs and the 180 diffusion degree pulses a duration of 7680 μs. The repetitive RF excitations, used for the read out, had a duration of 2560 μs. This results in slice selective gradients with an amplitude of $6.00\,\mathrm{mT\,m^{-1}\mu s^{-1}}$. In figure 5.11 **(b)** and **(c)** of the adaption in case of FSE acquisitions is presented. The acquisition with different slice selective gradients **(b)** show significantly more cancellations compared to the acquisition with adapted gradients **(c)**. As the 2DRF excitations are created by variable gradients and different RF-envelopes of which each can possibly be influenced differently by magnetic offsets the effect on them was investigated next. The influence of metallic artifacts on 2DRF excitations was probed with a spin echo and a FSE sequence at varying water phantoms surrounded by two aluminum screws, shown in 5.11**(d)** and **(e)**.

In comparison with the in **(c)** shown FSE acquisition without 2DRF excitations at the implant phantom strong distortions and signal cancellations are visible even far away from the metallic screws for the acquisitions with 2DRF excitations. The cancellations and distortions in the images give the impression of electromagnetic waves emitted from the aluminum screws. Thus, one possible reason could be that due to the rapid switching of gradients in combination with multiple RF pulses, to create a 2DRF excitation an electromagnetic field is induced into the metallic screws which as a result can could create an additional magnetic field. This magnetic field is contributing to the magnetic field inhomogeinity ΔB_i and lead to perturbations of the resonance frequency in areas, which before were not influenced.

Another reason could be that the encoding gradients used to create a 2DRF excitation are influenced by magnetic inhomogeinities. The field inhomogeinities can lead to an additional precession and resulting the tilted lines, needed for the 2DRF excitations, cancel each other out. Thus, the shape of the inner FOV is squeezed and or bent and does not excite in e.g. a square shape. Further the location of the side excitations can be displaced as well and thus saturation effects and or folding artifacts can occur in the images which lead to additional cancellations and distortions. A possible solution could be to adapt the 2DRF excitations depending on the distortions and to consider the magnetic inhomogeinities for the calculation of the 2DRF excitations. However, as this would have to be adapted for every possible implant combination, shape and position this is rather complicated and not

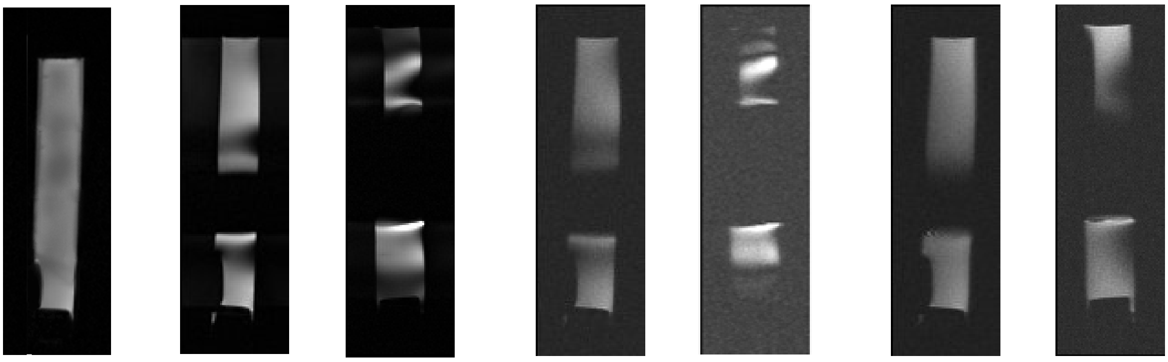

(a) (b) FSE DWI 180° ZOOM (c) STEAM DWI 180° ZOOM (d) STEAM alpha ZOOM

Figure 5.12: **(a)** Implant phantom with no screws acquired with FLASH. **(b)** to **(d)** Sagittal acquisitions of the implant phantom surrounded by 2 (left) and 4 (right) aluminum screws, respectively. **(b)** shows images acquired with a FSE 180° ZOOM inner FOV technique. **(c)** shows acquisition with single-shot STEAM 180° ZOOM. **(d)** presents slices acquired with an alpha ZOOM single-shot STEAM combination, where the α flip angle is rotated.

feasible.

For acquisitions of the spinal cord with FSE and STEAM an inner FOV is nearly mandatory. Inner FOV techniques reduce the amount of k-space lines to be measured, thus in case of STEAM the possibilities to use larger flip angles and shorter repetition times are given, and in case of FSE repetition time and SAR can be reduced. As result the image acquisition time is reduced as well. As 2DRF excitations are not feasible near metallic objects, as they increase the cancellations, as alternative inner FOV technique cross sectional excitations and their behavior near metallic objects was investigated in the following.

For the STEAM sequence we investigated two possible cross sectional approaches: First, the in the previous chapter applied rotation of the 180° diffusion excitation. Second, the rotation of the alpha flip angle, to enable the use of shorter RF pulse durations and as result also the possibility to use broader bandwidths. This is only possible in case of the alpha pulse and not the 180° pulse due to the small B_1 amplitude due to the smaller flip angle. For the FSE sequences we used ZOOM only with the 180° diffusion pulse. The first 90° was not rotated, for either FSE or STEAM, as we applied MAVRIC on it and thus used frequency selective 90° pulses. This will be described in detail later in the chapter.

The cross-sectional inner FOV acquisitions are presented in 5.12 at the implant water phantom with different numbers of screws attached. In all six cases in the vicinity of the screws strong cancellations are visible, however, if compared all acquisitions differ. In

regions with no cancellations the FSE acquisitions show a ∼34% higher SNR compared to the single-shot STEAM acquisitions, as also observed in previous acquisitions at water phantoms and in vivo. The distortions in the acquisitions with two screws are rather small, but seem to be more pronounced for the FSE than the STEAM images. For the acquisitions with four screws and ZOOM 180° this observation is reversed. The distortions present in the STEAM 180° ZOOM images look more severe than in case of the FSE.
The signal difference between the STEAM and FSE 180° measurements is probably due to the different alpha pulse angles used for the read out. In case of the single-shot STEAM acquisitions an angle of 23° was used compared to an angle of 160° used for the FSE acquisitions. Thus, the latter is probably not influenced as strongly by the magnetic inhomogeinities as STEAM. Further during the single-shot STEAM acquisitions only stimulated echoes are measured where with FSE stimulated and normal spin echoes are measured. This could lead to additional signal loss and thus the cancellations in case of the single-shot STEAM 180° acquisitions are slightly stronger in comparison to the FSE acquisitions.
For both configurations –two and four screws– the images with the least distortions are obtained by the STEAM acquisitions with the alpha pulse rotated. This can be explained as in case of the single-shot STEAM alpha acquisitions the read out bandwidth is higher, 2000 Hz compared to 1000 Hz used for the 180° ZOOM approaches. To enable the larger bandwidth the RF pulse duration has to be reduced to 512 μs. Thus, the slice selective gradients of the excitations differ and thus the signal should be reduced and or stronger distorted, however, as a larger frequency range can be covered, due to the larger bandwidth this effect is compensated. This will be further explained in the scope of the MAVRIC acquisition later this chapter.
Still in comparison to the acquisitions performed with 2DRF excitations the distortions are much less severe for all three approaches. Thus, ZOOM inner FOV seems to be a good alternative, even though the 2DRF approach showed slightly better results without metallic implants.

5.4 Correction of Resonant Frequency Offsets

The enhance the performance of the sequences even further, two methods were added to STEAM and FSE: view-angle tilt (VAT) and multi acquisition variable-resonance image combination (MAVRIC) which are explained in 2.6.2 and 2.6.3.

For FSE and single-shot STEAM VAT was applied by replaying the slice selection gradient during the signal read out. As result the in-plane distortions due to the field inhomogeinities should be reduced.
MAVRIC was applied because metallic objects not only lead to in-plane distortions but also to distortions in slice direction due to resonance frequency offsets. There for the first excitation is adapted, for single-shot STEAM and FSE, to a frequency selective excitation instead of a slice selective excitation. As result a specific frequency range can be excited. To measure the full range of frequency offsets, they are split in separate bins and are measured individually by repetitively applying either FSE or single-shot STEAM with different transmission and receiver frequency. The separately acquired images are combined by either averaging or by calculating them with maximum intensity projection. Both methods could enhance the signal significantly and thus are investigated in combination with single-shot STEAM and FSE without and with inner FOV cross sectional excitations to exclude that the techniques influence each other negatively.

5.4.1 VAT and MAVRIC Without Cross-Sectional Excitations

VAT and MAVRIC are probed, separately and combined, without ZOOM at the implant phantom with two screws. Single slice acquisitions are presented in figure 5.13. For the standard acquisition of FSE and STEAM the cancellations in the area of the 2 metallic screws are apparent. In the VAT acquisitions the additionally applied slice selective gradient during the read out gradient led to a rotation of the read out plane of $\Theta_{\mathrm{VAT}} = 9°$.

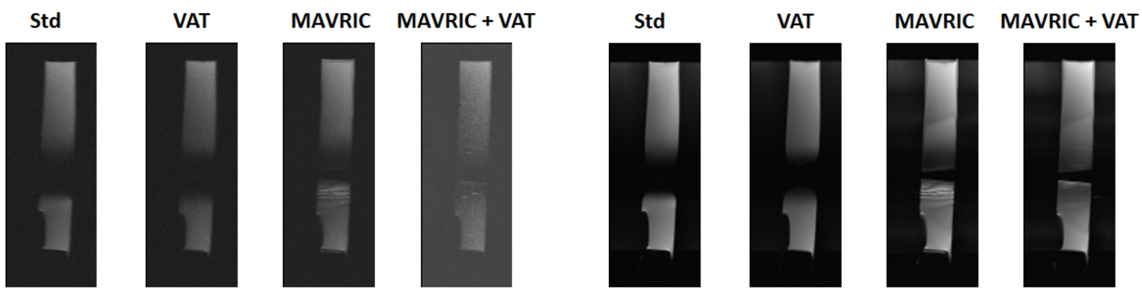

(a) STEAM **(b)** FSE

Figure 5.13: Sagittal single slices acquired with standard, VAT, MAVRIC and MAVRIC combined with VAT (left to right) single-shot STEAM and FSE sequences. Thereby a VAT angle Θ_{VAT} of 9° and a frequency range of 10 kHz to -10 kHz was scanned with an increment of 1 kHz in an interleaved manner for MAVRIC. The MAVRIC images were calculated using a maximum intensity projection across the frequency offsets.

The angle is calculated with equation 2.22. The images acquired with VAT show nearly no difference compared to the acquisitions without VAT. In the transition zone between the cancellations and the areas were the water bottle can be depicted slight variations in signal intensity can be observed, however, they are only marginal.
For the MAVRIC acquisitions the frequency was scanned with an increment of 1 kHz with 21 steps in between 10 kHz and -10 kHz and a RF pulse bandwidth of 1000 Hz. This resulted in total measurement times of about 42 s for FSE and 11 s for STEAM. The FSE measurement time was increased to prevent reaching the SAR limit. The MAVRIC images were calculated with a maximum intensity projection across the frequency offsets for each slice on the fly. In the MAVRIC image it can be observed that nearly the complete bottle can be resolved. In the vicinity of the screws the signal is not as strong as further away and in addition to the cancellation in its vicinity slight distortions can be observed. These distortions can arise as the two frequency selective measurements overlap. This can lead in case of consecutive measurements to saturation effects and thus signal loss. A different reason could be in-plane distortions, as with MAVRIC only distortions in slice direction are corrected. The distortions can displace the signal within an acquisition and thus result in the final image in signal enhancement or cancellations.
As solution MAVRIC and VAT were used together in the last image, with $\Theta_{\mathrm{VAT}} = 9°$, a frequency range from 10 kHz to -10 kHz and an increment of 1 kHz, as in the previous acquisitions. The image quality increases slightly compared to the acquisitions without VAT, only a small gap on the level of the screws is visible. Thus, it can be assumed that the distortions present in MAVRIC measurements are due to in-plane distortions, which get counteracted by VAT. The image quality of the MAVRIC acquisitions is directly connected to the frequency limits, the RF-bandwidth and the frequency increment with which the frequency range is scanned. Depending on the extent of the frequency inhomogeinities and the resulting displacement, induced by the metallic object, the frequency limits have to be arranged. For the implant phantom surrounded by 4 aluminum screws this is illustrated in 5.14. In **(a)** frequency selective acquisitions of a slice out of 10 are displayed in a range of 4 kHz to -4 kHz, scanned with an increment of 1 kHz. In the first images, 4 to 3 kHz, no signal seems to be obtained or rather only a negligible amount which does not contribute to the final image calculated with maximum intensity projection. Thus, they could be left out for the acquisition to reduce the measurement time.
Between 1 kHz and -1 kHz the most signal is obtained. In the following frequency selective acquisitions only a small amount of signal is obtained. However, each acquisition contributes to the final image. In case the frequency range would have been increased up to -14 kHz

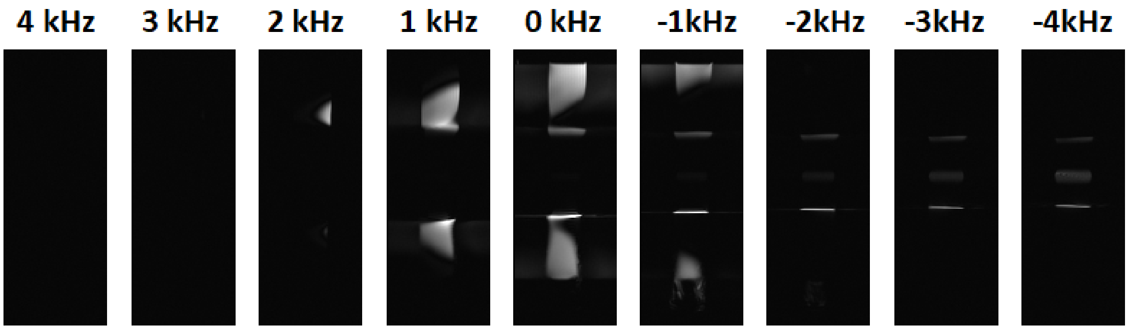

(a) **Frequency selective acquisitions**

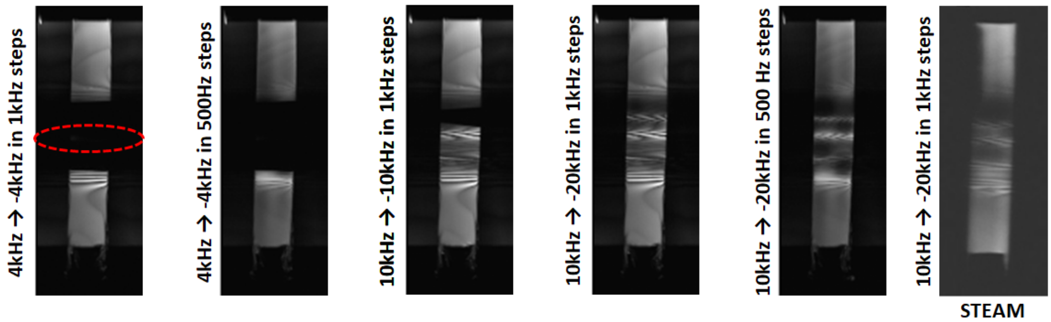

(b) **Maximum intensity projection**

Figure 5.14: **(a)** Unedited FSE VAT MAVRIC frequency selective acquisitions in a range from 4 kHz to -4kHz with 1 kHz steps and RF bandwidths of 1 kHz. Maximum intensity projections of one out of ten measured slices calculated from VAT MAVRIC acquisitions with constant RF pulse bandwidths of 1 kHz, varying frequency ranges and increment steps presented in **(b)**: 4 kHz to -4 kHz with 1 kHz, 4 kHz to -4 kHz with 500 Hz, 10 kHz to -10 kHz with 1 kHz, 10 kHz to -20 kHz with 1 kHz, 10 kHz to -20 kHz with 500 Hz and 10 kHz to -20 kHz with 1000 Hz, from left to right, respectively. The first five images are acquired with a FSE and the sixth is acquired with a single-shot STEAM. In the first image the frequency selective acquisitions shown in **(a)** are combined and the red dotted circle highlights a very faint signal which is more pronounced in the frequency selective acquisitions (-2 to -4 kHz).

small signal stripes would have been obtained with each selective acquisition which contribute to the final maximum intensity projection (see 5.14 **(b)**). Thus, it could be reasonable to increase the frequency limits for acquisitions near aluminum screws to obtain a nearly fully undistorted image.
The combined maximum intensity projection of the single frequency selective acquisitions in **(a)** are shown in the first image of figure 5.14 **(b)**. In the region of the aluminum screws large cancellations are visible even though in the frequency selective acquisitions small amount of signal is measured in the middle of the bottle. However, the signal is to weak

and thus only a very small stripe with nearly no intensity can be seen (highlighted by red dotted circle). In addition to the cancellations wave shaped distortions are visible in the bottle. They occur as during the scanning of the distorted frequencies some of them are missed. The reason there for is probably that either the RF pulse bandwidths used are to small and or the frequency increment used is to large. Thus, in the second image the frequency increment was reduced to 500 Hz while the bandwidth was hold constant at 1 kHz. As the frequencies are measured in an interleaved manner no saturation effects occur as the consecutive frequencies measured have a sufficient distance. Due to the decreased increment the frequencies are scanned twice and thus no signal is missed out. This leads to less distortions and a slight signal gain in comparison to the first image. This approach, however, doubles the measurement time needed.
To decrease the signal cancellations in the region of the metallic screws even further we increased the frequency range to 10 kHz and -10 kHz and scanned again with a frequency increment of 1 kHz. As result the size of the cancellation decreases in comparison to image one and two. Nearly the full bottle can be distinguished only in a small region cancellations are still visible. Further the wave shaped distortions, which we observed in the first image due to the to large frequency increments, returned. The signal obtained can be compared to the VAT MAVRIC FSE single slice acquisition at two screws (fig. 5.13 **(b)** 4th image). Additional distortions can be observed in the vicinity of the added screws. However, the signal drop out is not as strong as before and the bottle is equally good recognizable. This indicates that the frequency offsets generated by the screws interact with each other, as mentioned in section 2.6.
To acquire the full bottle without cancellations we increased the measured frequency range even further to 10 kHz and -20 kHz and scanned again with an increment of 1 kHz. As a result it is possible to depict the full water bottle without cancellations, but still with wave shaped distortions. To cancel them out as well the frequency increment was changed to 500 Hz and the bottle was scanned once more The maximum intensity projection is presented in the fifth image. The obtained image shows a reasonable signal quality, the distortions are nearly completely gone and the water bottle is completely visible, only the single acquisition time for ten slices is with 19.4 min rather long.
In the 6th image a single-shot STEAM MAVRIC acquisitions in a frequency range of 10 kHz to -20 kHz scanned with 1 kHz steps, is presented. Again in the full bottle signal can be obtained. The SNR is slightly decreased ($\sim 23\%$) in comparison to the FSE acquisition. However, the measurement time for a single frequency compared to the FSE acquisitions is approximately halved, due to the decreased energy deposition during the single-shot

STEAM. Further as only an increment of 1 kHz was used, the total measurement time was reduced to 5.9 min.

5.4.2 VAT and MAVRIC Combined With Cross-Sectional Excitations

The previous measurements of VAT and MAVRIC show that the combination with FSE and STEAM is a reasonable approach for the image acquisition near metallic artifacts. To further enhance the robustness and to shorten the acquisition time they are combined with ZOOM, to enable the possibility to image small areas, e.g. spinal cord. MAVRIC and VAT were combined with single-shot STEAM 180° ZOOM, single-shot STEAM ZOOM alpha, and FSE 180° ZOOM. The measurements were performed in sagittal orientation with an in-plane resolution of 1.0x1.0 mm^2, a FOV of 40x128 mm^2 and HF sampling. They contained 20 slices measured in an interleaved manner with a thickness of 4 mm. For all measurements Θ_{VAT} of 9° was used. The ZOOM 180° acquisitions were performed in a frequency range of 10 kHz to -20 kHz with an increment of 1 kHz which results in 31 frequency steps. The rotation angle for ZOOM was 15° with a thickness factor of 70% which resulted in an effective FOV of 48 mm, due to an additional phase oversampling of 60%. The FSE acquisition of a single frequency took 900 ms and a frequency selective single-shot STEAM acquisition 320 ms. The large timing difference arises to ensure that during the FSE acquisitions the SAR limits are not exceeded. This results in total measurement times of 9.18 min and 3.20 min, respectively. For single-shot STEAM alpha acquisitions the RF pulse duration can be reduced to 512 ms, thus the RF bandwidth can be increased to 2000 Hz. As a result the frequencies in the range of 10 kHz to -20 kHz can be scanned twice with equal scan rate due to the repetitive measurement in an incremental manner and thus the distortions should decrease even further. Additionally the repetition time, in comparison to the 180° ZOOM approach, was reduced to 210 ms as due to the reduced duration of the alpha pulses duration the repetition time for the read out can be reduced as well. As result the total measurement time was reduced to 2.1 min.

In figure 5.15 7 out of 20 slices are pictured of various measurements at the implant phantom with 4 aluminum screws. The in the first row presented standard cross sectional inner FOV acquisitions without MAVRIC or VAT all show large cancellations similar to the single slice acquisitions presented in figure 5.12. The application of VAT in the second row leads to a small increase in signal strength. The usage of MAVRIC in the third row leads to a significant increase in signal intensity and the combination of MAVRIC and VAT shows an additional signal gain.

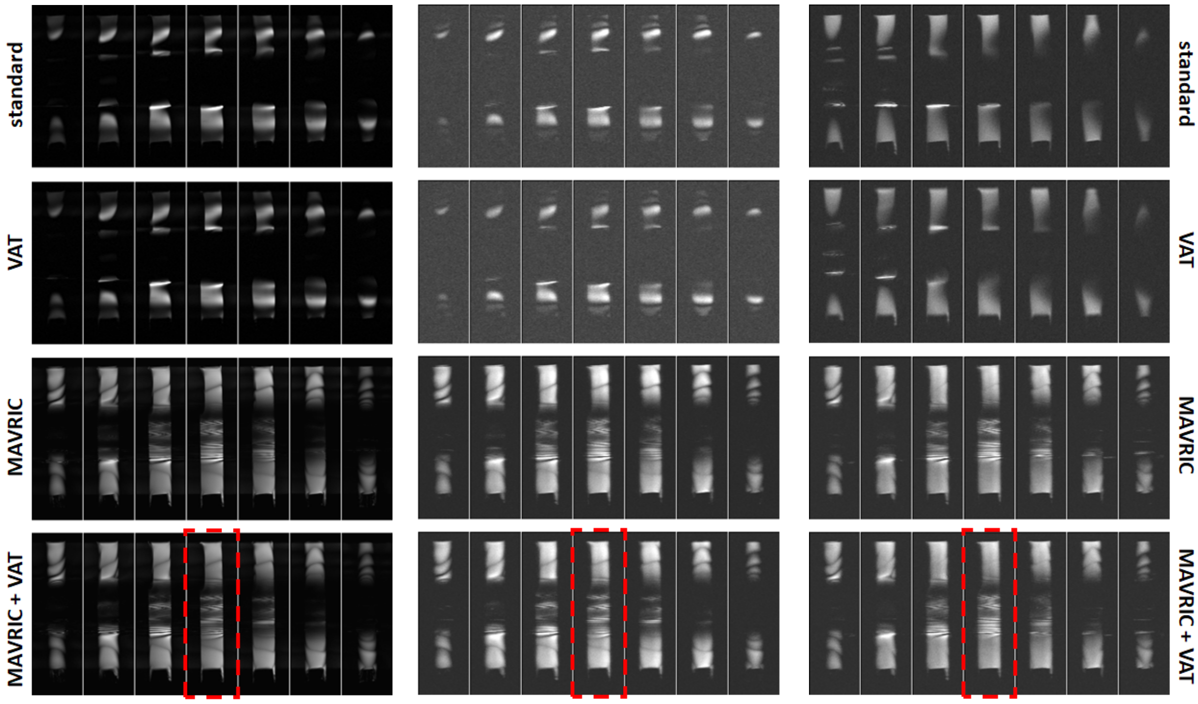

(a) 180° ZOOM FSE **(b)** 180° ZOOM STEAM **(c)** Alpha ZOOM STEAM

Figure 5.15: illustrates 7 out of 20 slices acquired at the implant phantom surrounded by 4 screws with three different sequences, 180° ZOOM FSE, 180° ZOOM STEAM and alpha ZOOM STEAM (l.t.r.). In the first row images acquired without additional applications are presented, detailed measurement parameters are discussed in the text. For the images below the sequences were combined with VAT. In the third row maximum intensity peak acquisitions, obtained with MAVRIC in a frequency range of 10 kHz to -20 kHz are shown. It was scanned with an increment of 1 kHz in **(a)** and **(b)** and in **(c)** an increment of 2 kHz was used. In the last row the sequences were combined with VAT and MAVRIC and the maximum intensity projection calculated. The in slices highlighted in red are acquired at the same position as in 5.14 **(b)** image 4 and 6.

This behavior is in accordance with the observations made at the acquisitions without ZOOM: VAT alone does not increase the signal sufficiently, MAVRIC leads to a significant increase of image quality and both combined show the best performance. The middle acquisition (highlighted by red dotted rectangle) can be compared to VAT MAVRIC acquisitions in image 4 and 6 of figure 5.14 **(b)** as they are acquired at the same position. In the FSE acquisitions with and without ZOOM nearly no difference can be spotted. For the single-shot STEAM acquisitions the image quality is also nearly equal. The alpha ZOOM acquisitions show an even bigger decrease in distortions compared to the acquisitions without ZOOM or 180° ZOOM. The distortions are lower for the alpha acquisition, due to the repetitive scanning of the frequencies because of the increased bandwidth, in

comparison to the other two acquisitions. In case of the 180° ZOOM and the acquisition without ZOOM (fig.:5.14 **(b)** img. 6) a RF bandwidth of 1 kHz is used compared to a 2 kHz bandwidth used for the ZOOM alpha acquisitions.
The efficiency of FSE and single-shot STEAM with MAVRIC and VAT increases if inner FOV ZOOM is used, by nearly a factor of two as the measurement times can be halved and no SNR loss is observed compared to acquisitions without ZOOM. Thus, it can be said the combinations of ZOOM with MAVRIC and VAT are a valid option for investigations near metallic objects.

5.4.3 Influence of Metallic Objects on Signal Cancellations

In the previous section it was shown that the signal obtained with MAVRIC strongly depends on the frequency limits. Thus, the general extent of the frequency displacement induced by metallic objects should always be considered during the acquisitions. This poses a rather difficult task as the metals all differ in susceptibilities and thus the strength with which the frequencies are displaced differs. Further depending on the region measured the influence might change as well depending on the surrounding tissue, e.g. near the lung or near fat.

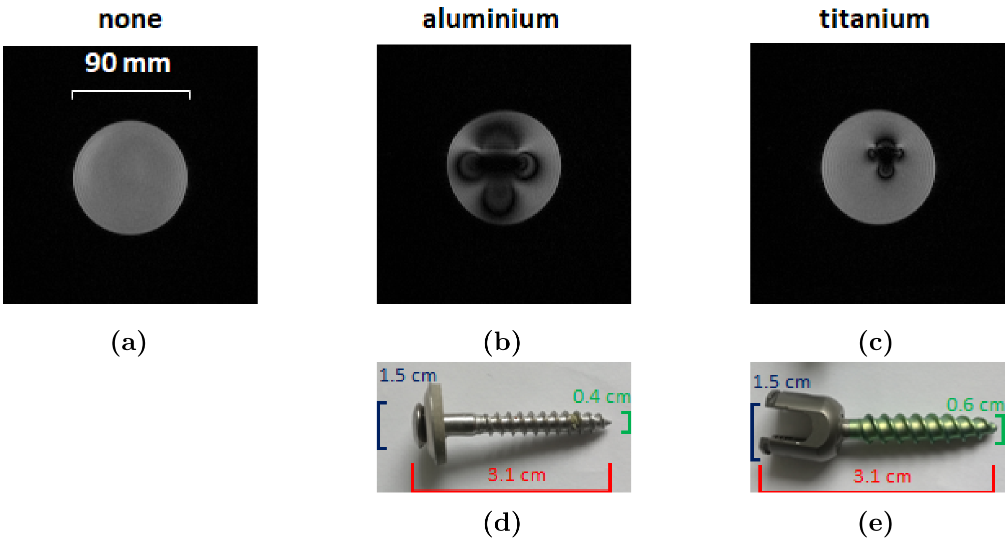

Figure 5.16: Three transversal FLASH acquisitions of a water bottle **(a)** filled with an aluminum screw **(b)** or an titanium screw **(c)**. The aluminum screw is shown in **(d)** it has a length of 3.1 cm, a diameter of 0.4 cm and a head size of 1.5 cm. The titanium screw shown in **(e)** has a length of 3.1 cm, a diameter of 0.6 cm and a head size of 1.5 cm

To illustrate this in figure 5.16 an aluminum screw **(b,d)** and a titanium screw **(c,e)** with similar dimensions were placed and scanned in a water bottle with a diameter of 90 mm **(a)**. The measurements were performed with a FLASH sequence. The cancellations due to the aluminum screws are visible almost across the whole bottle with different intensity. The cancellations due to the titanium screws in comparison are of much smaller size, about one third. The reason therefor are the different susceptibilities, even though both materials are paramagnetic. The susceptibility of aluminum is $2.1 \cdot 10^{-5}$ and of titanium $1.8 \cdot 10^{-4}$ at room temperature [84]. Thus, depending on the material investigated the frequency range has to be adapted.

5.4.4 In Vivo Acqusitions

The combined techniques of ZOOM, MAVRIC and VAT were probed with single-shot STEAM and FSE in vivo at healthy volunteers, before applying them at volunteers with implants, to check their basic performance.
In figure 5.17 these measurements are presented. The resolution used was 1.0x1.0 mm^2 with a FOV of 40x128 mm^2. For the sagittal acquisitions 10 slices were measured with a thickness of 2 mm. 20 transversal slices were measured with a thickness of 4 mm. The 180° ZOOM pulse angle was 15° and a thickness factor of 70% was applied. The single-shot STEAM alpha excitations were performed with an angle of 10° and a thickness factor of 30%, as else folding artifacts were observed during measurements at phantoms and in vivo. The repetition time to acquire one frequency of a single slice with FSE was 900 ms and for the single-shot STEAM acquisitions 320 ms and 250 ms, respectively for 180° ZOOM and alpha. The echo spacing TE2 was 7.4 ms, 6.7 ms and 4.7 ms, respectively. This lead to a total measurement time for standard acquisitions without MAVRIC of 9 s, 3.2 s and 2.5 s for sagittal and 18 s, 6.4 s and 5 s for transversal measurements. For the measurements with VAT and MAVRIC a frequency range of 5 kHz to -5 kHz with an increment of 1 kHz was probed. This was done, even though no frequency shifts occur in a healthy volunteer, to test the general performance of MAVRIC in vivo and to probe if anything could influence the frequency selective acquisitions and the calculated images, as e.g. tissues with different resonance frequencies. Thus, the total measurement times were prolonged by a factor 11.
In the standard acquisitions without MAVRIC and VAT (see figure 5.17) it can be observed that the signal obtained is decreased in comparison to previous presented single-shot STEAM and FSE acquisitions. This is because no averaging was performed and the slice

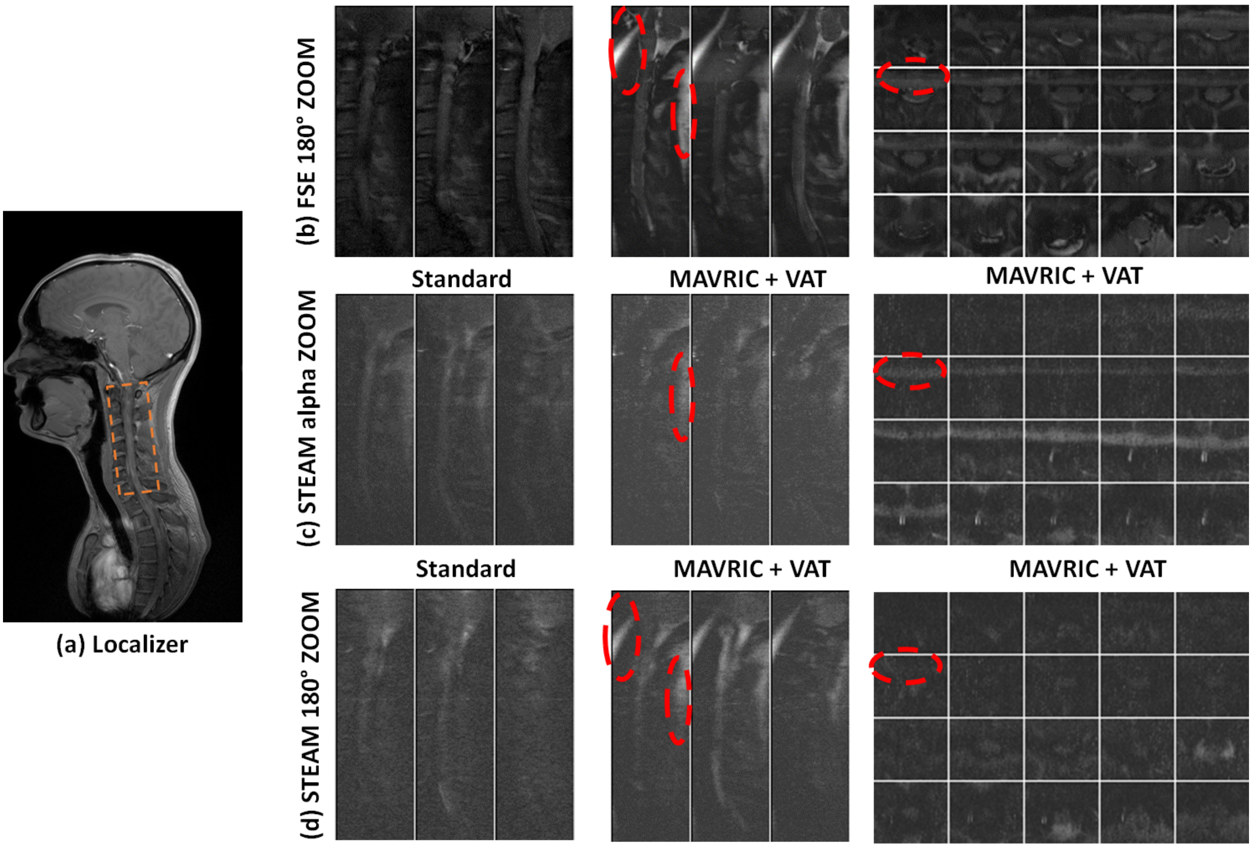

Figure 5.17: A FLASH localization measurement with the measured stack highlighted with orange dashed line **(a)**. In vivo measurements acquired with FSE 180° ZOOM **(b)**, single-shot STEAM alpha ZOOM **(c)** and single-shot STEAM 180° ZOOM **(d)** from top to bottom. From left to right the measurements are divided in: 5 out of 10 Sagittal slices with a thickness of 2 mm acquired with standard parameters, 5 out of 10 sagittal acquisitions with a thickness of 2 mm measured with MAVRIC and VAT and 20 transversal slices with a thickness of 4 mm, also acquired with MAVRIC and VAT. The frequency limits used with MAVRIC were 5 kHz and -5 kHz. They were scanned with an increment of 1 kHz. A few artifacts which occur during the MAVRIC and VAT acquisitions, are highlighted by red dotted circles.

thickness was decreased from 4 mm to 2 mm which reduces the total signal obtained.
For the standard acquisitions without MAVRIC and VAT in figure 5.17 the FSE images look the best compared to the images acquired with the single-shot STEAM techniques. The spinal cord can be clearly distinguished from other tissue structures, where as in the single-shot STEAM acquisitions it is complicated to distinguish. The difference occurs due to the general SNR difference of single-shot STEAM and FSE acquisitions, because of the acquisition of stimulated echoes and spin echoes, respectively, as mentioned before. The spinal cord is nearly not visible in the 180° ZOOM single-shot STEAM acquisitions. In

case of the alpha single-shot STEAM acquisitions the spinal cord can at least be recognized. This can be explained with the decreased alpha excitation bandwidth. It leads on the one hand to a slightly reduced measurement time and on the other hand the read-out bandwidth is increased.
By adding MAVRIC and VAT to the inner FOV acquisitions in comparison the signal is slightly increased, due to the repetitive acquisition of the slices and due to the calculation of the maximum intensity projection. However, in contrast to the standard acquisitions in the 180° ZOOM single-shot STEAM images the spinal cord can recognized and in the images acquired with alpha ZOOM excitations it is nearly not visible, neither in the sagittal acquisitions nor the transversal images. Due to the increased bandwidth during the frequency selective measurements with equal increment saturation effects can occur which saturate the following frequency band measured. Thus, the signal decreases in the images acquired with rotated alpha excitations.
The FSE acquisitions show still the best SNR ($\sim +30\%$) in comparison to the STEAM acquisitions and the spinal cord can be depicted in most images. However, in all acquisitions measured with MAVRIC and VAT independent of sagittal, transversal, FSE or STEAM artifacts occur[1], that can not be observed with the standard acquisitions.
They occur due to the frequency selective acquisitions. The spectral excitations are not spatially selective and thus all tissues which have a resonance frequency within the spectral range, get excited even though they are not in the FOV. The excited tissues, e.g. fat, have different precession frequencies and due to the chemical shift they get excited by the spatial selective refocusing and α excitations. The resulting spin echo which occurs outside of the measured slice or FOV is then further frequency encoded by the read out gradient and thus is measured with the receive coils. Thus, the obtained signal folds into the FOV measured even though cross sectional excitations are used.
The folding can be suppressed by choosing different rotation angles for ZOOM to not excite the regions which get folded into the FOV. This, however, would be needed to be done on the fly for each patient individually, depending on the tissue structures. To exclude the possibility that any signal outside of the FOV could lead to artifacts in the images saturation pulses were added. They are applied before the first 90° excitation in the region neighboring the FOV to saturate the spins the spins can not get excited by the 90° pulse and thus do not contribute to the measured signal.
The performance of the combined final sequence was again probed at a volunteer without

[1]Highlighted for selected images by red dotted circles.

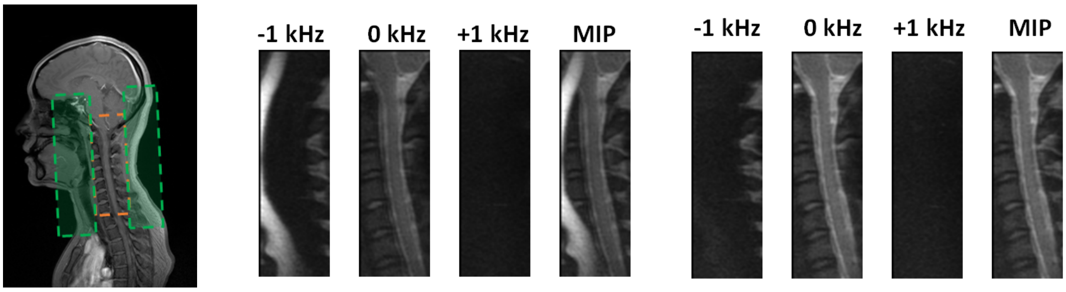

(a) **Localizer** (b) **Without saturation pulses** (c) **With saturation pulses**

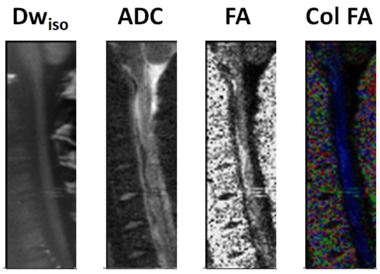

(d) **DWI with saturation pulses**

Figure 5.18: FLASH Localizer of investigated volunteer with measured stack highlighted in orange and saturation regions in green. Frequency selective ZOOM FSE acquisitions FSE single slice acquisitions with **(b)** and without **(c)** saturation pulses in a frequency range of of -3 kHz to +3 kHz with 1 kHz increment steps. The first three images are single frequency selective acquisitions between -1 kHz and 1 kHz, the fourth is a calculated maximum intensity projection of all frequency selective images. **(d)** single slice DWI images – DW_{iso}, ADC, FA and color-coded FA (l.t.r) – acquired with saturation pulses, ZOOM, MAVRIC in range of -3 kHz to +3 kHz with 1 kHz increment steps, VAT and four repetition measurements.

a metallic object implanted and compared to acquisitions without saturation pulses which are illustrated in 5.18 **(b,c)**. Further DWI, VAT, MAVRIC, ZOOM and saturation pulses combined with single-shot STEAM and FSE were probed, off which the latter is presented in 5.18 **(d)**.

For the comparison of with and without saturation pulses, FSE single slice acquisitions with VAT, MAVRIC and ZOOM were acquired in a frequency range of of -3 kHz to +3 kHz with 1 kHz increment steps. The measurement parameters used are nearly equal to the ones used for the FSE acquisitions shown in figure 5.17. The only difference is that a slice thickness of 4 mm was measured. Due to the increased slice thickness, as well as the decreased number of frequencies scanned an increased signal is obtained in comparison to the images in 5.17.

The frequency selective acquisitions between -1 kHz and 1 kHz are shown in **(b,c)** as well

as the maximum intensity projection which were calculated. In the measurements without saturation pulses **(b)** artifacts are clearly visible in the frequency selective acquisition of -1 kHz and in the calculated maximum intensity projection (MIP). The artifact superimposes the spinal cord in the maximum intensity projection.
The addition of two saturation pulses in **(c)**, as sketched by green rectangles in **(a)**, suppresses the artifacts in the -1 kHz frequency selective acquisition. As result in the maximum intensity projection the spinal cord can be clearly depicted without any superimposing signal or cancellations. This shows that the addition of saturation pulses further enhances the performance of MAVRIC in combination with ZOOM.
For a single slice DWI was performed with a b value of $500\,\mathrm{s\,mm^{-2}}$ and six weighted directions and one without weighting. The frequency selective acquisitions were performed between -2 kHz and 2 kHz with an increment of 1 kHz. Further 4 repetition measurements were performed. This results, with a repetition time for a single frequency selective acquisition of 900 ms for a single slice, in a total measurement time of 21.1 min.
The in **(d)** presented $\mathrm{DW_{iso}}$, ADC, FA and color-coded FA all show a good resolution. The spinal cord can be clearly recognized as well as its diffusivity. If compared to prior diffusion weighted images shown in this work at different volunteers no negative effects due to frequency selective measurement, VAT or the saturation pulses can be observed. However, the most apparent issue is that it is a time intensitiv approach. Compared to in the previous section, e.g. 5.2.2, performed measurements nearly double the time is needed, with less repetitive acquisitions and less slices measured.

5.4.5 In Vivo Near Metallic Objects

After finalizing the acquisition methods, by adding saturation pulses, single slice acquisitions were performed at a volunteer with an implant combination of titanium screws, bars and plates from the thorax downwards to the hips. The results are presented in figure 5.19. A resolution of $1.0\mathrm{x}1.0\mathrm{x}4.0\,\mathrm{mm^3}$ and a FOV of $40\mathrm{x}128\,\mathrm{mm^2}$ are used.
The single slice measurements were performed to obtain an overview and a comparison of the sequence interactions with metallic implants in vivo. In the ZOOM EPI acquisitions only a small part of the spinal cord is visible at the top, followed by strong distortions and complete cancellations there after. These observation are similar as in the 2DRF EPI measurements performed in previous sections in vivo.
The single-shot STEAM alpha acquisitions were performed without MAVRIC, as the phantom and in vivo measurements showed that in combination with MAVRIC it suffers

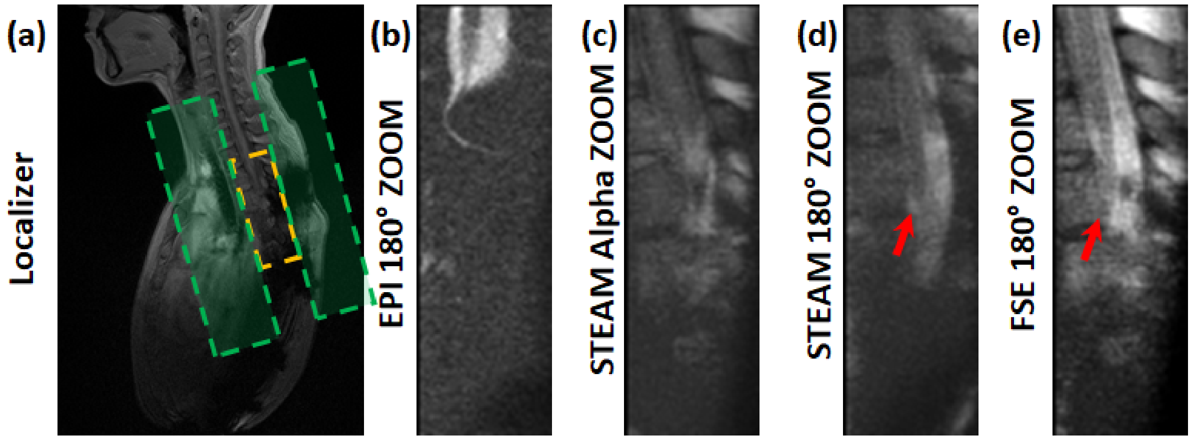

Figure 5.19: (a) FLASH localizer image of volunteer with metallic implants, measured region highlighted by dashed yellow lines and saturation pulses in green. Following sagittal single slice acquisitions with a resolution of 1.0x1.0x4.0 mm^3 surrounded by saturation pulses are presented: EPI ZOOM **(b)**, STEAM alpha ZOOM **(c)**, STEAM 180° **(d)** and FSE 180° **(e)**. The last two images are maximum intensity acquisitions calculated from frequency selective measurements which were scanned with an increment of 500 Hz in a range from 4 kHz to -4 kHz. Red arrows visualize the beginning of the cancellations in the MAVRIC acquisitions

in comparison to the STEAM 180° acquisitions. The reason therefor is the decreased excitation duration, the increased RF pulse bandwidth and the slice selection gradient, in comparison to the refocusing pulse and the 2nd 90° pulse[2] In the single shot STEAM alpha images the outline of the spinal cord can be recognized. However, the signal is very weak and it can not be distinguished between white and gray matter. Additionally from the middle downwards cancellations similar to the EPI measurements can be observed.
To determine the MAVRIC frequency limits the frequencies were scanned with an increment of 2 kHz between -10 kHz and 10 kHz to get a rough estimate of the extent of frequency displacements. As a consequent of these the single-shot STEAM and FSE 180° ZOOM maximum intensity projections presented were obtained with MAVRIC and calculated from 17 frequency selective measurements in a range of 4 kHz to -4 kHz with a sweep rate of 500 Hz in an interleaved manner as outside of this frequency range no significant signal contributions were be observed. In total the sagittal FSE 180° ZOOM acquisition combined with MAVRIC, VAT and saturation pulses shows the most reasonable image quality. The single-shot STEAM images lack SNR (~24%) in comparison to the FSE

[2]For the sake of completeness it should be noted that a possibility to improve the performance of single-shot STEAM alpha would be to adapt the excitation duration and thus reduce the bandwidth and adapt the slice selection gradients. Phantom measurements, however, showed that compared to the 180° ZOOM approach the SNR (~ 6%) was slightly decreased and thus was not considered further.

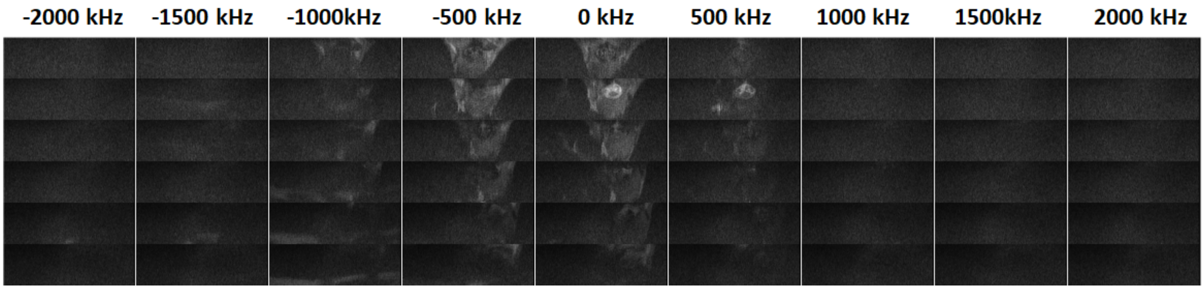

Figure 5.20: Frequency selective acquisitions of six slices measured in a volunteer with metallic implants. The frequency range covered was between 2 kHz and -2 kHz (l.t.r). The frequencies were measured in an interleaved manner, to prevent saturation effects, thus in between each acquisition the distance distance was at least 1 kHz which results in an increment of 500 Hz. Out of these selective measurements the slices in the 4th column in figure 5.21 are calculated

measurements and thus parts of the cord structure can not be identified.

In both acquisitions the spinal cord can be distinguished in the upper region. From the middle region downwards, however, cancellations can be observed. Near the red arrows the shape of the spinal cord narrows down as the spinal cord is not within the slice anymore. The cancellations, however, are not due to the metallic implants but due the shape of the spinal cord, which has a strong curvature in the direction of the image plane. This was first indicated by the uniform narrowing of the spinal cord and was latter confirmed with a rough transversal overview scan.

This gives rise to an additional problem which has to be kept in mind during the measurements, the shape of the investigated tissue, e.g. spinal cord. It could be insufficient to measure only a small number of sagittal slices. It might prove more useful to use acquisitions with either coronal or transversal orientation. This, however, could elongate the total measurement time to acquire the same imaging region.

An additional observation which is made during these measurement is that the frequency range used can be reduced even further, as no significant signal contribution can be observed in the outer ranges. This was confirmed in a second investigation of the volunteer where the frequency range was adapted to 2 kHz to -2 kHz and it was scanned with an increment of 500 Hz, resulting in nine frequency selective measurements for a single slice. The frequency selective acquisitions of six slices are presented in figure 5.20.

The frequencies are scanned in an interleaved manner so that the frequency difference between consecutive frequency acquisition is at least 1 kHz as the bandwidth of the RF excitations was 1 kHz and else saturation effects, due to pre-excitation of frequencies, could

occur. Due to the reduced increment the frequencies are scanned in the optimal case twice which decreases the distortions, as shown in the previous sections at phantoms. This was only utilized yet, as for the prior used larger frequency limits the total measurement time would be to long.
In the frequency selective acquisition it is observable that between 1 and -1 kHz the most signal is present and parts of the spinal cord can be distinguished. In the surrounding frequencies no signal is measured or only with a very low intensity. Thus, it could be assumed that it is possible to reduce the frequency ranges even further, however, this would pose the risk of frequency saturation, as during the measurements the frequencies are measured in an incremental manner and thus it is possible to scan the frequencies twice without saturation effects. If now the time in-between the measurements is to short the frequencies could still be not fully relaxed and less signal would be obtained if they get excited again. This probably would also only occur for a few selective frequencies and thus the calculated signal would be falsified. A possible solution is to not scan the frequencies twice in one acquisition. To, however, not lose any signal the increment and the bandwidth of the RF excitations need to be exactly the same and it has to be ensured that no gap between the spectral lines occurs as this might result in frequency saturation effects.
Further it always has to be kept in mind that the range in which the frequencies are distorted varies for each volunteer and or each metallic object implanted, as observed in previous acquisitions. In figure 5.21 the for the time being best result obtained with FSE is compared to the gold standard EPI used in volunteers without implants.
A resolution of 1.0x1.0 mm^2 and a FOV of 40x128 mm^2 was used with an oversampling of 60% and two saturation pulses surrounding the measured stack, as highlighted in green. The resolution was probed prior to the acquisition of the here shown image. For a resolution of 2.0x2.0 mm^2 the signal drops and the spinal cord is not recognizable anymore even though, the measurement time is reduced.
For ZOOM the first 180° pulse was rotated with an angle of 15° and a thickness factor of 70% which results in an effective FOV of about 40 mm with a transition zone of about 15 mm. Additionally, for the measurements Half-Fourier sampling was used, thus per slice 39 k-space lines were read out. The RF pulses used had a duration of 2560 μs with a bandwidth of about 1 kHz.
The echo spacing TE1 in between each measured line was 7.4 ms and the echo time TE2 needed for the diffusion module was 36 ms. Thus, for one frequency selectively acquisition the repetition time TR was 900 ms. In total 30 slices with a thickness of 4 mm were

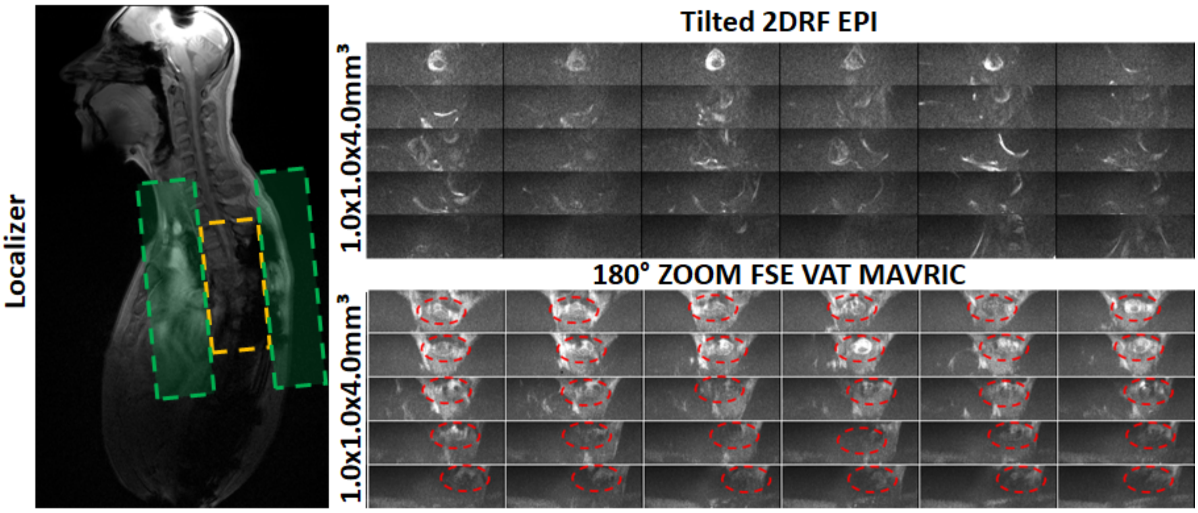

Figure 5.21: first a FLASH image of a volunteer in possession of metallic implants is presented. The measured stack is highlighted in yellow. The areas stimulated by saturation pulses are displayed with green squares. In the top image a tilted 2DRF EPI acquisition of 30 slices is presented. Beneath maximum intensity projections of a 180° ZOOM FSE VAT MAVRIC acquisition of 30 slices is presented with the spinal cord highlighted by red dotted circles. The frequency limits were 2 kHz and -2 kHz and were sweeped nine times in an interleaved manner with an increment of 500 Hz.

measured in a frequency range of 2 kHz to -2 kHz with an increment of 500 Hz. This resulted in a total measurement time of 4.03 min for the FSE acquisition.

The presented tilted 2DRF EPI was performed with an equal resolution. The echo time TE was 65 ms and a repetition time of 3900 ms was used. Thus, the total measurement time for 30 slices without averaging was 3.9 ms.

It can be observed that the EPI acquisitions show a reasonable image quality in the upper areas of the spinal cord, however, from the 4th slice downwards they suffer strongly from distortions. Still some signal is acquired in these slices but it is strongly displaced and distorted.

The maximum peak intensity acquisitions show in every slice signal of the spinal cord, as highlighted by the red dotted circles. In the first 3 slices the performance of EPI is much better compared to the FSE, however, the latter gains effectiveness in the lower areas. The measurements additionally show a much better image quality compared to the sagittal acquisitions shown in figure 5.19. In the images nearly no folding artifacts or distortions are visible, the spinal cord shows a reasonable form in nearly all slices. Only in the areas where the amount of metallic implants increases even further, the signal intensity decreases. A solution therefor would probably be given by repetitive measurement and thus enabling the averaging of the maximum intensity measurements.

5.5 Discussion

The performance and robustness of sequences near metallic artifacts and how they can be enhanced, are investigated in this study.
For this purpose the gold standard technique for diffusion weighted imaging, 2DRF EPI, which is discussed and investigated in the previous chapter, was first probed and latter used for comparison. The acquisitions show a large amount of distortions and cancellations near metallic artifacts. The reason therefor are the gradient refocused echoes. The blipped gradients are all influenced differently and the distortion affecting them accumulates through the read out train as they are not re-winded. This results in the signal displacements and cancellations observed.
Thus, in this work RF refocused sequences were used, to be precise single-shot STEAM and FSE. They are used as the spin echoes are refocused with RF pulses. As the main region of interest in the study was the spinal cord the sequences were combined with inner FOV techniques based on 2DRF excitations [18, 33] and cross-sectional excitations (ZOOM) [87], as done in the previous chapter at EPI. Further Half-Fourier-sampling was used to reduce the number of k-space lines and to accelerate the acquisition time. The possibility of SMS acceleration is given as well, however, it was not applied yet during the measurements.
The FSE and STEAM acquisitions combined with 2DRF excitations were probed at volunteers with implants and showed disillusioning results. The signal gain visible is marginal, compared to the EPI 2DRF acquisitions. It is found in this work that the 2DRF excitations are strongly influenced by metallic artifacts. One possible explanation therefor is that the rapid gradient switching induces an electromagnetic field into the metallic object which as a results becomes an antenna that creates an electromagnetic field. Another reason could be that the encoding gradients used to create a 2DRF excitation are influenced by magnetic inhomogeinities. The field inhomogeinities can lead to an additional precession and resulting the tilted lines, needed for the 2DRF excitations, cancel each other out. One consequence could be that the shape of the inner FOV is squeezed and or bent and does not excite in e.g. a square shape. Another result would be that the location of the side excitations are displaced as well and thus saturation effects and or folding artifacts occur in the images which lead to additional cancellations and distortions. Inner FOV techniques, however, are a strong tool to image small areas like the spinal cord,

as shown in the previous chapter. Thus, ZOOM inner FOV was combined with FSE and single-shot STEAM at the 180° DWI pulses and for the latter also with alpha pulses for the echo read out. The combinations showed reasonable results with less distortions than the 2DRF excitations. The reason therefor is that the slice selective gradients are of the same value and thus they experience the same frequency offsets induced by the artifacts. By manipulating the thickness of the rotated pulse, widening or thinning, the excited width can be increased and thus the distortions, do not interfere in the measured FOV. This is limited by the next slice to be measured in the stack, which is in this work twice the slice thickness as the measurements of the slices were performed in an interleaved manner. It is possible to increase the limits by increasing the gap in between the slices, or by using a multi-fold interleaved approach in which more than just one slice is skipped, depending on the slice stack.
In case of single-shot STEAM with the alpha pulse rotated for ZOOM the most signal was obtained near metallic objects compared to the 180° ZOOM approaches. Due to the larger bandwidth a wider frequency range can be measured and thus frequencies which are displaced stronger can still be obtained.
However, as still large cancellations were visible in the acquisitions, FSE and single-shot STEAM were combined with VAT [13] and MAVRIC [44] to obtain more signal and further to keep the possibility to perform DWI.
The application of VAT only showed a slight decrease of distortions. One reason therefor is that due to the additional VAT gradient small blurring artifacts can occur, as the signal is not obtained with a uniform read-out gradient but a tilted one. A different one is that with VAT only in-plane distortions are countered and strong distortions can shift the signal out of the plane so that VAT can not correct them.
The metallic artifacts displace the resonant frequencies not only in-plane but also in slice direction. To still acquire those frequencies and assign them the correct spatial location the approach of MAVRIC was chosen. MAVRIC measures the frequencies of a slice selectively in a specific range with a specific increment. For a slice stack thus the frequencies of a single slice were scanned first, before it was continued with the next. It is possible to loop first over the slices, while measuring the same frequency for each slice or cycling over them and vary the frequency for each slices in an ordered manner. This, however, poses the risk of frequency saturation effects and signal drop outs. Further the order in which the slices as well as the frequencies are measured, would have to be considered and adjusted for each measurement.
Depending on the frequency range and the frequency increment used during the MAVRIC

acquisition significant signal gain can be achieved. However, in in-plane direction still signal distortion can be observed. Thus, MAVRIC was further combined with VAT. VAT corrects the in-plane distortions and as a result in phantom measurements nearly the full signal can be obtained, independent of the amount of metallic artifacts or the sequence used.
The investigations of ZOOM, MAVRIC and VAT combined with either single-shot STEAM or FSE showed reasonable results at phantoms, but in vivo they were disappointing. This was due to folding artifacts which occurred during MAVRIC measurements even though ZOOM was utilized. The explanation for the artifacts are that with the spectral excitations the whole body and thus additional tissues, e.g. fat, are excited. Thus, they can also be excited by the ZOOM excitations, only at different locations due to the different resonance frequencies. However, the frequency selective read out measures the signal which then folds into the image and leads to artifacts. To solve this problem saturation pulses surrounding the measured slices were utilized in this work, to pre saturate tissues and ares which could lead to folding artifacts. Another possibility would be to apply the rotated pulses from a different direction[3] and thus avoid tissue structures which can be folded. This approach, however, would be needed to be performed individually on the fly depending on the volunteer investigated.
The in vivo and phantom measurements show that the SNR of single-shot STEAM in combination with ZOOM is lower compared to FSE combined with ZOOM ($\sim 27\%$). The reasons therefor are the reduced flip angle, used for the read out, and that only stimulated echoes are measured during STEAM. An observation that was made is that the STEAM alpha ZOOM approach does not combine well with MAVRIC. The reason there for is the changed RF pulse duration, as resulting also the slice selective gradient differs in strength compared to the other pulses, e.g. 180° or second 90°. Thus, the RF excitation is influenced differently by the metallic artifacts. Another reason for the disappointing performance of STEAM alpha combined with MAVRIC are saturation effects due to the increased bandwidth. Due to the increased bandwidth neighboring frequencies get saturated and can not relax back prior to be measured. These effects can be countered by adjusting the duration, however, compared to the 180° ZOOM approach the SNR is slightly decreased ($\sim 5\%$) no additional gain was observed. The single-shot STEAM alpha, without MAVRIC, combined with VAT, however, can give a good overview in the region of interest, the tissue structures and the cancellations, due to its wide bandwidth. Further

[3] In our case of 15° e.g. 165°

the duration of a single-shot STEAM alpha acquisition is rather short in comparison to FSE or single-shot STEAM combined with 180° ZOOM and probably the signal intensity can be increased by averaging over multiple acquisitions.

180° ZOOM single-shot STEAM does not show the same signal range without MAVRIC, as the read-out pulse bandwidth was only 1 kHz wide in comparison to the single-shot STEAM alpha acquisitions. On the other hand in combination with MAVRIC significantly more signal can be obtained. The reason is that all slice selective gradients are of the same value and thus the metallic artifacts equally influence them, as already mentioned. The SNR, however, lacks in comparison to the FSE acquisitions ($\sim 27\%$), thus during the last in vivo measurements it was not investigated further. The measurement time, however, was in this study only one third of the time needed for the FSE acquisitions. It could be possible that the SNR efficiency is higher and thus it might be possible to achieve a similar SNR in an equal amount of time by repetitive acquisitions and averaging. This needs additional investigations at volunteers with implants for validation, as the effect of varying magnetic susceptibilities, due to tissue structures and implants, can not be simulated perfectly at phantoms.

This addresses one of the main issues, which was present during the study. The implants and tissue structures, as well as their interaction with each other and the external fields, varied for each measurement. As a result the magnetic distortions influencing the frequencies and the sequences changed. This was observed in the investigation presented in figure 5.9 and 5.10. The same measurements were performed at both volunteers and the results differ strongly. In this case the difference were found in the implants which led to either weak or strong frequency displacement. The extent to which the frequency is influenced can not easily be determined, as several factors come into play. The material used for the implants, more specifically, their susceptibility, is a large factor. This can be recognized at FLASH acquisitions of an aluminum screw, used for the phantom measurements, and a titanium screw presented in figure 5.16. Titanium is widely used for implants, however, there are also implants made out of e.g. Cobalt-Chromium alloy, which differ again in susceptibility. Further the geometry in which the implants are arranged, e.g. six screws with bars, 12 screws with plates and so on, has an additional impact on the measured frequencies. The metallic implants interact with each other, by for example Hall effects [31, 37] which are induced by rapid switching fields, due to which the observed cancellations and or displacements differ. Additionally implants which are on paper the same, can differ due to the different tissue structures of each person. These variations complicate the comparisons in-between various volunteers. Thus, in this study we tried to investigate mostly volunteers with metallic implants that induced strong artifacts, as they seemed to emit the most complicated interference's and thus we the developed measurement would be insensitive to the different properties.

In phantom and in vivo measurements at metallic artifacts the FSE combined with inner FOV ZOOM, MAVRIC, VAT and saturation pulses showed the best results. Near metal significantly more signal is obtained compared to EPI and STEAM acquisitions. It might even be possible to enhance the signal even further with quadratic phase modulation [73], where the phase is modulated to ensure that the new echoes always overlap with stimulated echoes of previous line acquisitions. The duration of the FSE in comparison to the other sequences, however, is significantly higher.

Technically it would be possible to reduce the duration to about the duration of the STEAM 180° acquisitions. The problem is that due to the repetitive usage of 180° pulses the energy deposition could lead to heating effects in the subject. To negate this effect the timing in-between the frequency selective acquisitions is prolonged. The energy can be further reduced by decreasing the amount of slices and or the selective frequencies measurements which, however, is not always possible. Additionally it would be optimal to perform repetitive measurements, to be able to average the images and thus increase the SNR. However, this again would increase the measurement duration and the energy deposition.

Further it would be desirable for the application of diffusion weighted imaging to measure at least six non-collinear direction would be desirable. This was probed at phantoms and and in vivo at healthy volunteers and showed results with good image quality and increased SNR. However, DWI led to excessively long measurement times and would once again lead to a extension of the repetition time. For example the single slice diffusion weighted acquisition with 4 repetitions which as perdormed in this study, took 21 min. If the final acquisitions at the volunteer with metallic implants would have been performed with diffusion-weighting ∼28 min would have been needed. This is no feasible approach to apply at patients, as in addition to the high duration it can not be ensured that the correct region or the right frequency range is measured. This is also the reason due to which the last measurement were not performed in combination with diffusion weighting. To enable this work, the possibility to accelerate the FSE without stressing the SAR even further, has to be investigated.

One possibility might be the combination of MAVRIC with simultaneous multi-slice [8, 77] as similarly performed in the previous chapter. The frequency selective pulse thereby does not have to be a simultaneous multi slice pulse as all tissues with the right frequency are excited in the whole body. Further no additional influence on the SMS pulses by the magnetic inhomogeinities, compared to single slice pulses, is expected. Thus, it can be assumed that the measurement time decreases significantly. This, however, has yet to be investigated.

A different approach could be to adjust the duration of the RF pulses and the remaining slice selective gradients, to increase the bandwidth of the RF pulses and thus reduce the amount of frequency selective measurements similar to the approach during STEAM alpha. The problem is that if the duration is too short the pulse envelope and the excitation suffers.

To conclude this chapter, the techniques which we combined and investigated provide a feasible resolution near metallic implants. However, work has to be done in hindsight of the measurement time to make them applicable in clinical surrounding.

Chapter 6

Conclusion and Prospects

In this thesis different imaging techniques were developed and researched to increase the robustness and at the same time decrease the acquisition time of MRI sequences.
In the first part, diffusion weighted echo planar imaging was combined with inner field-of-view techniques –cross sectional excitations and 2DRF excitations–. In addition the measurement duration was accelerated by utilizing simultaneous multi slice acquisition. The influence of small inhomogeneities and the interaction of SMS with the various possibilities to arrange the inner FOV techniques were investigated at phantoms and in vivo. It was found that with SMS the orthogonal ZOOM and 2DRF collinear approach can be improved. However, the influence of inhomogeinities is still rather strong, which leads to more distortions compared to acquisitions with ZOOM with the 180° diffusion-weighted pulse rotated or tilted 2DRF excitations. In direct comparison tilted 2DRF excitations showed slightly more signal than 180° ZOOM. Further the regions outside of the small FOV do not have to be considered in case of the 2DRF excitations.
This makes the combination of tilted 2DRF excitations and SMS a feasible approach for investigations of the tissue structure and the neural system, for research as well as clinical investigation. The combination is a fast and simple system to execute with a high SNR efficiency.

In the second part of the thesis the diffusion-weighted 2DRF inner FOV EPI was probed at metallic artifacts which led to images with large cancellations and strong distortions due to strong field inhomogeinities and their effect on RF excitations.
Thus, the performance of RF refocused sequences –STEAM and FSE– near implants was examined. In combination with 2DRF excitations the sequences suffered in the vicinity of metallic artifacts similar to the EPI acquisitions and no significant signal gain could be observed. Thus, the sequences were combined with ZOOM and probed at phantoms.

These measurement showed promising results in comparison to the 2DRF excitations. However, the acquisitions still did not provide satisfying results as the metallic artifacts still led to significant cancellations.
To further improve the sequences, we adapted and combined them with view angle tilt and multi acquisition variable-resonance image combination. The first investigations at phantoms showed that with the combination of MAVRIC and VAT, with either FSE or STEAM, good results can be obtained. Further alpha ZOOM STEAM showed good results even with out MAVRIC only with VAT, due to the higher excitation bandwidth and the resulting higher frequency coverage.
The first measurements performed at healthy volunteers, however, were not satisfying. The reason therefor was the folding of different tissue structures which were stimulated by the combination of ZOOM and frequency selective excitations needed for MAVRIC. This effect was countered in this work by saturation pulses surrounding the measured stack. This, however, could pose the risk of signal cancellation, as the metallic artifacts can influence the pulses as well. In the following in vivo measurement though, this was not observed and it was possible to obtain images with reasonable quality by calculating the maximum intensity projections of the frequency selective acquisitions.
The STEAM acquisitions suffered from a low SNR in comparison to the FSE acquisitions ($\sim$27%), due to the small flip angles. This can probably be countered by averaging over multiple measurements, which was not investigated so far in vivo, however, showed first good results at phantom measurements.
The final FSE acquisitions which are presented in this work showed that they can resolve nearly the complete spinal cord near metallic implants with the help of MAVRIC and VAT. The downside of the FSE approach is the long measurement time, which makes it nearly impossible to apply diffusion weighted imaging, as the measurement time would increase beyond the scope of feasible applications in vivo. First diffusion weighted ZOOM FSE with MAVRIC and VAT were performed at phantoms and in vivo and showed reasonable results, however besides the long measurement time, the SAR was again a hindrance and the total deposited energy was rather high.
We found that the difficulties which arise with the desire to acquire good images near metallic artifacts are diverse and increase with each new solution. First it were only the frequency offsets induced by the metallic artifacts. Next, it were the susceptibilities of the tissue in combination with the implants and then it were unexpected folding artifacts. In total, additionally to the improvement of the EPI DTI, significant steps for a feasible sequence near metallic artifacts were performed with the combination of ZOOM, VAT,

MAVRIC, FSE and saturation.

To even further improve the sequences and to make then also feasible for clinical studies, for STEAM investigations in hindsight of the SNR have to be performed. Besides the increase of repetitive measurements, changing the ZOOM pulse and or the pulse for the frequency selective excitations, e.g. the second 90° pulse, might prove to show significant increase in the SNR. Further it could be of use to adapt the bandwidth of the RF pulses and not measure a brought frequency but a slim and increase the frequency selective steps. The improvement which is most important for the FSE is the reduction of the SAR and the measurement time. Here increasing the pulse bandwidth could be a solution, to reduce the steps and thus the deposited energy. A different approach could be to combine SMS with MAVRIC, similar to the approach performed with 2DRF EPI. It would be possible to use a frequency selective pulse to stimulate the full slice stack and determine the signal with multi slice pulses. This could, however, backfire as for higher acceleration factors the deposited energy increases and thus the time gained by the acceleration could be in vain. The measurement near metallic artifacts could be improved by the thorough investigation of the interactions of differently combined implants, the influence of different susceptibilities and the behavior near different tissue structures. Most investigations are only performed at single metallic implants, e.g. screws, up till now and complicated structures are left out. Thus, the knowledge of the different behaviors and interaction could help to improve image acquisitions near metals significantly.

Bibliography

[1] Attenberger, Ulrike I. ; Runge, Val M. ; Stemmer, Alto ; Williams, Kenneth D. ; Naul, L. G. ; Michaely, Henrik J. ; Schoenberg, Stefan O. ; Reiser, Maximilian F. ; Wintersprenger, Bernd J.: Diffusion weighted imaging: a comprehensive evaluation of a fast spin echo DWI sequence with BLADE (PROPELLER) k-space sampling at 3 T, using a 32-channel head coil in acute brain ischemia. In: *Invest Radiol* 44 (2009), S. 656–661

[2] Barth, MArkus ; Breuer, Felix ; Koopmans, Peter J. ; Norris, David G. ; Poser, BEnedikt A. P.: Simultaneous multislice (SMS) imaging techniques. In: *magnetic resonance in medicine* 75 (2016), S. 63–81

[3] Basser, Peter J. ; Mattiello, James ; LeBiihan, Denis: MR Diffusion Tensor Sectroscopy and Imaging. In: *Biophysical Journal* 66 (1994), January, S. 259–267

[4] Belliveau, JW ; Kennedy, DN ; McKinstry, RC ; Buchbinder, BR ; Weisskoff, RM ; Cohen, MS ; Vevea, JM ; Brady, TJ ; Rosen, BR: Functional mapping of the human visual cortex by magnetic resonance imaging. In: *Science* 254 (1991), Nr. 5032, S. 716–719

[5] Bihan, Denis L.: Diffusion MRI past and future: an overview. In: *Siemens Healthineers* (2019)

[6] Bloch, Felix: Nuclear induction. In: *Physical review* 70 (1946), Nr. 7-8, S. 460

[7] Bottomley, Paul A. ; Hardy, Christopher J.: Two-dimensional spatially selective spin inversion and spin-echo refocusing with a single nuclear magnetic resonance pulse. In: *Journal of Applied Physics* 62 (1987), nov, Nr. 10, S. 4284–4290

[8] Breuer, Felix A. ; Blaimer, Martin ; Heidemann, Robin M. ; Mueller, Matthias F. ; Griswold, MAak A. ; Jakob, Peter M.: Controlled aliasing in parallel imaging results in higher acceleration (CAIPIRINHA) for multi-slice imaging. In: *Magnetic resonance in medicine* 53 (2005), S. 684–691

[9] Butts, Kim ; Pauly, John ; Gold, Garry: Reduction of blurring in view angle tilting MRI. In: *Magnetic resonance in medicine* 53 (2005), 02, S. 418–24

[10] Bydder, GM ; Pennock, JM ; Steiner, RE ; Khenia, S ; Payne, JA ; Young, IR.: The short TI inversion recovery sequence–an approach to MR imaging of the abdomen. In: *Magn Reson Imaging.* 3 (1985), S. 251–254

[11] Carr, H. Y. ; Purcell, E. M.: Effects of Diffusion on Free Precession in Nuclear Magnetic Resonance Experiments. In: *Physical Review* 94 (1954), Nr. 3, S. 630–643

[12] Carslaw, H.S. ; Publications, Dover (Hrsg.): *Introduction to the Theory of Fourier's Series and Integrals*. Macmillan and Company, limited, 1921 (Introduction to the Theory of Fourier's Series and Integrals)

[13] Cho, Z.H. ; Kim, D.J. ; Kim, Y. K.: Total inhomogeneity correction including chemical shifts and susceptibility by view angle tilting. In: *American Associattion of Physiciss in Medicine* 15 (1988), Nr. 7, S. 7–11

[14] Conolly, Steven ; Nishimura, Dwight ; Macovski, Albert ; Glover, Gary: Variable-rate selective excitation. In: *Journal of Magnetic Resonance (1969)* 78 (1988), Nr. 3, S. 440 – 458. – ISSN 0022–2364

[15] Dixon, W T.: Simple proton spectroscopic imaging. In: *Radiology* 153 (1984), Nr. 1, S. 189–194

[16] Feinberg, David A. ; Hoenninger, John C. ; Crooks, Lawrence E. ; Kaufman, Leon ; Watts, Jeffrey C. ; Arakawa, Mitsuaki: Inner volume MR imaging: technical concepts and their application. In: *Radiology* 156 (1985), S. 743–747

[17] Fick, Adolf: Ueber Diffusion. In: *Annalen der Physik* 170 (1855), Nr. 1, S. 59–87

[18] Finsterbusch, Jürgen: High-resolution diffusion tensor imaging with inner field-of-view EPI. In: *Journal of magnetic resonance imaging* 29 (2009), S. 987–993

[19] Finsterbusch, Jürgen: Improving the performance of diffusion-weighted inner field-of-view echo-planar imaging based on 2D-selective radiofrequency excitations by tilting the excitation plane. In: *Journal of magnetic resonance imaging* 35 (2012), S. 984–992

[20] Finsterbusch, Jürgen: Functional neuroimaging of inner fields-of-view with 2D-selective RF excitations. In: *Magnetic Resonance Imaging* 31 (2013), sep, Nr. 7, S. 1228–1235

[21] Finsterbusch, Jürgen ; Frahm, Jens: Half-Fourier single-shot STEAM MRI. In: *Magnetic Resonance in Medicine* 47 (2002), S. 611–615

[22] Foyomed Medical Instruments Co., Ltd.: *Product catalogue.* www.nbmedicalinstruments.com/, August 2021

[23] Frahm, J. ; Merboldt, K.D. ; Hänicke, W. ; Haase, A.: Stimulated Echo Imaging. In: *Journal of Magnetic Resonance* 64 (1985), S. 81–93

[24] Gerabek, W.E. ; Haage, B.D. ; Keil, G. ; Wegner, W.: *Enzyklopädie Medizingeschichte.* De Gruyter, 2011. – ISBN 9783110976946

[25] Graham, Thomas: The Bakerian Lecture – On the Diffusion of Liquids. In: *Philosophical Transactions of the Royal Society of London* 27 (1829), S. 74–83

[26] Graham, Thomas: A short Account of Experimental Researches on the Diffusion of Gases through each other, and their Separation by mechanical means. In: *Quarterly Journal of Science, Literature and Art* 140 (1829), S. 1–46

[27] Graham, Thomas: On the Law of the Diffusion of Gasses. In: *Philosophical Magazine* 2 (1833), S. 175–190

[28] Griswold, Mark A. ; Jakob, Peter M. ; Heidemann, Robin M. ; Nittka, Mathias ; Jellus, Vladimir ; Wang, Jianmin ; Kiefer, Berhold ; Haase, Axel: Generalized autocalibrating partially parallel acquisitions (GRAPPA). In: *Magn Reson Med.* 47 (2002), Nr. 6, S. 1202–1210

[29] Guérin, Bastien ; Setsompop, Kawin ; Ye, Huihui ; Poser, Benedikt A. ; Stenger, Andrew V. ; Wald, Lawrence L.: Design of parallel transmission pulses for simultaneous multislice with explicit control for peak power and local specific absorption rate. In: *Magnetic Resonance in Medicine* 73 (2015), Nr. 5, S. 1946–1953

[30] Haase, A ; Frahm, J ; Matthaei, D ; Hanicke, W ; Merboldt, K.-D: FLASH imaging. Rapid NMR imaging using low flip-angle pulses. In: *Journal of Magnetic Resonance (1969)* 67 (1986), Nr. 2, S. 258 – 266. – ISSN 0022–2364

[31] Hall, E. H.: On a New Action of the Magnet on Electric Currents. In: *American Journal of Mathematics* 2 (1879), Nr. 3, S. 287–292. – ISSN 00029327, 10806377

[32] Hanson, Lars G.: Is quantum mechanics necessary for understanding magnetic resonance? In: *Concepts in Magnetic Resonance Part A* 32A (2008), Nr. 5, S. 329–340

[33] Hardy, Christopher J. ; Cline, Harvey E.: Spatial localization in two dimensions using NMR designer pulses. In: *Journal of Magnetic Resonance (1969)* 82 (1989), Nr. 3, S. 647 – 654. – ISSN 0022–2364

[34] Hargreaves, B. ; Worters, P. W. ; Pauly, Butts K. ; Koch, Kevin M. ; Gold, Garry E.: Metal Induced Artifacts in MRI. In: *AJR Am J Roentgenol* 197 (2011), Nr. 3, S. 547–555

[35] Hargreaves, Brian A. ; Worters, Pauline W. ; Pauly, Kim B. ; Pauly, John M. ; Koch, Kevin M. ; Gold, Garry E.: Metal-Induced Artifacts in MRI. In: *American Journal of Roentgenology* 197 (2011), sep, Nr. 3, S. 547–555

[36] Henning, J. ; Nauerth, A. ; Friedburg, H.: RARE Imaging: A fast imaging method for clinical MR. In: *Magnetic resonance in Medicine* 3 (1986), S. 823–833

[37] Hirsch, J. E.: Spin Hall Effect. In: *Physical Review Letters* 83 (1999), Aug, Nr. 9, S. 1834–1837. – ISSN 1079–7114

[38] Huettel, S.A. ; Song, A.W. ; McCarthy, G.: *Functional Magnetic Resonance Imaging*. Oxford University Press, Incorporated, 2009. – ISBN 9780878932863

[39] Jeong, Eun-Kee ; Kim, Seong-Eun ; Guo, Junyu ; Kholmovske, Eugene G. ; Parker, Dennis L.: High-Resolution DTI with 2D Interleaved Multislice Reduced FOV Single-Shot Diffusion-Weighted EPI (2D ss-rFOV-DWEPI). In: *Magnetic Resonance in Medicine* 54 (2005), S. 1575–1579

[40] Jones, Derek K. ; Basser, Peter J.: “Squashing peanuts and smashing pumpkins”: How noise distorts diffusion-weighted MR data. In: *Magnetic Resonance in Medicine* 52 (2004), Nr. 5, S. 979–993

[41] Keller, P J. ; Hunter, W W. ; Schmalbrock, P: Multisection fat-water imaging with chemical shift selective presaturation. In: *Radiology* 164 (1987), Nr. 2, S. 539–541

[42] Khalil, Ahmed A. ; Hohenhaus, Marc ; Kunze, Claudia ; Schmidt, Wolf ; Brunecker, Peter ; Villringer, Kersten ; Merboldt, Klaus-Dietmar ; Frahm, Jens ; Fiebach, Jochen B.: Sensitivity of Diffusion-Weighted STEAM MRI and EPI-DWI to Infratentorial Ischemic Stroke. In: *PLOS ONE* 11 (2016), 08, S. 1–13

[43] Kim, Seong-Gi ; Tsekos, Nikolaos V. ; Ashe, James: Multi-slice perfusion-based functional MRI using the FAIR technique: comparison of CBF and BOLD effects. In: *NMR in Biomedicine: An International Journal Devoted to the Development and Application of Magnetic Resonance In Vivo* 10 (1997), Nr. 4-5, S. 191–196

[44] Koch, K. M. ; Brau, A. C. ; Chen, W. ; Gold, G.E. ; Hargreaves, B-A ; Koff, M. ; McKinnon, G.C. ; Potter, H.G. ; King, K.F.: Imaging Near Metal with a MAVRIC-SEMAC Hybrid. In: *Magnetic Resonacne in Medicine* 65 (2011), S. 71–82

[45] Koch, Kevin M. ; Lorbiecki, John E. ; Hinks, R. S. ; King, Kevin F.: A multispectral three-dimensional acquisition technique for imaging near metal implants. In: *Magnetic Resonance in Medicine* 61 (2009), feb, Nr. 2, S. 381–390

[46] Koch, KM ; Hargreaves, BA ; Pauly, K B. ; Chen, W ; Gold, GE ; King, KF: Magnetic resonance imaging near metal implants. In: *Journal of magnetic resonance imaging : JMRI* 32 (2010), October, Nr. 4, S. 773—787. – ISSN 1053–1807

[47] Koopmans, Peter J. ; Boyacioğlu, Rasim ; Barth, Markus ; Norris, David G.: Simultaneous multislice inversion contrast imaging using power independent of the number of slices (PINS) and delays alternating with nutation for tailored excitation (DANTE) radio frequency pulses. In: *Magnetic Resonance in Medicine* 69 (2013), Nr. 6, S. 1670–1676

[48] Kwong, K. K. ; Belliveau, J. J. ; Goldberg, I. E. ; Weisskoff, R. M. ; Poncelet, B. P. ; Kennedy, D. N. ; Hoppel, B. E. ; Cohen, M. S. ; Turner, R.: Dynamic magnetic resonance imaging of human brain activity and during primary sensory stimulation. In: *Proceedings of the National Academy of Sciences of the United States of America* 89 (1992), Nr. 12, S. 5675–5679

[49] Lauterbur, P. C.: Image Formation by Induced Local Interactions: Examples Employing Nuclear Magnetic Resonance. In: *Nature* 242 (1973), Nr. 5394, S. 190–191. – ISSN 1476–4687

[50] Le Roux, Patrick: NON-CPMG Fast Spin Echo with Full Signal. In: *Journal of Magnetic Resonance* 155 (2002), S. 278–292

[51] Lee, Mi-Jung ; Kim, Sungjun ; Lee, Sung-Ah ; Song, Ho-Taek ; Huh, Yong-Min ; Kim, Dae-Hong ; Han, Seung ; Suh, Jin-suck: Overcoming Artifacts from Metallic Orthopedic Implants at High-Field-Strength MR Imaging and Multi-detector CT1. In: *Radiographics : a review publication of the Radiological Society of North America, Inc* 27 (2007), 05, S. 791–803

[52] Liang, Zhi-Pei ; Lauterbur, Paul C.: *Principles of magnetic resonance imaging: a signal processing perspective*. SPIE Optical Engineering Press, 2000

[53] Lu, Wenmiao ; Pauly, Kim B. ; Gold, Garry E. ; Pauly, John M. ; Hargreaves, Brian A.: SEMAC: Slice Encoding for Metal Artifact Correction in MRI. In: *Magnetic Resonance in Medicine* 62 (2009), S. 66–76

[54] Mansfield, P. ; Ordidge, R J. ; Coxon, R: Zonally magnified EPI in real time by NMR. In: *Journal of Physics E: Scientific Instruments* 21 (1988), S. 275–281

[55] Maudsley, A.A: Multiple-line-scanning spin density imaging. In: *Journal of Magnetic Resonance (1969)* 41 (1980), Nr. 1, S. 112 – 126. – ISSN 0022–2364

[56] McGibney, G. ; Smith, M. R. ; Nichols, S. T. ; Crawley, A.: Quantitative Evaluation of Several Partial Fourier Reconstruction Algorithms Used in MRI. In: *Magnetic Resonance in Medicine* 30 (1993), Juli, Nr. 1, S. 51–59

[57] Meiboom, Saul ; Gill, David: Modified spin-echo method for measuring nuclear relaxation times. In: *Review of scientific instruments* 29 (1958), Nr. 8, S. 688–691

[58] Merboldt, Klaus-Dietmar ; Hänicke, Wolfgang ; Frahm, Jens: Self-Diffusion NMR Imaging Using Stimulated Echos. In: *Journal of Magnetic Reonance* 64 (1985), April, S. 479–486

[59] Moseley, M E. ; Kucharczyk, J ; Mintorovitch, J ; Cohen, Y ; Kurhanewicz, J ; Derugin, N ; Asgari, H ; Norman, D: Diffusion-weighted MR imaging of acute stroke: correlation with T2-weighted and magnetic susceptibility-enhanced MR imaging in cats. In: *American Journal of Neuroradiology* 11 (1990), Nr. 3, S. 423–429

[60] Nolte, Ulrike G. ; Finsterbusch, Jürgen ; Frahm, Jens: Rapid Isotropic and Diffusion Mapping and Without Susceptibility and Artifacts: Whole and Brain

Studies and Using Diffusion-Weighted and Single-Shot STEAM and MR Imaging. In: *Magnetic Resonance in Medicine* 44 (2000), S. 731–736

[61] Norris, David G. ; Börnert, Peter ; Reese, Torsten ; Leibfritz, Dieter: On the Application of Ultra-fast RARE Experiments. In: *Magnetic Resonance in Medicine* 27 (1992), S. 142–164

[62] Nunes, Rita ; Hajnal, Joseph ; Golay, Xavier ; Larkman, D.J.: Simultaneous slice excitation and reconstruction for single shot EPI. In: *Proceedings of the 14th Annual Meeting of ISMRM* (2006), 01

[63] P., Mansfield: Multi-planar image formation using NMR spin echoes. In: *Solid State Physics* 10 (1977), S. L55–L58

[64] Pauly, John ; Nishimura, Dwight ; Macovski, Alber: A k-Space Analysis and of Small-Tip-Angle and Excitation. In: *Journal of Magnetic Resonance* 81 (1989), Nr. 43-56

[65] Poser, Benedikt A. ; Anderson, Robert J. ; Guérin, Bastien ; Setsompop, Kawin ; Deng, Weiran ; Mareyam, Azma ; Serano, Peter ; Wald, Lawrence L. ; Stenger, V. A.: Simultaneous multislice excitation by parallel transmission. In: *Magnetic Resonance in Medicine* 71 (2014), Nr. 4, S. 1416–1427

[66] Pruessmann, Klaas P. ; Weiger, Markus ; Scheidegger, Markus B. ; Boesiger, Peter: SENSE: sensitivity encoding for fast MRI. In: *Magnetic Resonance in Medicine: An Official Journal of the International Society for Magnetic Resonance in Medicine* 42 (1999), Nr. 5, S. 952–962

[67] Purcell, E. M. ; Torrey, H. C. ; Pound, R. V.: Resonance Absorption by Nuclear Magnetic Moments in a Solid. In: *Phys. Rev.* 69 (1946), Jan, S. 37–38

[68] Ra, J. B. ; Rim, C. Y.: Fast imaging using subencoding data sets from multiple detectors. In: *Magnetic Resonance in Medicine* 30 (1993)

[69] Rabi, I. I. ; Zacharias, J. R. ; Millman, S. ; Kusch, P.: A New Method of Measuring Nuclear Magnetic Moment. In: *Phys. Rev.* 53 (1938), Feb, S. 318–318

[70] Reiser, Maximilian ; Semmler, Wolfhard: *Magnetresonanztomographie*. Springer-Verlag, 2013

[71] Rieseberg, Susanne ; Frahm, Jens ; Finsterbusch, Jürgen: Two-dimensional spatially-selective RF excitation pulses in echo-planar imaging. In: *Magnetic Resonance in Medicine* 47 (2002), Nr. 6, S. 1186–1193

[72] Rooney, William D. ; Johnson, Glyn ; Li, Xin ; Cohen, Eric R. ; Kim, Seong-Gi ; Ugurbil, Kamil ; Springer Jr., Charles S.: Magnetic field and tissue dependencies of human brain longitudinal 1H2O relaxation in vivo. In: *Magnetic Resonance in Medicine* 57 (2007), Nr. 2, S. 308–318

[73] Roux, P. L. ; McKinnon, G. ; Yen, Y.-F. ; Fernandez, B.: Realignment capability of the nCPMG sequence. In: *Journal of Magnetic Resonance* 211 (2011), aug, Nr. 2, S. 121–133

[74] S, Kurtz ; K, Ong ; E, Lau ; F, Mowat ; M., Halpern: Projections of primary and revision hip and knee arthroplasty in the United States from 2005 to 2030. In: *J Bone Joint Surg Am.* 89 (2007), Nr. 4, S. 780–785

[75] Saritas, Emine U. ; Cunningham, Charles H. ; Lee, Hyung J. ; Han, Eric T. ; Nishimura, Dwight G.: DWI of the spinal cord with reduced FOV single-shot EPI. In: *Magnetic resonance in medicine* 60 (2008), S. 468–473

[76] Schenck, JF: The role of magnetic susceptibility in magnetic resonance imaging: MRI magnetic compatibility of the first and second kinds. In: *Medical physics* 23 (1996), June, Nr. 6, S. 815—850

[77] Setsompop, Kawin ; Gagoski, Borjan A. ; Polimeni, Jonathan R. ; Witzel, Thomas ; Wedeen, Van J. ; Wald, Lawrence L.: Blipped-controlled aliasing in parallel imaging for simultaneous multislice echo planar imaging with reduced g-factor penalty. In: *Magnetic Resonance in Medicine* 67 (2012), Nr. 5, S. 1210–1224

[78] Shaw, Peter J. ; Rawlins, David J.: The point-spread function of a confocal microscope: its measurement and use in deconvolution of 3-D data. In: *Journal of Microscopy* 163 (1991), Nr. 2, S. 151–165

[79] Siemens: *Upgrade your MAGNETOM Trio to the new MAGNETOM Prismafit.* `siemens.com/prisma-fit`

[80] Stejskal, E. O. ; Tanner, J. E.: Spin Diffusion Measurements: Spin Echoes in the Presence of a Time-Dependent Field Gradient. In: *J. Chem. Phys.* 42 (1965), S. 288

[81] Stenger, V. A. ; Noll, Douglas C. ; Boada, Fernando E.: Partial Fourier Reconstruction for Three-Dimensional Gradient Echo Functional MRI: Comparison of Phase Correction Methods. In: *MAGNETIC RESONANCE IN MEDICINE* 40 (1998), Nr. 3, S. 481–490

[82] Szczepankiewicz, Filip ; Lasič, Samo ; van Westen, Danielle ; Sundgren, Pia C. ; Englund, Elisabet ; Westin, Carl-Fredrik ; Ståhlberg, Freddy ; Lätt, Jimmy ; Topgaard, Daniel ; Nilsson, Markus: Quantification of microscopic diffusion anisotropy disentangles effects of orientation dispersion from microstructure: Applications in healthy volunteers and in brain tumors. In: *NeuroImage* 104 (2015), S. 241 – 252

[83] Twieg, DB: The k-trajectory formulation of the NMR imaging process with applications in analysis and synthesis of imaging methods. In: *Medical physics* 10 (1983), Nr. 5, S. 610—621

[84] Weast, R. C. ; Selby, S.M. ; Hodgman, C.D.: *CRC Handbook of Chemistry and Physics*. CRC Press, 1990

[85] Weiss, Audrey J. ; Elixhauser, Anne ; Andrews, Roxanne M.: *Characteristics of Operating Room Procedures in U.S. Hospitals, 2011: Statistical Brief 170*. Agency for Healthcare Research and Quality (US), Rockville (MD), 2014

[86] Wheeler-Kingshott, Claudia A. M. ; Hickman, Simon J. ; Parker, Geoffrey J. M. ; Ciccarelli, Olga ; Symms, Mark R. ; Miller, David H. ; BArker, Gareth J.: Investigating Cervical Spinal Cord Structure using axial diffusion tensor Imaging. In: *Neuro Image* 16 (2002), S. 93–102

[87] Wheeler-Kingshott, Claudia A. ; Parker, Geoffrey J. ; Symms, Mark R. ; Hickmann, Simon J. ; Tofts, Paul S. ; Miller, David H. ; Barker, Gareth J.: ADC mapping of the human optic nerve: Increased resolution, coverage and reliability with csf-suppressed ZOOM-EPI. In: *magnetic resonance in medicine* 47 (2002), S. 24–31

Appendix / Puplications

Shorter Acquisition Times for Diffusion-Weighted Imaging of the Human Spinal Cord with Simultaneous Acquisition of Multiple Inner Fields-of-View

Caspar Florin[1] and Jürgen Finsterbusch[1]

[1]*Systems Neuroscience, University Medical Center Hamburg-Eppendorf, Hamburg, Germany*

Synopsis

Inner field-of-view EPI is widely used for diffusion-weighted acquisitions of the human spinal cord. However, due to the high in-plane resolution required acquisition times to achieve a reasonable signal-to-noise ratio are usually rather long. In this study, inner-field-of-view EPI based on 2D-selectove RF excitations is accelerated with multiband excitations. Two different approaches are considered that differ with respect to the orientation of the 2DRF trajectory and whether side excitations must be suppressed or can be used to cover the bands excited and acquired simultaneously. Results obtained in the human brains stem and cervical spinal cord in vivo are presented.

Introduction

Inner-field-of-view imaging techniques, e.g. based on 2D-selective RF (2DRF) excitations [1, 2] have been shown to improve the image quality for diffusion-weighted echo-planar imaging of the human spinal cord in vivo (e.g. [3, 4]). Due to the high spatial resolution desired, acquisition times are typically about 10 minutes or longer which may hamper the applicability in practice. In this study, two different approaches to shorten the acquisition time by the simultaneous acquisition of multiple inner fields-of-view (e.g. [5]) are considered and demonstrated in phantom and in vivo experiments.

Methods

The basic EPI sequences and geometric setups used are presented in Fig. 1. Both sequences involve a 2DRF pulse for the initial excitation, however, they differ regarding (i) its orientation relative to the imaging part and (ii) the desired excitation profile. In the first sequence, the 2DRF trajectory is rotated by an angle ϕ compared to the slice and phase-encoding direction ("tilted", upper in Fig. 1a) [3]. This allows to position the side excitations occurring in the blip direction between the multiple slices to be refocused (Fig. 1b) which reduces the field-of-excitation and the minimum 2DRF pulse length required but also means that all fields-of-view to be excited need to be included in the desired excitation profile (Fig. 1b). In the second sequence ("swapped") the blip and line direction of the 2DRF trajectory coincide with the slice and phase directions of the imaging part, respectively (lower in Fig. 1a) [4]. Thus, the side excitations can be positioned to cover the other inner fields-of-view to be acquired, i.e. it is sufficient to define only one rectangle as the desired excitation profile (Fig. 1c).

Experiments were performed on a 3 T whole-body MR system (Magnetom PrismaFit, Siemens, Erlangen, Germany). Phantoms and healthy volunteers were investigated with a 64-channel head-neck coil with volunteers giving their informed consent prior to the examination. 2DRF envelopes were calculated using the low-flip-angle approximation [2] and were designed to excite rectangular profile(s) with a size of 4.0x32 mm^2. The resolution of the underlying trajectory was 2.5x10 mm^2. Echo-planar images were obtained with a resolution of 1.0x1.0x4.0 mm^3 covering a field of view (FOV) of 32 x 128 mm^2 with 16 mm oversampling in the phase encoding direction to account for profile imperfections. Diffusion weighting was applied in six non-collinear directions with a b-value of 500 s mm^{-2} yielding echo times between 60 and 70 ms and TRs between 5100 ms and 2600 ms without and with multiband acceleration (acceleration factor 2), respectively. Some acquisitions were performed with blipped-CAIPI [5] gradient pulses to induce an apparent relative shift of 50% of the field-of-view between the slices excited and acquired simultaneously. Non-accelerated acquisition were performed with the "tilted" approach.

Results and Discussion

Results of phantom measurements are presented in Fig. 2. All multiband accelerated acquisition provide an image quality similar to the conventional acquisition, in particular, no residual aliasing artifacts are observed. Furthermore, applying blipped-CAIPI did not offer advantages compared to the "unblipped" approach, most likely because for such small shifts no gain in the g factors could be achieved. This is why in vivo acquisitions were performed without blipped-CAIPI.

Figure 3 presents non-diffusion-weighted and diffusion-weighted images acquired in the human brain stem and spinal cord in vivo. Most striking is the low performance of the swapped approach with a significantly lower SNR. Presumably, this is a consequence of the low bandwidth of the corresponding 2DRF excitation in the blip direction which coincides with the slice direction for this sequence version. This means that even a minor deviation of the frequency, e.g. due to field inhomogeneities, may result in a significant spatial shift and a corresponding signal loss because of a mismatch with the refocusing RF pulse.

Color-coded FA maps of the slices shown in Fig. 3 are compared in Fig. 4. The multiband accelerated acquisition performs better than the non-accelerated acquisition with the same acquisition time (4.6 min) but seems not to achieve the quality of the full acquisition which however takes more than minutes. Although the number of averages is identical (16), this can be expected because due to the much shorter TR (2.6 s vs 5.1 s), saturation effect are significant for the accelerated acquisition.

Conclusion

With multiband acceleration, the acquisition time of diffusion-weighted inner field-of-view echo-planar imaging of the human spinal could be shortened which could help to improve its applicability in clinical practice.

Acknowledgements

This work was supported by a grant from Wings for Life.

References

[1] Hardy CJ et al.: Spatial localization in 2 dimensions using NMR designer pulses. J Magn Reson. 1989; 82: 647-654

[2] Pauly J et al.: A k-space analysis of small-tip-angle excitation. J Magn Reson, 1989; 81: 43-56

[3] Finsterbusch J, Improving the performance of diffusion-weighted inner field-of-view echo-planar imaging based on 2D-selective radiofrequency excitations by tilting the excitation plane. J Magn Reson. Imaging 2012; 35: 984-92.

[4] Saritas EU, Cunningham CH, Lee JH, Han ET, Nishimura DG. DWI of the spinal cord with reduced FOV single-shot EPI. Magn Reson Med. 2008; 60: 468-73.

[5] Setsompop K et al.: Blipped-controlled aliasing in parallel imaging for simultaneous multislice echo planar imaging with reduced g-factor penalty. Mag Reson Med. 2012; 67: 1210-1224

Figures

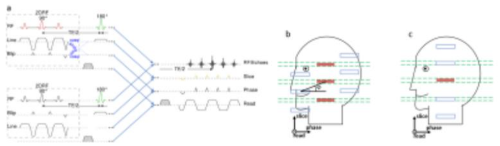

Basic (a) pulse sequences and (b, c) geometric setups for the “tilted” (upper+right a, b) and “swapped” (lower+right a, c) approaches. In the “tilted” version, the 2DRF trajectory is rotated compared to the imaging trajectory, for the “swapped” version the 2DRF line and blip directions coincide with the phase and slice direction, respectively. Filled rectangles illustrate the defined excitation profile, empty ones the side excitations. For the “swapped” version, the side excitations cover the other bands to be excited; for the “tilted” version, they need to be positioned between the refocusing bands to avoid unwanted signal contributions.

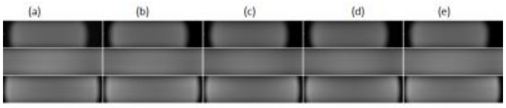

Diffusion-weighted images of three slices in a water phantom obtained (a) without and (b-e) with multiband acceleration using the (b, c) „tilted“ and (d, e) „swapped“ approach (b, d) without and (c, e) with blipped CAIPI.

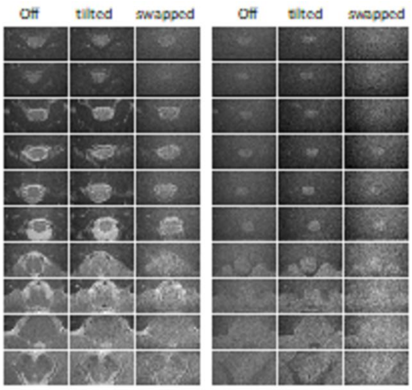

In vivo MR images without (left) and with diffusion weighting (right) without multiband acceleration and with multiband acceleration with the „tilted“ and the „swapped“ approach.

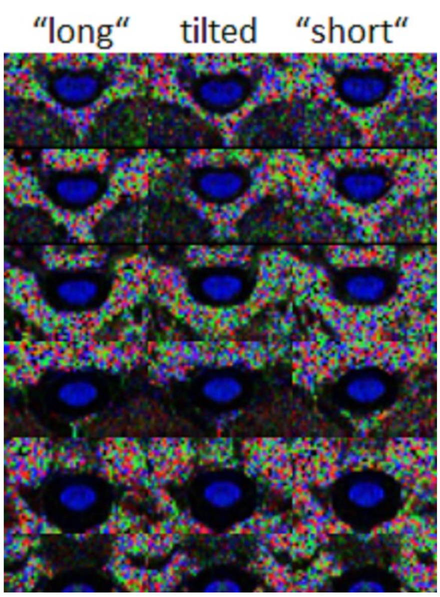

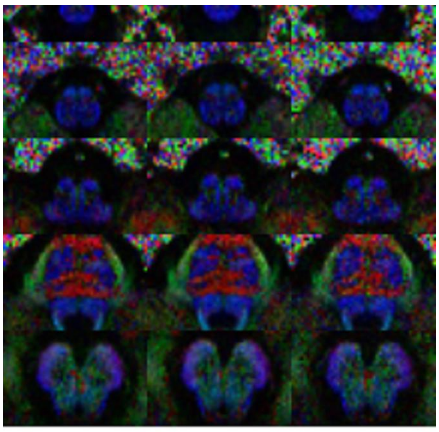

FA maps of the slices shown in Fig. 3 obtained without multiband acceleration and 16 averages („long“, 9.2 minutes acquisition time), with multiband acceleration and the „tilted“ approach (“tilted“, 16 averages, 4.6 minutes), and without multiband acceleration and 8 averages only („short“, 4.6 minutes)

Sensitivity of 2D-Selective RF Excitations for Inner-Field-of-View Diffusion-Weighted Imaging to Field Inhomogeneities

Caspar Florin[1] and Jürgen Finsterbusch[1]

[1]*Department of Systems Neuroscience, University Medical Center Hamburg-Eppendorf, Hamburg, Germany*

Synopsis

Inner-field-of-view techniques based on 2D-selective RF (2DRF) excitations reduce geometric distortions of echo-planar imaging and improve diffusion-weighted imaging of the human spinal cord. A comparison of two common approaches revealed that a setup with the 2DRF excitation collinear to the image plane suffers from a reduced signal-to-noise ratio (SNR) for tall slice stacks. In this study, it is shown that the SNR loss is related to the larger sensitivity of the corresponding 2DRF excitation to frequency offsets caused by field inhomogeneities and is particularly pronounced for the large fields-of-excitation and 2DRF pulse durations needed for tall slice stacks.

Introduction

Geometric distortions of echo-planar imaging (EPI)[1] can be reduced with inner-field-of-view techniques[2-3] based on 2D-selective RF (2DRF) excitations[4-5], which has been shown to improve diffusion-weighted imaging of the human spinal cord[2-3]. A comparison of two inner-field-of-view approaches[2-3] revealed a lower signal-to-noise ratio (SNR) for 2DRF excitations being collinear to the image plane if a large volume is covered[6]. Here, it is shown that this SNR reduction is related to the larger sensitivity of the corresponding 2DRF excitation to frequency offsets caused by field inhomogeneities that are particularly pronounced for the large fields-of-excitation needed for tall slice stacks.

Methods

Figure 1 and 2 present the EPI pulse sequences and geometric setups used in the present study. Both sequences involve a 2DRF excitation based on a fly-back blipped-planar trajectory as the initial excitation but differ regarding its orientation relative to the image plane and the position of the side excitations occurring in the blip direction. In the “collinear” setup (Fig. 1a and 2a), the line and blip direction of the 2DRF trajectory coincide with the imaging phase and slice directions[2], respectively. Thus, to avoid interferences, the side excitations must be positioned above and below the slice stack which requires a large field-of-excitation (FOE) and 2DRF pulse duration for tall slice stacks (cf. Fig. 2a). For the “tilted” setup (Fig. 1b and 2b), the 2DRF trajectory is rotated compared to slice and phase-encoding direction such that the side excitations neither are refocussed nor interfere with the slice stack to measure[3]. Thus, a small FOE is sufficient, independent of the number of slices, yielding short 2DRF pulses. Experiments were performed on a 3T whole-body MR system (PrismaFit, Siemens Healthineers, Erlangen, Germany) using a standard 64-channel head-neck coil in combination with a 32-channel spine array coil. Only coil elements with significant signal contributions were selected for the acquisitions. A water phantom and healthy volunteers that gave their informed consent prior to the examination, were investigated. 2DRF excitations were based on a trajectory resolution of 4.0×10.0mm² in the line×blip (tilted) and blip×line directions (collinear) and were designed to excite rectangular profile(s) with a size of 4×56mm² (slice×phase-encoding direction). 15 to 62 slices were targeted yielding FOEs of 60mm to 248mm for the collinear setup (2DRF pulse duration between (33.8 ms and 7.9 ms) and a fixed FOEs of 70mm for the tilted setup (6.4 ms). An inner FOV of 32×128 mm² with 16 mm oversampling in the phase encoding direction to account for profile imperfection was acquired with a resolution of 1.0×1.0×4.0mm^3. Diffusion-tensor imaging was performed with six non-collinear directions of the diffusion weighting (b value 625 s mm^{-2}) yielding echo times between 64 and 70ms and repetition times between 5600ms. Additionally simultaneous multi-slice (SMS) acquisitions[7] with an acceleration factor of 2 (TR = 3400ms) and a correspondingly reduced FOE were performed for comparison.

Results and Discussion

Figure 3 demonstrates the influence of frequency and gradient offsets on the SNR in a water phantom. For the collinear setup with a small FOE (15 slices) and the tilted setup (15-62 slices), no significant impact on the SNR is observed. However, for the collinear setup with larger FOEs (31 and 62 slices), the frequency (100Hz) and z gradient offset (0.05mT m^{-1}) clearly show a reduced SNR due to the low bandwidth of the 2DRF excitation in the blip, i.e. slice, direction: the offsets shift the excited profile in the slice direction such that it is not fully covered by the refocussing RF pulse. In contrast, the tilted setup exhibits a shift mainly in the phase-direction making it much more robust to frequency offsets and field inhomogeneities. Example images of the human spinal cord are shown in Fig. 4. For larger slice stacks and FOEs, the signal intensity is reduced in some sections of the spinal cord for the collinear setup due to field inhomogeneities. In contrast, the tilted setup shows a no SNR reduction in the cord even for a tall slice stack. In Fig. 5, conventional and SMS DTI acquisitions obtained with the collinear setup are presented. In the SMS acquisitions, the FOE is halved because one of the side excitations is positioned to cover the other slice to be acquired simultaneously which reduces the SNR loss caused by field inhomogeneities.

Conclusion

Compared to the tilted setup, the 2DRF excitation of the collinear setup suffer from an increased sensitivity to field inhomogeneities for tall slice stacks that can reduce the SNR in the spinal cord; however, simultaneous multi-slice acquisitions can help to ameliorate the problem.

Acknowledgements

This work was supported by Wings for Life.

References

1. Mansfield P, Multi-planar image formation using NMR spin echoes. J Phys C 1977; 10: 349-352

2. Saritas EU, Cunningham CH, Lee JH, Han ET, Nishimura DG. DWI of the spinal cord with reduced FOV single-shot EPI. Magn Reson Med. 2008; 60: 468-73.

3. Finsterbusch J. Improving the performance of diffusion-weighted inner field-of-view echo-planar imaging based on 2D-selective radiofrequency excitations by tilting the excitation plane. J Magn Reson. Imaging 2012; 35: 984-92.

4. Hardy CJ, Cline HE Spatial localization in 2 dimensions using NMR designer pulses. J Magn Reson. 1989; 82: 647-654

5. Pauly J, Nishimura DG, Macovski A. A k-space analysis of small-tip-angle excitation. J Magn Reson, 1989; 81: 43-56

6. Florin C, Finsterbusch J. Shorter Acquisition Times for Diffusion-Weighted Imaging of the Human Spinal Cord with Simultaneous Acquisition of Multiple Inner Fields-of-View. Proc Int Soc Magn Reson Med 2018, 1625

7. Setsompop K, Gagoski B, Polimeni J, Witzel T, Wedeen V, Wald LBlipped-controlled aliasing in parallel imaging for simultaneous multislice echo planar imaging with reduced g-factor penalty. Mag Reson Med. 2012; 67: 1210-1224

Figures

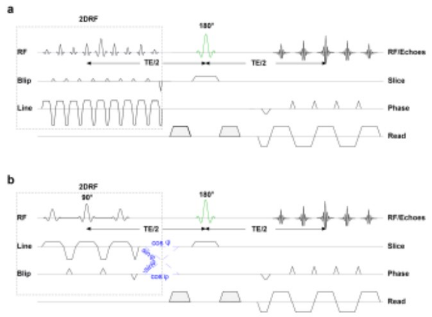

Basic pulse sequences for the (a) collinear and (b) tilted setup with the 2DRF trajectory collinear and tilted compared to the image plane.

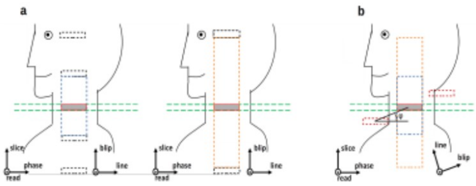

Geometric setups for the (a) collinear approach with a small (left) and tall slice stack (right) and for (c) the tilted approach. The dashed rectangles represent the targeted slice stacks, the filled and empty rectangles the defined excitation profile and the side excitations occur in the blip direction, respectively. For the collinear setup, the distance of the side excitations (field-of-excitation, FOE) and, thus, the 2DRF pulse duration increases with the height of the slice stack but for the tilted setup a fixed, small FOE and short 2DRF pulse duration can be used for both slice stacks.

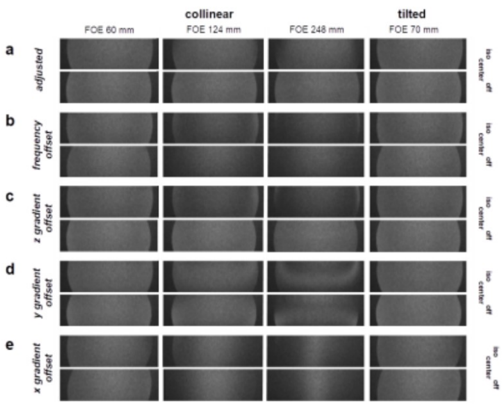

Inner-FOV images of an isocenter (upper) and 36mm-offcenter slice (lower) acquired with the collinear setup with different FOEs as required for different heights of the slice stack (columns 1-3) and the tilted setup (column 4). Acquisitions were performed with (a) the frequency and shim adjusted and (b-e) offsets of the frequency (100Hz) and the gradients (0.05 mT m^{-1}). With the misadjustments, the signal intensity for the collinear setup with a small FOE and for the tilted setup remains unaffected while there are significant signal losses for the collinear setups with the large and medium FOEs.

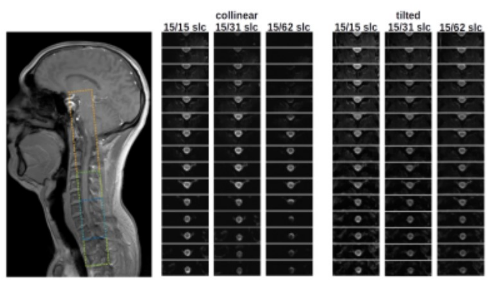

Non-diffusion-weighted images of 15 slices covering the cervical spinal cord acquired with the collinear and tilted setup for different number of slices(15, 31, 62) and heights of the slice stack (60mm, 124mm, 248mm; see localizer). For taller slice stacks, the signal intensity decreases in spinal cord sections suffering from field inhomogeneities for the collinear setup while it remains unaffected for the tilted setup.

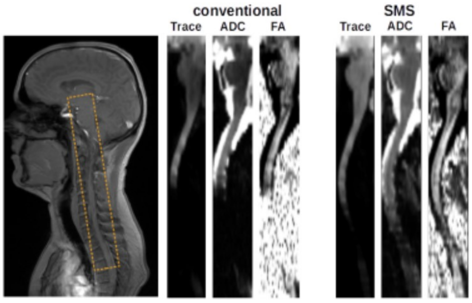

Results of DTI acquisitions (isotropic/trace-weighted image, apparent diffusion coefficient/ADC, fractional anisotropy/FA) with conventional and SMS accelerated acquisitions for the collinear setup. For the SMS acquisitions, the FOE and, thus, the pulse duration is reduced making the 2DRF excitation less sensitive to field inhomogeneities. Thus, SMS accelerated acquisitions benefit not only from a shorter acquisition time but also from an increased robustness.

Diffusion-Weighted ZOOM-EPI with Simultaneous Multi-Slice Imaging

Jürgen Finsterbusch[1] and Caspar Florin[1]

[1]Department of Systems Neuroscience, University Medical Center Hamburg-Eppendorf, Hamburg, Germany

Synopsis

Zonal oblique multi-slice (ZOOM) EPI uses cross-sectional RF excitations to focus the measurement volume to a small, inner volume which allows to reduce the FOV without aliasing in the phase-encoding direction. Thus, geometric distortions are reduced and the spatial resolution of diffusion-weighted acquisitions can be increased as has been demonstrated for the optic nerve and spinal cord. In this study, ZOOM-EPI is combined with simultaneous multi-slice (SMS), the boundary condition to avoid unwanted signal contributions is determined, and the feasibility to shorten acquisitions times is demonstrated for diffusion-tensor imaging (DTI) of the human spinal cord.

Introduction

Spin-echo echo-planar imaging (EPI)[1] is the standard technique for diffusion-weighted acquisitions but suffers from geometric distortions in the presence of field inhomogeneities. The distortions increase with the echo train length and, thus, are more pronounced for larger fields-of-view (FOVs) and higher spatial resolutions which limits the applicability of EPI to small, inner structures like the optic nerve or the spinal cord. To shorten the echo train and reduced geometric distortions accordingly, zonal oblique multi-slice (ZOOM) EPI[2,3] has been proposed. It involves cross-sectional RF excitations to focus the refocussed magnetization to an inner volume which allows to reduce the FOV without aliasing in the phase-encoding direction. In this study, ZOOM-EPI is combined with simultaneous multi-slice (SMS)[4], the boundary condition to avoid unwanted signal contributions is determined, and the feasibility to shorten acquisitions times is demonstrated for diffusion-tensor imaging (DTI) of the human spinal cord.

Methods

The pulse sequences and geometric setups used in the present study are sketched in Fig. 1 and 2. The plane of the initial RF excitation is tilted by an angle φ compared to the image plane defined by the refocussing RF pulse. On both sides of the desired inner FOV, transition zones are excited and refocused which requires phase-encoding oversampling to avoid aliasing. Furthermore, neighboured sections are partially covered and saturated by the tilted RF excitation. Thus, the angle φ must be chosen as a compromise between minimum saturation effects and small transition zones. To extend the conventional approach (Fig. 1a and 2a) to simultaneous multi-slice imaging, both RF pulses must cover multiple frequency bands (Fig. 1b and 2b). As an unwanted side effect, magnetization outside of the target region can be excited and refocused by the bands of different slices. However, they can be positioned outside of the object to avoid their unwanted signal contributions if the tilt angle φ obeys $\tan \varphi < g/(f+max(x1, x2))$ (g: minimum gap between the simultaneously acquired slices, f: desired inner FOV; x_i: distances from inner FOV to object boundary on different sides in the different slices; cf. Fig. 2b). Furthermore, additional gradient pulses to use the blipped-CAIPI approach[4] were applied in the slice direction. Experiments were performed on a 3T whole-body MR system (PrismaFit, Siemens Healthineers, Erlangen, Germany) using a 64-channel head-neck coil together with a 32-channel spine array coil with only those coil elements selected that provide significant signal contributions for the chosen measurement volume. A water phantom was used for test experiments, in vivo acquisitions (62 slices, no gap) were performed in healthy volunteers after their informed consent was obtained. Images were acquired with a voxel size of $1.0\times1.0\times4.0\,mm^3$, a tilt angle φ of 5°, an inner FOV of 40mm plus 20mm phase-encoding oversampling to account for the transition zones, and involved an interleaved excitation order due to saturation in directly neighboured sections. Diffusion-tensor imaging was performed with six different directions of the diffusion weighting, a b value of $625 s\,mm^{-2}$ yielding an echo time of 75ms, and 12 averages. SMS acquisitions were accelerated by a factor of 2 which allowed to shorten the repetition time from 7300ms to 3700ms and the total acquisition time from 10.5min to 5.7min, slightly less than a factor of 2 due to the extra reference acquisitions required for SMS imaging. Isotropic diffusion-weighted images and maps of the apparent diffusion coefficient (ADC) and fractional anisotropy (FA) were obtained with the analysis framework provided by the manufacturer.

Results and Discussion

Non-diffusion-weighted images of the human brain stem and spinal cord are presented in Fig. 3. For lower cord sections, the signal intensity is considerably reduced due to the lower performance of the receive coils. No adverse effect like residual aliasing or noise amplification is observed for the SMS acceleration.

Results of a DTI experiment are summarized in Fig. 4. The conventional and SMS acquisitions show a very similar performance despite the much shorter repetition and acquisition time of the SMS acquisition. Due to the small FOV, only minor geometric distortions are visible in the spinal cord. Color-coded maps of the FA show a reduced anisotropy in spinal cord grey matter, reflect the nerve fibre orientation in white matter, and show some of the fibre crossing of transverse pontine fibres with the pyramidal tracts.

Conclusion

For an appropriately chosen tilt angle, ZOOM-EPI can be accelerated with SMS acquisitions without side effects. Thus, DTI acquisitions of small target regions like the optic nerve or spinal cord can be shortened which could improve the clinical applicability in patients.

Acknowledgements

This work was supported by a grant from Wings for Life.

References

1. Mansfield P. Multi-planar image formation using NMR spin echos. J Phys C. 1977; 10: 55-58.

2. Wheeler-Kingshott CA, Parker GJ, Symms MR, Hickman SJ, Tofts PS, Miller DH, Barker GJ. ADC mapping of the human optic nerve: increased resolution, coverage, and reliability with CSF-suppressed ZOOM-EPI. Magn Reson Med 2002; 47: 24-31.

3. Wheeler-Kingshott CA, Hickman SJ, Parker GJ, Ciccarelli O, Symms MR, Miller DH, Barker GJ. Investigating cervical spinal cord structure using axial diffusion tensor imaging. Neuroimage 2002; 16: 93-102.

4. Setsompop K, Gagoski BA, Polimeni JR, Witzel T, Wedeen VJ, Wald LL. Blipped-controlled aliasing in parallel imaging for simultaneous multislice echo planar imaging with reduced g-factor penalty. Mag Reson Med 2012; 67: 1210-1224

Figures

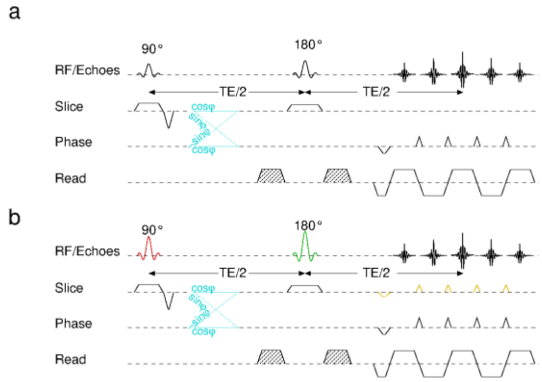

Fig. 1: Basic diffusion-weighted ZOOM-EPI pulse sequences for (a) conventional and (b) SMS acquisitions (acceleration factor 2) as used in the present study. The plane of the initial RF excitation is tilted by an angle φ with respect to the plane of the refocussing RF pulse and the image plane. Colour RF envelopes indicate RF pulses with multiple frequency bands. Note, that the required width and centre frequency of the bands will differ between the excitation and refocussing RF pulses.

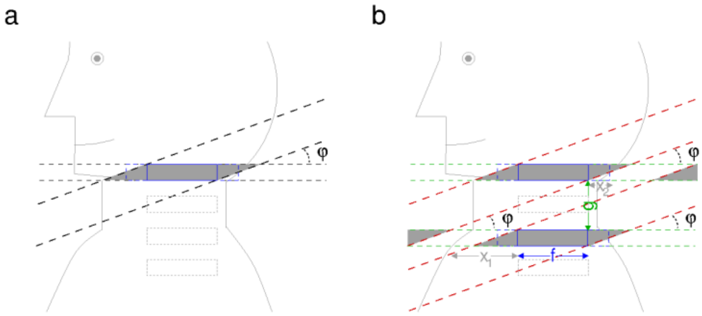

Fig. 2: Geometric setups of ZOOM-EPI for (a) conventional and (b) SMS acquisitions (acceleration factor 2) used in the present study. Grey areas reflect the intersection volumes of the RF excitations (dashed black), i.e. the regions contributing to the acquired signal: the desired inner FOV (solid blue) and transition zones on both sides that require phase-encoding oversampling to avoid aliasing (dashed blue). For SMS acquisitions, additional intersection volumes appear that are excited by the band of one slice but refocused by that of the other; with an appropriately chosen tilt angle φ, they can be positioned outside of the object.

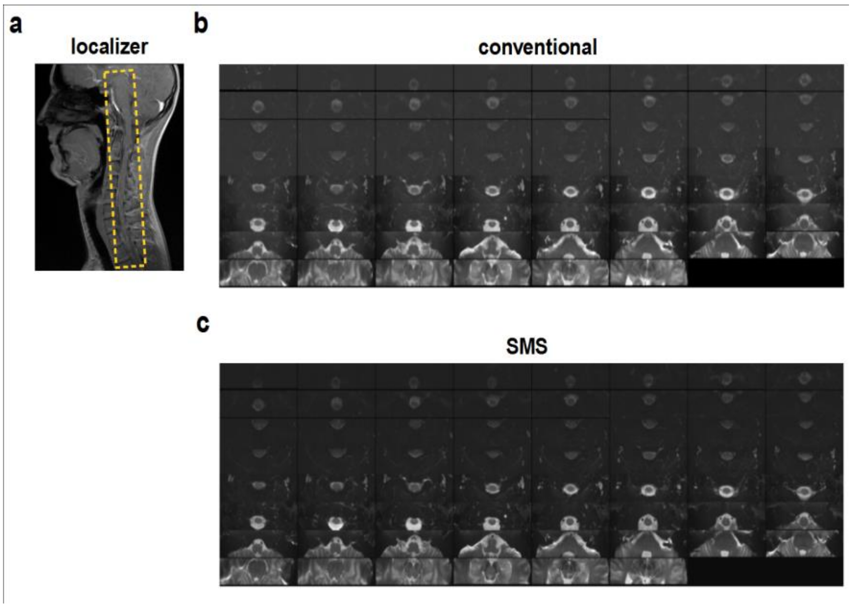

Fig. 3: (a) Localizer and (b, c) averaged non-diffusion-weighted images (voxel size $1.0{\times}1.0{\times}4.0mm^3$) for 15 of the 62 slices covering the brain stem and cervical spinal cord acquired with (b) conventional and (c) SMS acquisitions (acceleration factor 2). For comparability, the same TR (7300ms) was used for both acquisitions.

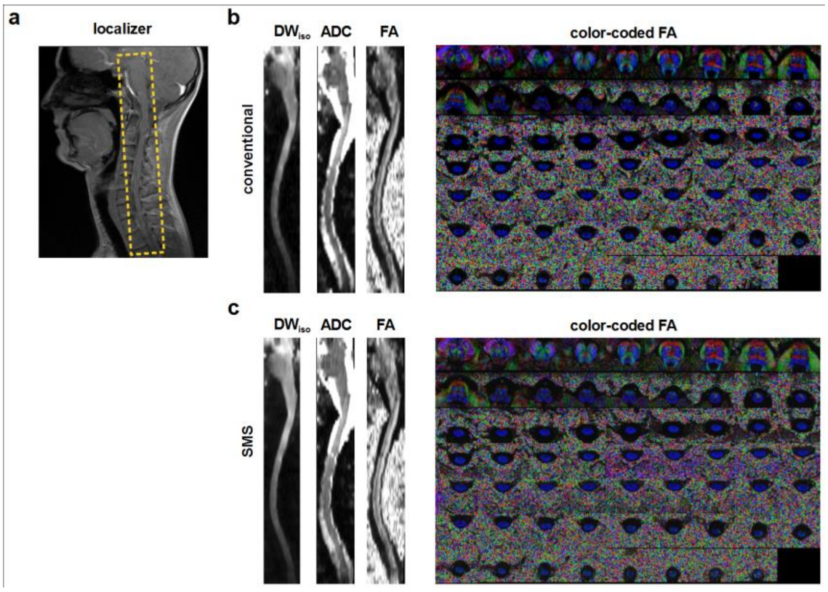

Fig. 4: (a) Localizer image and (b,c) sagittal reconstructions of isotropic diffusion-weighted images and ADC and FA maps and transverse section of the color-coded FA (voxel size $1.0 \times 1.0 \times 4.0 mm^3$) obtained with (b) conventional (10.5min) and (c) SMS acquisitions (acceleration factor 2, 5.7min).

Robust Diffusion-Weighted Imaging Close to Metallic Objects with Inner-FOV STEAM Based on 2D-selective RF Excitations

Caspar Florin[1*] und Jürgen Finsterbusch[1]

[1]Department of Systems Neuroscience, University Medical Center Hamburg–Eppendorf,
[*]cflorin@uke.de

Abstract:
2DRF inner field-of-view diffusion weighted EPI has shown good image quality in the spinal cord. Still in the vicinity of metallic implants EPI suffers strongly. Thus we searched for other diffusion weighted techniques, which do not suffer that strongly in the vicinity of implants. One technique, diffusion weighted TSTEAM is discussed in this study. Further 2DRF inner field-of-view excitations and partial Fourier acquisition were applied to enhance the image qualitiy and acquisition efficiency. EPI and TSTEAM acquisitions were compared.

Zusammenfassung:
Diffusions gewichtete EPI mit kleinen Messfeldern, basierend auf 2DRF Anregungen, zeigt gute Bildqualität im Rückenmark. In der Nähe von metallischen Implantaten leidet die EPI Leistung jedoch sehr stak. Aufgrund dessen wurde nach diffusions gewichteten Techniken gesucht, die nicht so stark beeinträchtigt werden. Eine dieser Techniken, diffusions gewichteter TSTEAM, wird in dieser Arbeit untersucht. Um die Bildqualität und die Aufnahmeeffizienz zu steigern, wurden auf 2DRF basierende innere Messfelder und partielle Fourier-Transformation verwendet. Als Vergleich wurden EPI und TSTEAM untersucht.

Motivation

A valuable non-invasive access to white matter fibre structures and tissue structure is provided by diffusion weighted (DW) imaging. This could provide valuable information to characterize and monitor spinal cord injuries. Previous studies with inner field-of-view (FOV) echo-planar imaging (EPI) have shown to improve the image quality in the spinal cord (1). But as fatal artifacts can occur due to strong field inhomogeinities and in the vicinity of metallic implants turbo stimulated echo acquisiton mode (TSTEAM) (3) was proped in this work to test the robustness of it.
Additionally partial Fourier (PF) acquisition (2) was used and further inner FOV acquisitions, based on 2D-selective RF (2DRF) excitations (4), were implemented to reduce the amount of k-space lines measured and the duration of the TSTEAM measurement. This study examines the image qualtiy near metallic subjects in test objects and compares the results of TSTEAM and EPI.

Materials and Methods

In Figure 1 the basic DW TSTEAM sequence used in this study is presented. The sequence is based on an initial 2DRF excitation. The 2DRF trajectory is rotated by an angle ϕ to slice and phase-encoding direction. Due to this rotation the side excitations, arising with 2DRF excitations, are shifted out of the slice stack to be measured. Further the field-of-excitation (FOE) and the 2DRF pulse length are reduced.
MR images were acquired on a 3T whole-body MR system (Siemens PrismaFit) using a 64 channel head-neck and a spatial resolution of

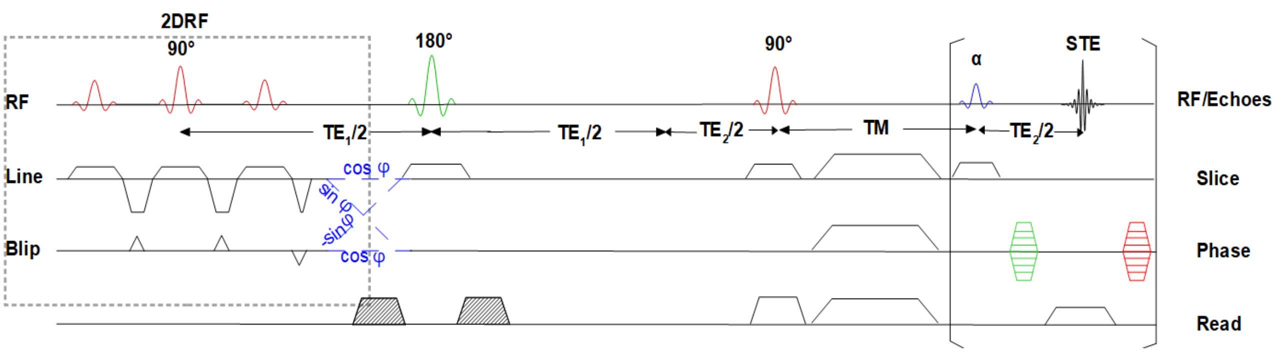

Fig. 1: Basic pulse sequence of DW inner FOV TSTEAM, based on 2DRF excitations where the 2DRF trajectory is rotated by ϕ compared to the imaging trajectory

1.0x1.0x4.0 mm³ covering a FOV of 100x128 mm² and 32x128 mm². Diffusion tensor imaging (DTI) involved 20 slices with 8 averages of 6 directions of the diffusion weighting at a *b* value of 500 s mm^{-2} together with an image without diffusion weighting yielding TRs between 4000 and 8000 ms resulting in total acquisition times between 6.3 and 14 min. The images were acquiered in a water phantom and in a cucumber filled with 2 parallel 20 cent coins and one perpendicular in a distance of 1.1 cm to simulate artifacts from metals.

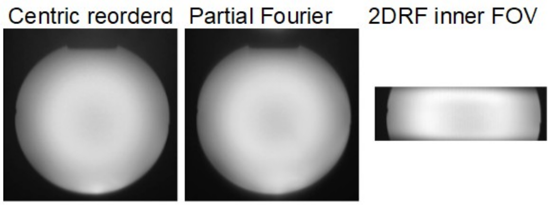

Fig. 2: Images of Water phantom measured with TSTEAM with varying methods. Centric reorderd, PF with a Factor of ½, PF combined with 2DRF inner FOV (from left to right).

Results and Discussion

In Figure 2 TSTEAM images of a water phatom acquiered using centric reordered and PF method to measure the k-space lines, and 2DRF inner FOV acquisitions. The image quality slightly increases (l.t.r.) and the time needed in comparision is decreasing, from 1.6 s to 1 s to 0.5 s per slice (l.t.r.). This is due to the fact that in case of inner FOV less k-space lines are measured thus on one hand the acquisition is faster and on the other the signal desaturation is smaller, resulting in a higher flip angle of 22° compared to 12° can be used.

In Figure 3 non DW images acquired with TSTEAM and EPI in a cucumber filled with coins is presented. It can be observed that far away from the coins (non marked areas) the image quality and the time efficiency of the EPI measurement (c) is superior to the TSTEAM measurements (b).

But in the vicinity of the coins it can be observed that EPI suffers strongly, the coin or the cucumber are nearly unrecognisable (blue marked areas). The TSTEAM aqcuistion on the other hand shows nice images in which nearly no artifacts are observable and it is nearly possible to recognise the coins used. The reason behind is that TSTEAM is less sensitive to field inhomogeneities and metallic subjects. This is due to the fact that the echos are RF refocused individually.

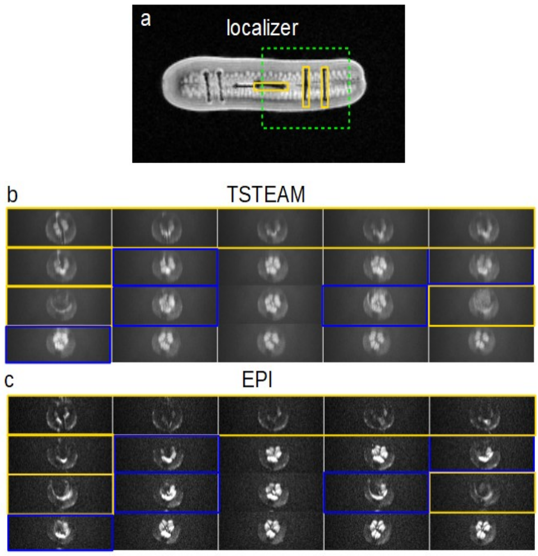

Fig. 3: (a) localizer of a cucumber with coins in it, which are highlighted by yellow rectangles, the measured stack is represented by blue dashed rectangle. Further are in (b) full FOV TSTEAM, (c) inner FOV TSTEAM and (d) inner FOV EPI measurements, with the coins highlighted by gold rectangles and slices in the vicinity of the coins in blue, presented.

Conclusion

The Addition of PF and inner FOV to TSTEAM accelerates the image acquisition and increases the image quality.

Images acquiered with EPI with no metals in the vicinity are acquiered much faster and show a better image quality compared to inner FOV TSTEAM. But near metals inner FOV TSTEAM shines. TSTEAM is much more robust than EPI and shows no artifacts. To enhance the efficiency of inner FOV TSTEAM one solution could be simultaneous mulit-slice imaging.

Acknowledgements

This work was supported by a grant of Wings for Life.

References

1. Saritas EU. DWI of the spinal cord with reduced FOV single-shot EPI. MRM, 2008;60: 468-473

2. Margosian P, Schmitt F, Purdy DE, Faster MR imaging: Imaging with half the date. Health Care Instrum. 1994;32: 535-539

3. Mulcahey MJ, Diffusion Tensor Imaging in Pediatric Spinal Cord Injury. Spine. 2012;37: E797

4. Pauly J, A k-Space Analysis and of Small-Tip-Angle and Excitation. JMR. 1989;81:4

Robust Diffusion-Weighted Imaging near Metallic Objects with Inner-FOV Single-Shot STEAM based on 2D-Selective RF Excitations

Caspar Florin[1] and Jürgen Finsterbusch[1]

[1]Department of Systems Neuroscience, University Medical Center Hamburg-Eppendorf, Hamburg, Germany

Synopsis

The potential of a single-shot stimulated echo acquisition mode (STEAM) sequence based on RF refocused echoes for DW imaging close to metallic objects is evaluated. It is optimized for spinal cord applications by combining it with inner-FOV technique based on 2D-selective RF (2DRF) excitations and half-Fourier sampling which improves its signal-to-noise ratio (SNR) efficiency significantly. Its robustness in the presence of metallic objects is investigated and compared to EPI showing a better performance with smaller regions suffering from signal losses.

Introduction

Diffusion weighted (DW) imaging is a powerful tool to access white matter fibre tracts and tissue microstructure and could be valuable to characterize and/or monitor spinal cord injuries. While inner field-of-view (FOV) echo-planar imaging (EPI) is able to provide a good image quality for DW imaging of the spinal cord[1,2], it suffers from severe artifacts in the presence of metallic objects making it unusable in regions close to implants stabilizing the lower spine. Here, the potential of a single-shot stimulated echo acquisition mode (STEAM) sequence[3] based on RF refocused echoes for DW imaging close to metallic objects is evaluated. It is optimized for spinal cord applications by combining it with inner-FOV technique based on 2D-selective RF (2DRF) excitations[4] and half-Fourier sampling[5] which improves its signal-to-noise ratio (SNR) efficiency significantly. Its robustness in the presence of metallic objects is investigated and compared to EPI showing a better performance with smaller regions suffering from signal losses.

Methods

The basic pulse sequence used in this study is presented in Figure 1. It is based on an initial 2DRF excitation with a blipped-planar trajectory tilted by an angle ϕ compared to the slice and phase-encoding direction in order to shift the unwanted side excitations out of the refocussing plane and the slice stack to be measured which reduces the field-of-excitation (FOE) and the RF pulse length considerably[2]. The 2DRF envelopes were calculated using the low-flip-angle approximation[4] and designed to excite a rectangular profile with a size of 4×56mm² (slice×phase-encoding direction) using a trajectory with a resolution of 4.0×10.0mm² in the line×blip direction.

Single-shot STEAM and EPI Images were acquired on a 3T whole-body MR system (PrismaFit, Siemens) using a 64-channel head-neck coil using a voxel size of 1.0x1.0x4.0 mm³ and covering either a full FOV of 100x128 mm² or an inner FOV of 32x128 mm². The readout flip angle of single-shot STEAM was adapted to yield a point-spread function with a full-width at half-maximum (FWHM) corresponding to the nominal resolution[3]. For diffusion tensor imaging (DTI), 20 slices with 8 averages of 6 diffusion directions with a diffusion weighting of 500 s mm-2 and a non-diffusion weighted image were acquired. TR was between 4000 and 8000 ms resulting in total acquisition times between 6.3 and 11.2 min.

A water phantom and a cucumber larded with 20-cent coins (€) as metallic objects and healthy volunteers were investigated, the latter giving their informed consent prior to examination.

Results and Discussion

Results and Discussion (220) Figure 2 shows the advantages of half-Fourier sampling and inner-FOV acquisition for single-shot STEAM. With both techniques applied, the acquisition time is reduced from 1183 ms to 264 ms while there is almost no SNR penalty yielding an overall increase of the SNR efficiency by about 100%, While both techniques reduce the number of k-space lines and, thus, decrease the SNR at a first glance, the modified sampling allows for larger readout flip angles (e.g. from 12° to 22°) for the same FWHM of the point-spread function which increases the signal amplitude.

Results of in vivo acquisitions are presented in Figure 3. While EPI is much faster (6.2 min vs 11.2 for single-shot STEAM) and provides a better SNR, it suffers from geometric distortions caused by global and local field inhomogeneities even in the absence of metallic objects. In contrast, single-shot STEAM is more robust and, e.g., does not show a modulation of the posterior edge along the spinal cord.

This is demonstrated in Fig. 4 showing the results of experiments in the phantom with metallic objects. EPI not only suffers from pronounced signal loses in slices containing parts of the coins, but also in neighbouring sections. On the other hand, single-shot STEAM is rather robust, even in regions close to the coins, and clearly shows the exact position and shape of the coins.

Conclusion

The SNR efficiency of single-shot STEAM can be significantly improved by using inner-FOV techniques, e.g. based on 2DRF excitations, and half-Fourier sampling. Compared to EPI it still suffers from a reduced SNR but is much less prone to metallic objects and field inhomogeneities. Thus, it could be a viable technique to investigate spinal cord regions close to implants.

Acknowledgements

This work was supported by a grant from Wings for Life.

References

1. Saritas EU, Cunningham CH, Lee HJ, et al., DWI of the spinal cord with reduced FOV single-shot EPI. MRM, 2008;60: 468-473

2. Finsterbusch J,Improving the performance of diffusion-weighted inner field-of-view echo-planar imaging based on 2D-selective radiofrequency excitations by tilting the excitation plane. JMRI, 2012;35: 984-992

3. Nolte UG, Finsterbusch J, Frahm J, Rapid Isotropic and Diffusion Mapping and Without Susceptibility and Artifacts: Whole and Brain Studies and Using Diffusion-Weighted and Single-Shot STEAM and MR Imaging. MRM, 2000;

4. Pauly J, Nishimura D, Macovski A, A k-Space Analysis and of Small-Tip-Angle and Excitation. JMR. 1989;81:4

5. Margosian P, Schmitt F, Purdy DE, Faster MR imaging: Imaging with half the date. Health Care Instrum. 1994;32: 535-539

Figures

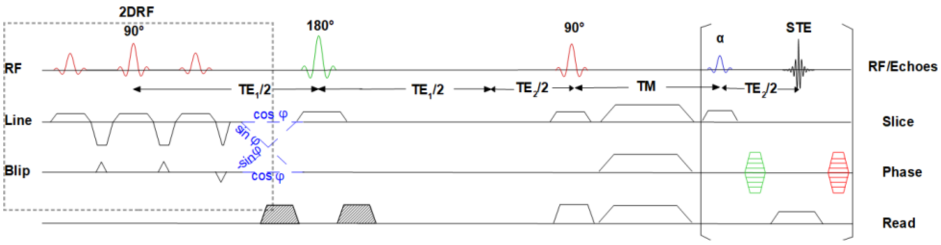

Basic pulse sequence of inner-FOV single-shot STEAM based on 2D-selective RF excitations with a tilted trajectory as used in the present study.

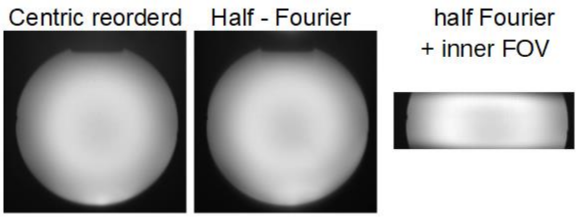

Images of Water phantom measured with single-shot STEAM covering a full field-of-view with centric reordering (1183ms per slice, readout flip angle 12°, relative SNR 100%) and half-Fourier encoding (652ms, 18°, 120%) and an inner field-of-view with half-Fourier encoding (263ms, 22°, 98%) (from left to right).

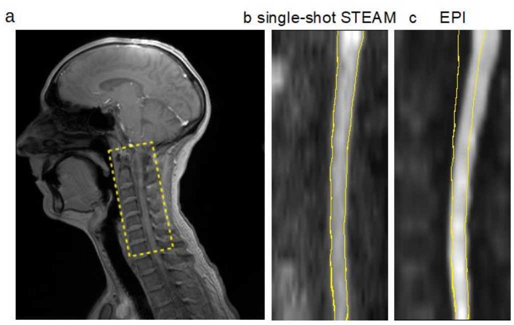

(a) Localizer with the measured slice stack (yellow box). (b,c) Sagittal reconstructions of isotropic diffusion-weighted images (20 slices, 1.0x1.0x5.0mm) acquired with inner-FOV (b) single-shot STEAM and (c) EPI. The reconstructions shown in (b) single-shot STEAM and (c) EPI. The yellow outline of the spinal cord defined on the STEAM images and the arrows clearly show the geometric distortion present in EPI as a consequence of global and local field inhomogeneities.

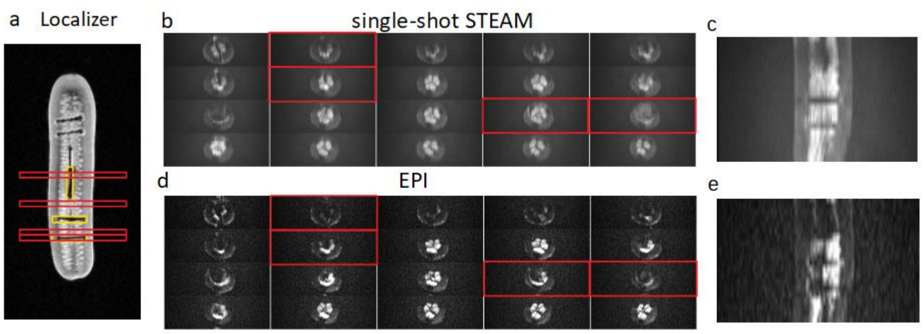

(a) Localizer of a cucumber with coins that are highlighted by the yellow rectangles. (b,d) Non-diffusion-weighted images obtained with (b) single-shot STEAM and (d) EPI and (c,d) coronal reconstructions. While slices close to or containing the coins (e.g., red frames) suffer from pronounces signal losses for EPI, single-shot STEAM is more robust and clearly shows the position and shape of the coins.

Single-Shot Inner-Field-of-View Fast Spin Echo Imaging with MAVRIC: Access to the Spinal Cord Close to Metallic Implants

Caspar Florin[1] and Jürgen Finsterbusch[1]
[1] 1Department of Systems Neuroscience, University Medical Center Hamburg–Eppendorf, Hamburg, Germany

Synopsis

Inner field-of-view EPI provides a good image quality for diffusion-weighted imaging of the spinal cord in healthy subjects but suffers from severe artifacts in the vicinity of metallic implants that may be present in patients with traumatic injuries. Here, inner-field-of-view imaging based on cross-sectional RF pulses is used to obtain a single-shot fast spin echo technique that combined with multi acquisition variable-resonance imaging (MAVRIC) and view angle tilt (VAT) offers a more robust access to small target regions close to metallic implants and, thus, may be feasible for diffusion-weighted imaging of patients with traumatic spinal cord injury.

Introduction

Inner field-of-view EPI, e.g. (1,2), provides a good image quality for diffusion-weighted imaging (DWI) of the spinal cord in healthy subjects. But it suffers from severe artifacts in the vicinity of metallic implants making it unfeasible for most patients with traumatic injuries. Fast-spin-echo (FSE) imaging, in particular when combined with multi acquisition variable-resonance imaging (MAVRIC)(3) and view angle tilt (VAT)(4) is much more robust, however, may not be applicable in a single-shot as desired for DWI. Here, inner-field-of-view imaging based on cross-sectional RF pulses is combined with FSE imaging to enable single-shot imaging that in combination MAVRIC and VAT can provide a much better image quality close to metallic objects than EPI and, thus, may be feasible for diffusion-weighted imaging of patients with traumatic spinal cord injury.

Materials and Methods

The basic pulse sequence (Fig. 1) has been derived from a standard fast-spin-echo sequence. An extra refocusing section is inserted prior to the readout interval that could be used to apply diffusion weighting and is tilted by an angle ϕ compared to the image plane. The latter allows to reduce the FOV in the phase-encoding direction without aliasing and can shorten the echo train accordingly to make it feasible for single-shot acquisitions. To introduce the frequency-selectivity required for MAVRIC, the initial RF excitation is applied without slice-selection gradient pulse but different frequency offsets that differ between subsequent acquisitions of the same slice; the same frequency offsets are also considered for all subsequent slice-selective RF pulses and add to the frequency required for the conventional slice selection. The readout is performed with view angle tilt, i,e. a gradient pulse in the slice direction during the data acquisition. Measurements were performed on a 3T whole-body MR system (Siemens PrismaFit) using a 64 channel head-neck coil and a 32 channel spine coil on phantoms with metallic objects (four aluminum screws; see Fig. 2) and a volunteer with a metallic implant from whom informed consent was obtained prior to the examination. A resolution of 1.0x1.0x4.0mm³ covering a FOV of 32x128 mm² was used yielding an echo spacing of 7.4ms, an echo time of 35ms for an ascending sampling for the FSE. With a frequency width of the RF pulses of about 1000Hz, the MAVRIC frequency range between +10kHz and -10kHz for phantom measurements and 2000 Hz and -2000Hz in vivo was sampled in steps of 500Hz in an interleaved order. All frequencies were stepped through for a slice with a TR of 900ms yielding a total acquisition time per slice of 1.13min for phantom and of 8.1s for in vivo measurements before continuing with the next slice. A maximum intensity projection across frequency offsets was used to calculate a single image for each slice on the fly. The EPI measurement yielded a total measurement duration of 5 s with a TR of 4200 ms and a TE of 65 ms.

Results and Discussion

Figure 2 summarizes results obtained in the phantom with metallic objects (four aluminum screws). Signal losses close to and even at a distance from the screws are obvious in the localizer image (Fig. 2a) and within the FSE acquisitions without MAVRIC (Fig. 2b). With MAVRIC, significant signal can be regained and almost the full phantom becomes visible, although with some residual interferences and remaining signal losses. These images underline the significant influence of even smaller metallic objects and the capability of the MAVRIC approach to recover signal. In figure 3 measurements of a volunteer with metallic implants are presented. Thereby the cancellations due to the implants are apparent in the localizer (a). Further in Fig 3 transversal in vivo measurements with inner FOV EPI (b) and inner FOV FSE (c) are shown. In case of the EPI images the spinal cord is nearly not identifiable, the distortions due to the metallic screws and plates are too strong. With the combination of FSE and MAVRIC the spinal cord can be observed and in nearly all slices parts of it are recognizable, even though the SNR is rather low. The image quality difference in between FSE and EPI is due to the different refocusing techniques used, RF refocused and gradient refocused, respectively, as the least reacts more prone to inhomogeneities. The reason for the varying measured frequency ranges during the phantom and in vivo acquisitions are due to the different susceptibilities of the implant materials. The susceptibility of aluminum, as used for the phantom, is by a factor of 10^2 larger compared to titanium as present in the volunteer and thus leads to stronger distortions.

Conclusion

The combination of FSE with ZOOM and MAVRIC proves to be a tool with which the image acquisition near metallic artifacts can be improved significantly. Still work has to be done to accelerate the acquisition time. A possibility to accelerate the image acquisition could lie in combination of MAVRIC with simultaneous multi-slice imaging.

Acknowledgements

This work was supported by a grant of Wings for Life

References

[1] Saritas EU. DWI of the spinal cord with reduced FOV single-shot EPI. MRM, 2008;60: 468-473

[2] Wheeler-Kingshott CA. ADC mapping of the human optic nerve: Increased resolution, coverage and reliability with csf-suppressed ZOOM-EPI, MRM, 2002 (47) 24-31

[3] Koch KM et al., Imaging near metal with a MAVRIC-SEMAC hybrid. Magn Reson Med, 2011 (65) 71-82

[4] Cho ZH et al Total inhomogeneity correction including chemical shifts and susceptibility by view angle tilting, A. A. Phys. In Medicine 1988, (15), 7-11

Figures

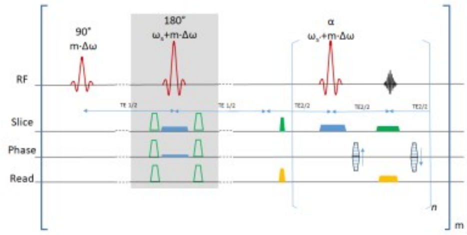

Pulse sequence of DW inner FOV TSTEAM, based on ZOOM excitations where the 2nd 180° pulse Trajectory (grey underlined) is rotated by ϕ compared to the imaging trajectory and a slice selective frequency ωs modulated by a frequency offset m·Δω. Additional VAT gradients (green) and the possibility of frequency selective excitation (1st excitation)for MAVRIC with an increment m per MAVRIC repetition.

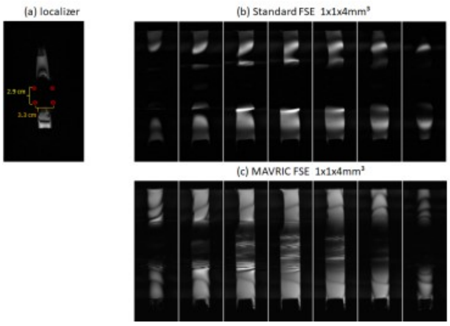

(a) Localizer of water phantom with a diameter of 2.8 cm, surrounded by 4 aluminum screws, with 2.9 cm and 3.3 cm to each other. (b) 7 out of 20 inner FOV FSE MAVRIC acquisitions with a resolution of 1x1x4mm³ (c) 7 out of 20 inner FOV FSE MAVRIC acquisitions with a resolution of 1x1x4mm³ and 81 MAVRIC frequency steps of Δω 500 Hz

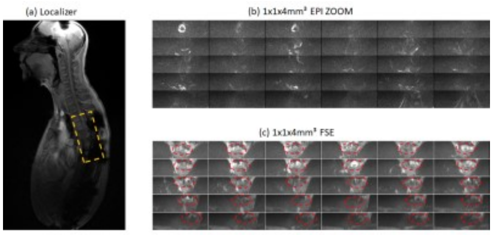

(a) Localizer of a volunteer with metallic implants and measured slice stack highlighted in orange. (b) 30 1x1x4mm³ transversal ZOOM EPI acquisitions (c) 30 1x1x4mm³ transversal ZOOM MAVRIC FSE acquisitions with a frequency increment of 500 Hz and 9 steps. The spinal cord is highlighted by red dotted ellipsoids.

Acknowledgments

At this point I would like to thank everyone who guided and helped me realize this thesis. In particular I want to thank:

- Dr. Jürgen Finsterbusch, who made it possible to write my thesis in his group. I'm very thankful for his help in any situation, his supervision, his tenacious teachings, the fruitful discussions and the ideas contributing to this work.
- Prof. Dr. Florian Grüner, who agreed to carry out the survey of this thesis.
- Prof. Dr. Martin Koch and Dr. Thomas Lindner, who both agreed to be part of the examination comity of the thesis defense.
- Prof. Dr. Hagner for who agreed to be the chair of the examination comity
- Patrick Freund and his group for giving us the possibility and helping us perform measurements at balgrist.
- Our medical technical assistants who helped with measurement and were always helpful in case of problems.
- Carolina Dlugosch and Heike Path who are always ready to help.
- Francisco Lagos Fritz for helping me with post processing of the data.
- Tobias Streubel for being a great roommate during conferences and always helpful during measurements with ideas or as volunteer.
- Ying Chu for all the discussions regarding programming and measurements.
- Henning Runge and Marcel Diem for proof reading and all the discussions we had.
- My family and friends always supporting and motivating me. In particular my wife Denise Florin.

Eidesstattliche Versicherung / Declaration on oath

Hiermit versichere ich, Caspar Florin, an Eides statt, die vorliegende Dissertationsschrift selbst verfasst und keine anderen als die angegebenen Hilfsmittel und Quellen benutzt zu haben.

Die eingereichte schriftliche Fassung entspricht der auf dem elektronischen Speichermedium.

Die Dissertation wurde in der vorgelegten oder einer ähnlichen Form nicht schon einmal in einem früheren Promotionsverfahren angenommen oder als ungenügend beurteilt.

Hamburg, September 16, 2002

Caspar Florin